DEVELOPMENT OF METHODS FOR DRUG RELEASE EVALUATION FROM ADVANCED NANOPOROUS ANODIC ALUMINA STRUCTURES

Pankaj Kapruwan

UNIVERSITAT ROVIRA i VIRGILI

Development of Methods for Drug Release Evaluation from Advanced Nanoporous Anodic Alumina Structures

Pankaj Kapruwan

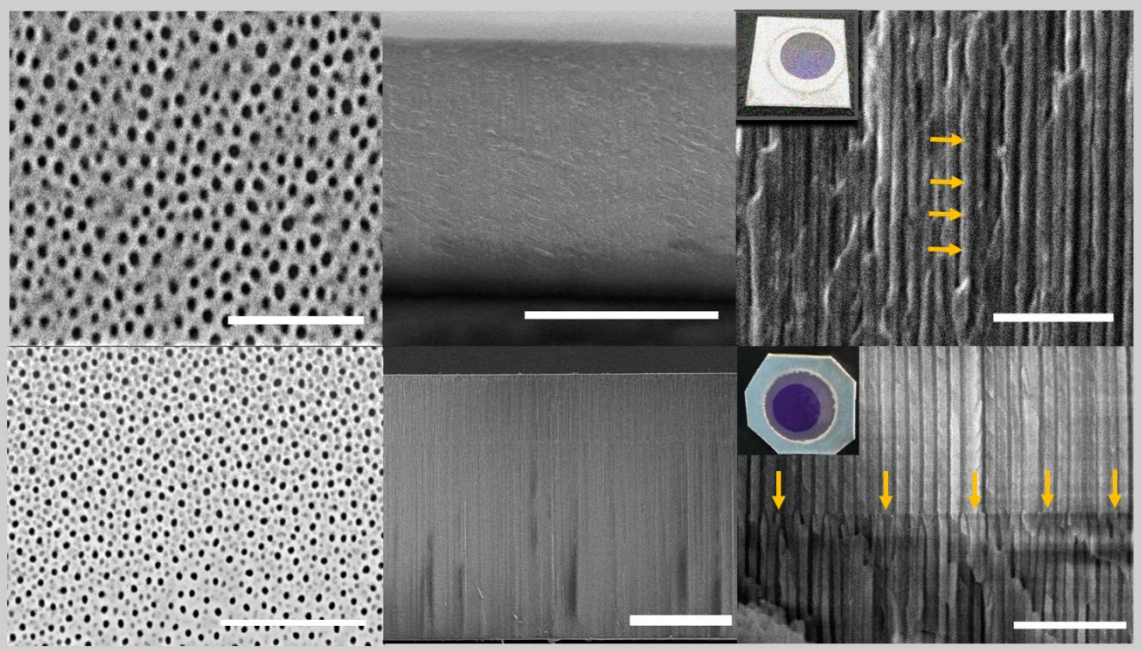

DOCTORAL THESIS

2021

UNIVERSITAT ROVIRA I VIRGILI
DEVELOPMENT OF METHODS FOR DRUG RELEASE EVALUATION FROM ADVANCED NANOPOROUS ANODIC ALUMINA STRUCTURES
Pankaj Kapruwan

UNIVERSITAT ROVIRA I VIRGILI
DEVELOPMENT OF METHODS FOR DRUG RELEASE EVALUATION FROM ADVANCED NANOPOROUS ANODIC ALUMINA STRUCTURES
Pankaj Kapruwan

Pankaj Kapruwan

Development of Methods for Drug Release Evaluation from Advanced Nanoporous Anodic Alumina Structures

Ph.D. Thesis

Supervised by

Dr. Josep Ferré-Borrull and Prof. Lluís Francesc Marsal Garví

Department of Electrical, Electronic and Automatic Engineering

Nano-Electronic and Photonic Systems (NePhoS)

UNIVERSITAT ROVIRA i VIRGILI

Tarragona

2021

UNIVERSITAT ROVIRA I VIRGILI
DEVELOPMENT OF METHODS FOR DRUG RELEASE EVALUATION FROM ADVANCED NANOPOROUS ANODIC ALUMINA STRUCTURES
Pankaj Kapruwan

Escola Tècnica Superior D'Enginyeria
Departament d'Enginyeria Electrònica, Elèctrica i Automàtica Campus Sescelades
Avinguda dels Països
Catalans, 26 43007
Tarragona, Espanya
Tel.: + 34 977 559 610
Fax: + 34 977 559 605

FAIG CONSTAR que aquest treball, titulat "**Development of Methods for Drug Release Evaluation from Advanced Nanoporous Anodic Alumina Structures**", que presenta **Pankaj Kapruwan** per a l'obtenció del títol de Doctor, ha estat realitzat sota la meva direcció al Departament d'Enginyeria Electrònica, Eléctrica i Automàtica d'aquesta universitat.

HAGO CONSTAR que el presente trabajo, titulado "**Development of Methods for Drug Release Evaluation from Advanced Nanoporous Anodic Alumina Structures**", que presenta **Pankaj Kapruwan** para la obtención del título de Doctor, ha sido realizado bajo mi dirección en el Departamento de Ingeniería Eléctrica, Electrónica y Automática de esta Universidad.

I STATE that the present study, entitled "**Development of Methods for Drug Release Evaluation from Advanced Nanoporous Anodic Alumina Structures**", presented by **Pankaj Kapruwan** for the award of the degree of Doctor, has been carried out under my supervision at the Department of Electronic, Electric and Automatic Engineering of this university.

Tarragona, 01 October 2021

El/s director/s de la tesi doctoral
El/los director/es de la tesis doctoral
Doctoral Thesis Supervisor/s

FERRE BORRULL JOSE - 40935236C
Firmado digitalmente por FERRE BORRULL JOSE - 40935236C
Fecha: 2021.09.30 10:55:17 +02'00'

Dr. Josep Ferré-Borrull

MARSAL GARVI LUIS FRANCISCO - 39688257D
Firmado digitalmente por MARSAL GARVI LUIS FRANCISCO - 39688257D
Fecha: 2021.09.30 11:04:54 +02'00'

Prof Lluís Francesc Marsal Garví

UNIVERSITAT ROVIRA I VIRGILI
DEVELOPMENT OF METHODS FOR DRUG RELEASE EVALUATION FROM ADVANCED NANOPOROUS ANODIC ALUMINA STRUCTURES
Pankaj Kapruwan

Acknowledgements

This PhD thesis is not only a result of my immense interest for science but also of the financial freedom provided to me by the Universitat Rovira i Virgili. This thesis would not have been possible without the help of several people that have supported me during the last 3 years.

First of all, I would like to thank my supervisor Dr. Josep Ferré-Borrull for his continuous encouragement, moral support, and suggestions to keep the research on track and to give me freedom to explore the thrilling world of nanotechnology. The number of articles obtained through this PhD would not have possible without his invaluable comments. I would also like to thank Prof Lluís Marsal, for his constant guidance and for offering me an opportunity to learn and complete my thesis.

I would also like to thank Mariana, Mercè, Debora, and Rita from Servei de Recursos Científics i Tècnics Servei (SRCiT) for their constant support and availability for helping me in obtaining the excellent images.

I am grateful for all the support I got from the current and previous NePhoS group members for making lab 235, 332, and 335 a wonderful environment to work in. Thanks to Pilar, Elisabet, José, Francisco, Laura, Pili, Karen, Sara, Jakub, Rebecca, Amou, Anand, Alfonsina, Enas, Deepanshu, Ahmad, Alejandro, Magali, Angels, Miriam, Menyar, and Marina. Thank you for the wonderful time and excellent teamwork.

Also, I would like to thank the Indian community (Raju, Anvesh, Asmaul, Laxmi & Vida, Sachin, Indrajeet, Basudev, David, Deepika, Naga, Parijaat, Kongkana, Vinayak, Aanchal, Jitesh, Sukruth, Sarika, Madhavi) for their continuous support and activities during my stay in Tarragona. I would also

like to thanks especially to Dr. Anchal Yadav and Ankur for supporting me through the roller-coaster ride of emotions during the three years.

I would like to reserve the biggest acknowledgment to the family (Grandmother, father, mom and brother) for being there all the time when I was low.

Finally, this thesis is dedicated to my father who worked extremely hard during his entire life to be able to support me in all the hard times and not amongst us today. Thank you for everything. I hope you finds peace in heaven.

List of Abbreviations

Al - Aluminium

Al_2O_3 - Aluminium Oxide

μ - Current efficiency

J - Current density

Cu - Copper

$CuCl_2$ - Copper chloride

d_{int} - Interpore distance

d_p - Pore diameter

DOX - Doxorubicin Hydrochloride

DDS - Drug Delivery System

EtOH - Ethanol

FTIR- Fourier transform infrared spectroscopy

Fe - Iron

HA - Hard anodization

H_3PO_4 - Phosphoric acid

H_2O - Deionized water

HCl - Hydrochloric acid

$HClO_4$ - Perchloric acid

$H_2C_2O_4$ - Oxalic acid

Hy-NAA-GIF - Hybrid nanoporous anodic alumina gradient index filter

J - Current density

J_1 - Current density amplitude

j_t - Current density at time (t)

J_o - Offset current density

J_a - Anion current density

J_c - Cation current density

k - Extinction coefficient

SEM - Scanning Electron Microscope

LDDS - Localized drug delivery systems

LBL - Layer by layer deposition

MA- Mild anodization

Mg - Magnesium

Nm - Nanometer

N - Number of cycles

NAA - Nanoporous anodic alumina

NAA-GIF- Nanoporous anodic alumina gradient-index filters

O_2 - Oxygen

P - Porosity

Pt.- Platinum

PLS - Photoluminescence spectroscopy

PEMs - Polyelectrolyte multilayers

PAH - Polyallylamine hydrochloride

PSS - Polystyrene sulfonate

PCs - Photonic crystals

PBG - Photonic band gap

PSB - Photonic stopband

pSi - Porous silicon

PW - Pore widening

PBS - Phosphate buffer saline

Q - Charge

R_p - Pore growth rate

R.I. - Refractive Index

Rh6G - Rhodamine 6G

Si - Silicon

TDDS - Targeted drug delivery systems

TMM - Transfer matrix method

$t_{release}$ - Characteristic time release

T_w - Pore wall thickness

T - Temperature

t - time

T - Sinusoidal time period

τ - Thickness

UV-VIS - Ultraviolet-visible spectrophotometer

V - Voltage

3-aminopropyltriethoxysailane - APTES

% R - Reflectance

µL - Microlitre

List of Figures

List of Tables

List of Contributions

Journal Publications

1. Mahmoud Amouzadeh Tabrizi, Josep Ferré-Borrull, **Pankaj Kapruwan**, Lluis F. Marsal; A photoelectrochemical sandwich immunoassay for protein S100β, a biomarker for Alzheimer's disease, using an ITO electrode modified with a reduced graphene oxide-gold conjugate and CdS-labeled secondary antibody, Microchim Acta 186, 117 (2019).
2. **Pankaj Kapruwan**, Josep Ferré-Borrull, Lluis F. Marsal; Nanoporous Anodic Alumina Platforms for Drug Delivery Applications: Recent Advances and Perspective, Adv. Mater. Interfaces 2020, 7, 2001133.
3. **Pankaj Kapruwan**, Laura K. Acosta, Josep Ferré-Borrull and Lluis F. Marsal; Optical Platform to Analyze a Model Drug-Loading and Releasing Profile Based on Nanoporous Anodic Alumina Gradient Index Filters, Nanomaterials 2021, 11, 730.
4. **Pankaj Kapruwan**, Josep Ferré-Borrull, Lluis F. Marsal; Real-time monitoring of doxorubicin release from hybrid nanoporous anodic alumina structures, Sensors (To be submitted)

Conferences

1. **Pankaj Kapruwan**, Josep ferré-Borrull and Lluis f. Marsal; Analyzing the loading and release of Rhodamine 6G dye from Nanoporous anodic alumina rugates filters using optical methods, Imaginenano (IM2020) Online, Oral contribution.
2. **Pankaj Kapruwan**, Josep ferré-Borrull and Lluis f. Marsal; Optical analysis on infiltration of Rhodamine dye inside Nanoporous anodic alumina Gradient-index filters", NanoBioMed (NBMO2020), ePoster and ePoster-Flash contribution.

Dedicated to my father

((तू साथ हो ना हो, हम राह तकते रहेंगे
तेरे संग ना सही, हम जी के देखेंगे))

Table of Contents

Chapter 1

Introduction

1.1 Motivation and Background

It all started with the famous talk stating ´´**There is plenty of room at the bottom**´´ given by physicist Richard Feynman and since afterwards the nanoscience and nanotechnology research has been grown in an astonishing way that has revolutionized the scientific community. Recent years have seen some tremendous growth for manipulating the materials at the nanoscale level due to their excellent physicochemical properties which usually are not found in their bulk form. As a result, scientists all over the world are speculating new ways to make effective use of the nanoscale properties present in these materials such as the high surface area to volume ratio, excellent mechanical strength, improved chemical reactivity, etc. for the benefit of society.

One of the most interesting and challenging fields in science is to control the propagation and emission of light. Apart from the day-to-day activities in our daily life, light also plays a crucial role in several applications that include telecommunications, sensors, data storage, imaging, exploiting chemical structure, microscopy, and many more. Therefore, scientists around the world are working hard to develop a material that could give maximum control over the propagation of light. Many limitations in the field of optoelectronic research are being eliminated by creating advanced systems based on photons instead of electrons, as in semiconductors. The photons are nothing but the bundle consisting of electromagnetic energy which can move in a dielectric material at a higher pace as compared to electrons movement in a metal wire. Photons are stable, have zero mass with no electric charge upon them. This gives rise to a new branch called photonics which is well known today and playing a major role in the development of advanced technology. Amongst the major factor governing the manipulation of light-matter interactions, photonic crystals are considered one of the best attractive materials. As the name

indicates, photonic refers to a branch of physics that includes the study of photonic emissions, detection & manipulation, and a crystal representing the periodic arrangement of atoms. Therefore, a photonic crystal can be considered as a periodic optical nanostructure consisting of repeating units of high and low dielectric constants in which the photons either pass through the structure or are completely forbidden depending upon their wavelength. This specific property allows one to control the light with good accuracy that is not possible with conventional optical technology.

Recent advancements in nanotechnology research have opened the possibilities to master the nanostructures obtained by the fabrication process through a self-ordering mechanism. In this regard, nanoporous materials such as nanoporous anodic alumina (NAA), porous silicon (pSi), and nanoporous titanium gathered a lot of interest from the research community. These nanoporous materials have been thoroughly exploited amongst other nanoporous materials specifically in the field of biosensing and drug delivery (Gulati et al. 2012)(Alba et al. 2014)(A. Santos et al. 2011). Amongst, the templates mentioned above, NAA emerges as one of the best materials as it can easily be obtained by inexpensive electrochemical anodization of aluminium (Al). In addition, it also has excellent biocompatibility, tuneable chemistry, controlled pore dimensions, and mechanical robustness which makes it one of the promising material to be used in drug delivery (Porta-i-Batalla et al. 2016).

Drug delivery, as the name suggests refers to a method of delivering the pharmaceutical compound onto the site of action with the main aim of achieving a therapeutic dosage. An ideal drug delivery contains the mechanism where the concentration of the drug remains higher at the targeted site and for a long period. Previously, conventional drug delivery methods

such as injections, formulations (ointments and creams), oral (capsules, pills, and tablets) were used. It was until the 1960s, the concept of a controlled and implantable drug delivery system (DDS) came into existence where several devices and implants were fabricated and modified for drug delivery within the body (Hoffman 2008). In the field of nano-biotechnology, one should remember that the complex mechanisms happening inside the human body take place in a regime going in a downward trend from the macro-level to the nano-level. Therefore, understanding the material properties at the nanoscale opens up several possibilities to understand the complex biological systems and physical and chemical interactions involved. Therefore, researchers all over the world are coming together in this multi-disciplinary field to investigate and develop advanced systems for drug delivery.

1.1.1 Objectives and Structure of this PhD Thesis

The main aim of this thesis is to develop a methodology through the advanced engineering of aluminium with the optimization of its structural parameters by an electrochemical process. As obtained structures are modified with different surface functionalization methods to improve the attachment of several biomolecules. To fill these advanced nanostructures with the drug, the drop-casting method is applied. The loaded NAA chips are thoroughly characterized to gain an in-depth understanding of the loading, and the release process in real-time using several optical methods such as UV-Visible, and reflectance spectroscopy.

The detailed objectives are as follows:

- Design and fabrication of advanced nanoporous anodic alumina architectures

- Optimization of nanoporous anodic alumina preparation method to be applied specifically for controlled drug delivery applications.
- Loading and analysis of the molecule infiltration by drop-casting technique for different nanoporous anodic alumina structures using simulation and experimental methods.
- Studying the influence of nano structuring of nanoporous anodic alumina and analysing the releasing behaviour of molecules in real-time.

The structure of the thesis is organized as follows:

Chapter 1 gives the background motivation required to pursue this PhD thesis

Chapter 2 demonstrates the state of the art which includes a brief history of nanoporous anodic alumina, its structural characteristics, and electrochemical processes involved. Once fabricated, the principle of different functionalization techniques involved for the modification has been described along with the different molecular loading techniques. A general principle of all the characterization methods used in this work is presented along with the model of the instrumentation applied to study the material. Finally, an overview of the applications involved for as prepared structure with the specific use in drug delivery application has been taken from a review paper entitled, **"Nanoporous Anodic Alumina Platforms for Drug Delivery Applications: Recent Advances and Perspective"** published in **Advanced Material Interfaces**.

Chapter 3 discusses a detailed description of all the types of NAA architectures prepared in this thesis. The whole fabrication setup is presented followed by the role of each part that makes up the setup. In addition, the details about the chemistry involved in drug loading and release profiles have

been elaborated as well. This section also discusses the strategies applied to gather information about the filling and releasing characteristics of drugs/dye from several optical techniques. To show the drug loading and release, numerical simulation of the optical properties of the nanostructures has also been discussed.

Chapter 4 provides detailed information about the fabrication process that has been optimized to produce NAA-GIFs with different lengths. Next, surface modification has been performed with different chemicals to hold the drug molecules inside the structure. Finally, a methodology has been shown to gather a better understanding of the drug loading and release processes in real-time. The results obtained has been shown in the final remarks section of the chapter and published in "Nanomaterials" journal as an article with the title, "**Optical Platform to analyze a Drug-Loading and Releasing Profile Based on Nanoporous Anodic Alumina Gradient Index Filters".**

Chapter 5 reveals the detail about the hybrid nanoporous anodic alumina gradient-index filters (Hy-NAA-GIFs) prepared through two different anodization techniques combined in one step electrochemical process. These structures were loaded with the doxorubicin (DOX) drug and the release kinetics in real-time have been reported by studying the influence of two parameters, i.e. different flow rates and pore lengths. The results have been discussed in the final remarks section of the chapter as well.

Chapter 6 summarizes and present the main conclusions and achievements obtained during this PhD dissertation. Also, it gives an overview of the possible applications where these nanostructures can be applied.

Chapter 2

State of the art

2.1 Fundamentals of Nanoporous anodic alumina

2.1.1 Historical Perspective

The history of the anodization process of metals started back in the 1920s when it was utilized for protection and decoration layers. When aluminium sheets/pieces were exposed to the air, it was observed that it led to the formation of a protective coating consisting of aluminium oxide (alumina) on the top of aluminium. This exciting phenomenon led many researchers to develop new ideas and study the material and its properties in detail. In 1923, Bengough and Stuart discovered and patented an electrochemical anodization method based on chromic acid to protect aluminium and its alloys from corrosion (Bengough and Stuart 1923). Just after this discovery, within ten years, i.e. from 1927-1937, Gower and O'Brien and Carboni mastered the art of electrochemical anodization in different acid electrolytes, a modified version of which is widely used today as well ((Italian Patent 741753, 1936).

After few years, Keller et al. used electron microscopy for the first time to characterize NAA and revealed that the structure consists of closely packed hexagonal arrays consisting of nanopores and barrier layer. Also, it was found that the interpore distance (D_{int}) is directly proportional to the anodization voltage (V), which served as a base to explore the physical and chemical properties of this material (Keller, Hunter, and Robinson 1953). Shortly after this, several efforts have been put towards developing the theoretical model to explain the mechanism behind the pore nucleation and growth process (Shimizu et al. 1991)(O'Sullivan JP and Wood GC 1970). During the late 1960s, Diggle et al. developed the first theoretical model to explain the formation process of aluminium oxide (Al_2O_3) (Diggle, Downie, and Goulding 1969). In the early 90s, Thompson and wood provided a more detailed understanding of the growth mechanism of anion incorporation in the

NAA through transmission electron microscopy and microtome section (Thompson and Wood 1983)(Wood et al. 1996).

During its early stages, the fabrication of NAA was restricted by the presence of a disordered alumina layer and a lack of information about the self-ordering process. In 1995, Masuda and Fukuda (H. Masuda and Fukuda 1995) discovered a two-step anodization process through which it became possible to obtain a highly ordered pore arrangement of NAA. By adjusting the anodization parameters, manipulating the geometrical characteristics of NAA became possible, which embarked on a new journey to fabricate cheap and highly reproducible nanoporous structures based on aluminium oxide with narrow pore size distribution and relatively high aspect ratio. Gradually, it became one of the promising materials to be applied in a wide range of applications. In 2002, Nielsch et al. refined this strategy by proposing an empirical rule that demonstrates that the self-ordering process of NAA requires a porosity (P) of around 10 % regardless of the main dominating parameters, i.e. type of electrolyte, anodization potential, and the anodization conditions applied (Nielsch et al. 2002).

Once the outstanding properties of NAA were discovered, several functionalization techniques were applied for a modification to obtain diversified nanostructures (Md Jani, Losic, and Voelcker 2013). Owing to its cheap fabrication process, stability, scalability, excellent mechanical and tuneable properties, it became one of the most promising materials in the scientific community until today.

2.1.2 Electrochemistry of NAA fabrication

According to thermodynamics, certain metals, when exposed to the oxygen (O_2) present in the air (equation 2.1) or water (equation 2.2), the surface of the metal is covered with a thin layer of natural oxide. This phenomenon can be

described by a change in significant negative Gibbs free energy (F Li 1998)(Araoyinbo et al. 2013).

$$2\,Al\,(s) + \frac{3}{2}\,O_2\,(g) \rightarrow Al_2O_3\,(s) \qquad \Delta G^0 = -1582 Kj.\,mol^{-1} \tag{2.1}$$

$$2\,Al\,(s) + 3H_2O(l) \rightarrow Al_2O_3\,(s) + 3H_2(g) \Delta G^0 = -871 Kj.\,mol^{-1} \tag{2.2}$$

The electrochemical process to obtain several NAA structures from aluminium usually occurs in an aqueous solution of oxalic, sulphuric, or phosphoric acid. The aluminium templates serve as an anode in this process, whereas platinum wire is used as a partially submerged cathode in an aqueous electrolyte. The electrochemical process is completed by applying the anodization voltage between the anode and cathode, as a result of which the pore nucleation starts and grows on top of the Al surface (figure 2.1).

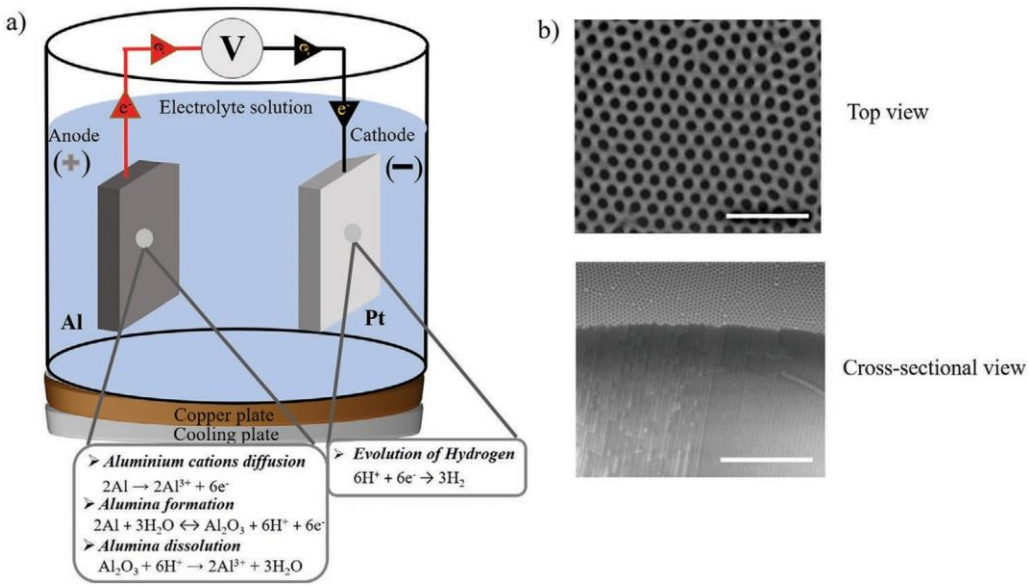

Figure 2.1: a) Fabrication process of nanoporous anodic alumina using an electrochemical setup. b) ESEM top and cross-section view (scale bars = 500 nm and 3 nm, respectively). Inset shows the chemical reaction that occurs during anodization.

From the kinetics point, the driving forces for the anodization of aluminium are mainly dependent on the ionic transport of Al^{3+} and O^{2-} across the aluminium-alumina interface, the barrier layer, and the alumina-electrolyte interface.

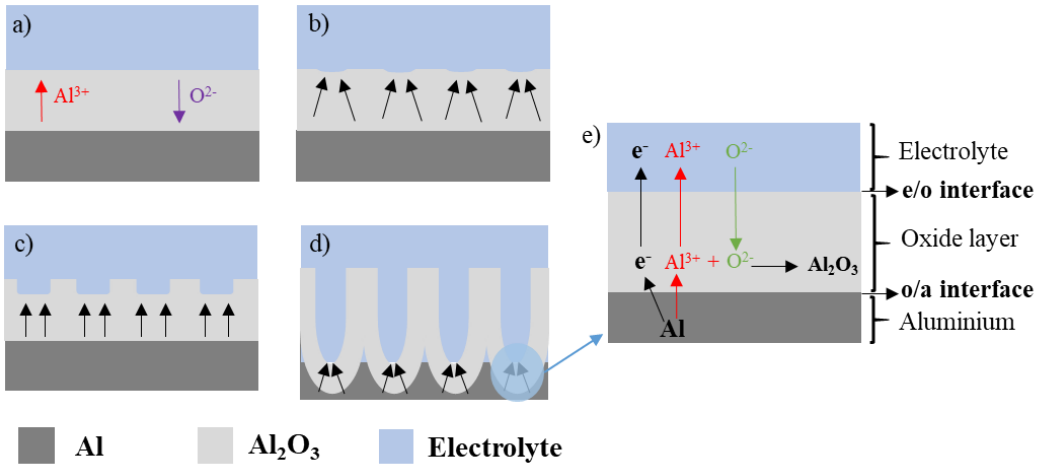

Figure 2.2: A simplified procedure for demonstrating the different stages of formation of pores, a) thin layer formation of Al_2O_3, b) dissolution of the oxide layer due to electric instabilities, c) process of achieving an equilibrium (formation and dissolution of Al_2O_3), d) steady-state growth of the pores, e) the magnified version of the blue circle in the figure (d) describing the passage of the main electrolytic species (Al^{3+} and O^{2-}) through the barrier layer.

As shown in figure 2.2, at the pore tip, several complex chemical reactions occur between the oxide/aluminium (o/a) and oxide/electrolyte (o/e) interfaces. The following equation relates to the formation of oxide:

$$2Al(s) + 3O^{2-} \leftrightarrow Al_2O_3\,(s) + 6e^- \qquad (2.3)$$

Correlating the figure (2.2.) and equation (2.3), the oxygen anions from the electrolytic solution passes through the e/o interface towards the o/a interface. This transportation results in the formation of an alumina oxide layer along

with the generation of free electrons. On the other hand, the aluminium cations extracted from the aluminium substrate penetrate towards the e/o interface due to an electric field where they are either passed onto the electrolytic solution or helps form oxide and water. This mechanism can be described in the form of the equation (2.4) below:

$$2Al^{3+}(aq) + 3H_2O(l) \leftrightarrow Al_2O_3(s) + 6H^+(aq) \quad (2.4)$$

On the other hand, the dissolution of the oxide layer tends to happen continuously at the e/o interface, where the protonation process of H^+ leads to the separation of the alumina into cationic Al and H_2O. In addition, an equilibrium is presumed to be occurring at the e/o and o/a interface present at the pore tips (equation 2.5).

$$Al_2O_3 + 6H^+ \rightarrow 2Al^{3+} + 3H_2O \quad (2.5)$$

The equation (2.4 and 2.5) mentioned helps to presume a constant dynamic exchange of ions between e/o and o/a interfaces at the pore bottom. As a result, the oxide layer is increased, and hydrogen cations are produced. At the same time, on the cathodic part of the system, there is a continuous reduction process of these hydrogen cations that generate a lot of free electrons. These hydrogen cations are then pushed away from the electrolyte and appear in the bubbles form. The whole reaction is described below (equation 2.6).

$$6H^+(aq) + 6e^- \rightarrow 3H_2(g) \quad (2.6)$$

In general, there are much more complex reactions involved during the anodization process of NAA. Therefore, only a basic introduction is provided along with the main equations to simplify and better understand the processes. The other chemical reactions involved can be found in more detail somewhere else (Feiyue Li, Zhang, and Metzger 1998)(Bard and Ketelaar 1976).

During the redox reactions (Eq. 2.3, 2.4, 2.5, and 2.6) occurring inside the electrochemical system, as obtained current density *(J)* is the combination of the cation (J_c), anion (J_a), and electron (J_e) current densities (equation 2.7):

$$J = J_a + J_c + J_e \tag{2.7}$$

The vital thing to know here is that the electron current density described above can be overlooked since the charges during the electrochemical process are predominantly regulated by Al^{3+} and O^{2-} due to the extremely low electrical conductivity of aluminium oxide. Therefore, equation 2.6 can also be rewritten as (equation 2.8)

$$J \approx J_a + J_c \tag{2.8}$$

The chemical reactions mentioned above can also be analyzed in the form of an anodization curve, where an abrupt decrease in the current density can be observed as the anodization process starts (figure 2.3, I). This decrease in intensity is due to the formation of an insulating thin and compact barrier layer of Al_2O_3 all across the aluminium surface. The applied anodization voltage primarily determines this thickness. Afterwards, due to local instabilities in the electric field across the barrier layer, the current density achieves its minimal value when pores start to nucleate at random places on the oxide film and then increases to their maximum value due to the dissolution of alumina at the localized areas (figure 2.3, II). Then (figure 2.3, III), several processes occur during which pores happen to grow, are eliminated, and sometimes joined together, as a result of which, a slight decrease in the *J* value is observed. At the final stage, the process achieves equilibrium between the formation and dissolution of Al_2O_3 and pore growth is observed in a steady-state (figure 1.3, IV).

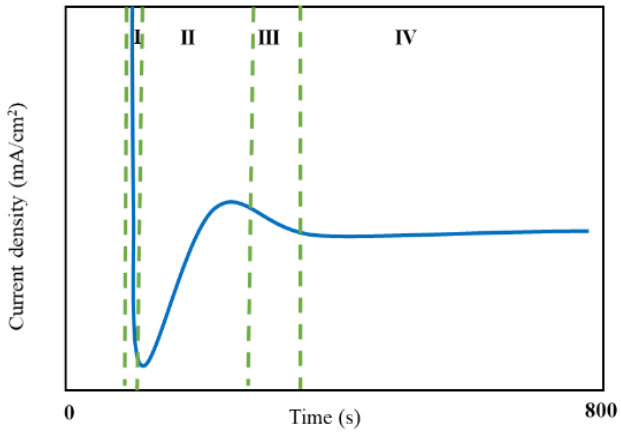

Figure 2.3: Typical current density vs time having four different regimes for pore growth under potentiostatic conditions.

During the anodization process, the chemical structure of NAA presents two primary interfaces: an inner layer and an outer layer. The inner layer is close to the aluminium-aluminium oxide interface consisting of pure alumina. In contrast, the outer layer lies between the aluminium oxide-electrolyte interfaces contaminated by the anionic species originating from the acid electrolyte (figure 2.4). Assuming the ordered pore growth during the NAA fabrication, usually, the ratio between the inner and outer layer is constant and independent of the type of electrolyte used (Nielsch et al. 2002)(Le Coz et al. 2010).

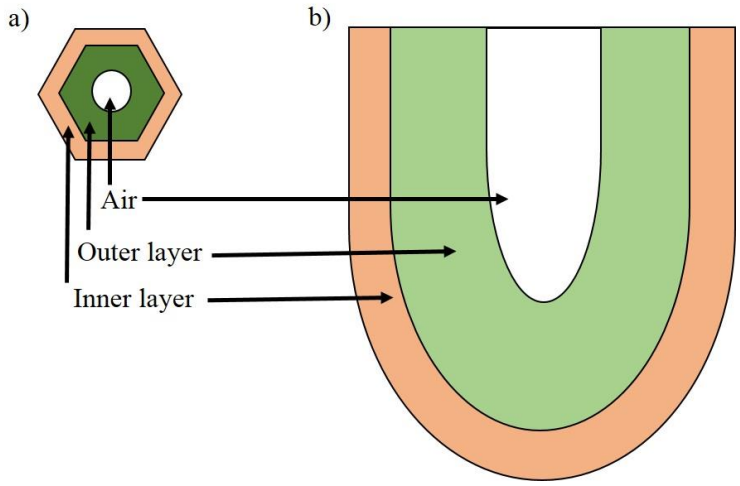

Figure 2.4: Schematic diagram of the pure inner layer and outer contaminated part of Al_2O_3 during anodization.

2.1.3 Anodization methods

The two widely used methods for obtaining NAA porous structures have been named mild and hard anodization.

Mild anodization (MA) refers to a process carried out under potentiostatic conditions by applying a constant potential and low current density (≈ 30 mA/cm^{-2}). Usually, in this process, there is a slow but linear growth of the NAA structure (1-3 $\mu m\ h^{-1}$). Furthermore, selecting the necessary anodization conditions (voltage, time, temperature, and acid type) along with the mild anodization process typically results in the manipulation of the geometrical characteristics such as pore size, thickness, and inter-pore distance.

On the other hand, an alternate approach utilizes higher voltages, leading to faster growth of NAA films and a high pore order arrangement called **hard anodization (HA)**. However, while performing the HA process, the current density value remains 1-2 order of magnitude higher than the MA process. As a result, the pore growth is not linear.

2.1.4 Anodization parameters and Structural Characteristics of NAA

Some of the crucial anodization parameters for fabrication of ordered NAA structure include anodization voltage (V), temperature (T), anodization time (t), pH, and concentration (C) of electrolyte. These anodization parameters have a significant influence on the structural characteristics of NAA structure which are pore diameter (d_p), porosity (P), barrier layer thickness (τ_{BL}), interpore distance (d_{int}), growth rate (R_p), and thickness (T_w) (O'Sullivan JP and Wood GC, 1970)(Feiyue Li, Zhang, and Metzger 1998).

One of the critical factors for obtaining the self-ordered NAA is anodization voltage confined for each electrolyte and its concentration used in the anodization process, otherwise, it might result in burning of the barrier layer, thus leading to the inhomogeneous pore growth arrangement or even destruction of the sample. The reasons include an increase in conductivity at the pore bottom due to local heating, breakage of the barrier layer due to cracks already present on the sample, and dielectric breakdown of aluminium oxide resulting in the generation of more electrons. The conductivity for most common electrolytes follow this trend: $H_2SO_4 > H_2C_2O_4 > H_3PO_4$.

Apart from the voltage, another important parameter, i.e. the interpore distance (d_{int}) (distance between the neighbouring pores), is directly proportional to the applied anodization voltage (equation 2.9). The relationship can be expressed as follows:

$$d_{int} = K_1 V \tag{2.9}$$

where K_1 is the proportionality constant, the value of which is in the range of 2.5-2.8 $nm \cdot V^{-1}$ for mild anodization process. Usually, for acidic electrolytes like sulphuric acid (20 V), oxalic acid (40 V), and phosphoric acid (150-195

V), an interpore distance between 50-500 nm can be achieved depending upon the type of electrolyte used (Lee et al. 2006).

Some of the electrolytes used to fabricate NAA with excellent pore ordered arrangement and inter-pore distance has been summarized below.

Table 2.1 shows all the details about different electrolytes used to fabricate NAA

Electrolyte	Concentration	Anodization voltage	Temperature (° C)	Inter-pore distance (nm)	References
Sulfuric acid	0.3 M	19–25	5	50-60	(Mir, Shah, and Ganai 2020)
Selenic acid	0.3 M	60-100	0	120-160	(Gordeeva, Roslyakov, and Napolskii 2019)
Oxalic acid	0.3 M	120-150	1-2	220-300	(Lee et al. 2006)
Malonic acid	5.0 M	120	0-1	300	(Ono, Saito, and Asoh 2005)
Tartaric acid	2-4 wt %	195	5	500	(Chu et al. 2006)
Malic acid	0.5 M	230	5	530	(Zajaczkowska, Siemiaszko, and Norek 2020)
Citric acid	0.1-1 M	250-460	10-30	1100	(Mozalev et al. 2005)

The temperature (T) of the electrolyte plays a crucial role and directly impacts the pore growth rate (R_p). To prevent the NAA structures from being dissolved during the process of anodization, the electrolyte temperature needs to be lower than the room temperature. The average temperature being used for the anodization processes with low voltages, i.e. sulphuric and oxalic acid electrolytes conditions, are between 5 and 20 ºC. For the anodization process requiring higher voltages (i.e. phosphoric acid at 195 V, mild anodization), the temperature should be close to 0 ºC to prevent the burning of the NAA structure due to the production of local heat at the bottom of the pores.

All the other electrolytic conditions described above, i.e. electrolyte type, pH, and concentration, serve as an essential factors in obtaining well-ordered porous structures. The type of acid used with the known concentration specifically for NAA anodization is usually limited within a specific voltage range. The higher the conductivity of the acid solution, the lower voltage should be applied to diminish the excessive heat production due to the Joule effect. For instance, highly conductive sulphuric acid electrolytes, at a particular concentration, only up to a maximum of 25 V or lower, must be applied. Similarly, for oxalic acid and phosphoric acids, the voltages are in the range of 40-70 V and up to 195 V, respectively. On the other hand, using an acid solution of low pH and a combination of low voltages leads to the generation of tiny pores and vice-versa.

The porosity (P) of the material can be explained in terms of the ratio of the surface covered with the pores compared to the overall surface of the substrate. For NAA, the P depends upon the anodization regime. For instance, P obeys the 10 % porosity rule under mild anodization processes, whereas in hard anodization conditions, P is around 3.3 % (Nielsch et al. 2002). It can be estimated by the equation (2.10) given below

$$P = \frac{\pi}{2\sqrt{3}}\left(\frac{d_p}{d_{int}}\right)^2 \quad (2.10)$$

It has been observed and reported before that during the anodization process, a thin and compact dielectric layer is formed at the pore bottom tip, knows as the barrier layer (τ_{BL}). It serves as one of the most critical parameters to gather more in-depth knowledge for the kinetic processes happening during the anodization process (Lee et al. 2006). The thickness of the barrier oxide layer is directly proportional to the anodization voltage and a proportionality constant (K_2) depending upon the anodization conditions and can be related by the following equation (2.11)

$$T_{BL} = K_2 V \quad (2.11)$$

In general, the NAA thickness (τ) is controlled by the anodization time. However, when the potentiostatic conditions are applied, NAA thickness does not grow linearly as the anodization time proceeds. Therefore, it is advisable to apply galvanostatic conditions to obtain a better control on the NAA thickness, since in this case, the relationship between (τ) and the charge (Q) is linear (Takahashi and Nagayama 1978) (Eftekhari 2008).

For simplicity to the readers, in this thesis, all the terminology describing PAA (porous anodic alumina) or AAO (anodic alumina oxide) has been renamed as nanoporous anodic alumina (NAA).

2.2 Introduction to Photonic Crystals

Some of the remarkable breakthroughs discovered in the past resulted in a more detailed understanding of several optical and electronic properties of materials. Specifically, tremendous developments have been seen in exploring the optical properties of materials, and efforts have been put in the direction of controlling the light-matter interactions.

One of the structures that have gathered enormous attention is photonic crystals (PCs) that can be defined as the periodic arrangement of dielectric structures capable of modulating light so that it allows them to block the propagation of light in a certain frequency range. This frequency range where the light is not allowed to travel is referred to as photonic bandgap (PBGs).

2.2.1 Light-matter interactions (Absorption, transmission, and reflection)

The interaction of light with the materials usually results in three significant optical phenomena: absorption, reflection, and transmittance. Absorption occurs when the light energy after hitting the surface gets converted into heat energy; reflection can be demonstrated as a process where the light is bounced back off the surface, whereas the transmission process occurs when the light passes through the material. All of these processes mentioned above depends on the optical properties of the target material and, precisely, the dielectric constant and complex refractive index

For most of the materials used, the permittivity is related to the complex refractive index, which can be defined as (equation 2.12):

$$\tilde{n} = n + ik \tag{2.12}$$

where n is the real value of the material's refractive index, k refers to the imaginary part of the complex refractive index or extinction coefficient. As known that refractive index of any material can be linked to the speed of the light travelling through a material by the following equation (2.13):

$$n = \frac{c}{v} \tag{2.13}$$

c refers to the speed of light, and v is the phase velocity of the light in that material. In figure 2.5, the imaginary part (k) is related to the absorption of light in a material. Two scenarios can happen k = 0, and the other one where k > 0. Furthermore, the figure depicts the behaviour of a waveform when it

enters into a transparent medium having k = 0 and k > 0. For k = 0, it shows a change only in the phase velocity of the light in which the amplitude remains the same as the light penetrates into the material, whereas when k > 0, a noticeable decrease in the amplitude of the waveform is observed due to the absorption of light. Usually, the transparent medium gives almost no absorption, so that the value of k can be considered almost insignificant.

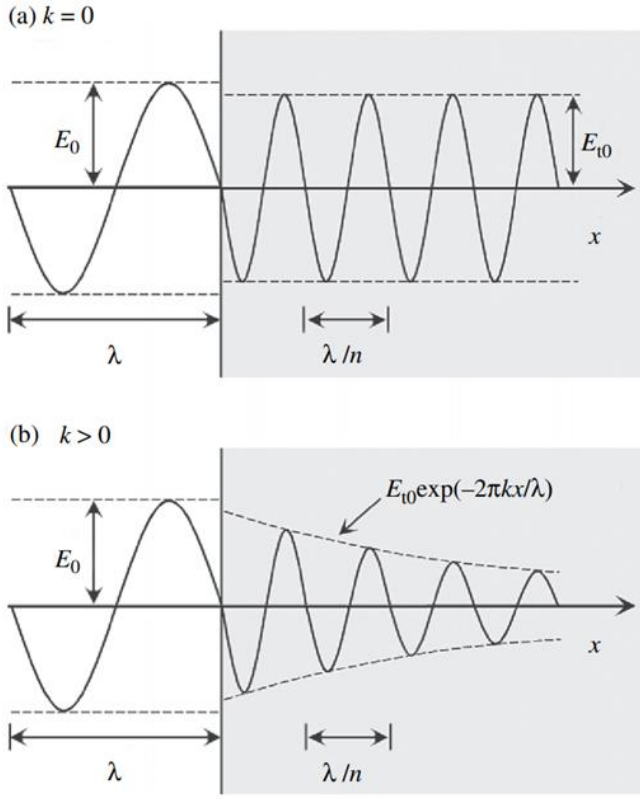

Figure 2.5: Light-matter interaction at the interface a) when k = 0, no absorption with a change only in the speed of light, b) k > 0, absorption process occurs leading to a change in the amplitude of light (Fujiwara 2007) Adapted with permission, Copyright (2007), Wiley books.

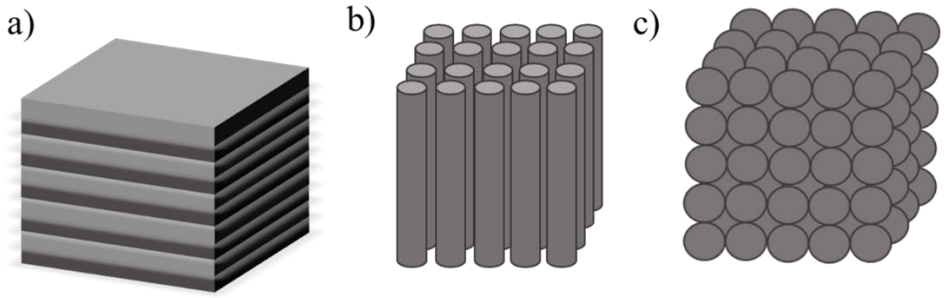

Figure 2.6: Schematic representation of different kinds of Photonic crystals, a) one-dimensional (1 D), b) two-dimensional (2D), and c) three-dimensional (3D).

PCs take benefit from the optical properties of the material to obtain the PBGs. The periodic variation that occurs in these dielectric structures leads to the formation of the structure in three different dimensions, i.e. one-dimensions (1D), two-dimensions (2D,) and three-dimensions (3D) (figure 2.6).

1D PCs as shown in figure 2.6 a) contains periodically alternating layers of two different materials having a refractive index of n_1 and n_2 along with the different thickness of a_1 and a_2, respectively. When incident light is shone on such a structure, each interface reflects some of the light. By appropriately choosing the thickness of each layer, the reflected beams can be combined to form a constructive interference along with a strong reflectance referred to as Bragg reflection. One of the most common examples is the distributed Bragg reflector (DBR). This unique reflection property of these structures is used widely in several applications, including optical filters (Qiang, Zhou, and Soref 2007), Fabry-Perot cavity (Velha et al. 2007), fiber Bragg grating (Nasu and Yamashita 2005) etc. Another most commonly used 1D PC used in the optoelectronic industry are rugate filters, details of which is explained in the next section.

2D PCs resemble a stack of 1D PCs displaying a single PBG distributed homogenously in the x and y-direction. There might be several geometries present for these types of structures, but they can usually be found either in the cylindrical or square form (figure 2.6 b). Different types of 2D PCs geometries can be used in several applications, including photonic crystal fiber (Cregan et al. 1999), and planar defect circuits (Pottier, Mastroiacovo, and De La Rue 2006) etc.

Similarly to 2D PCs, the **3D PCs** represents a stack of 2D PCs having periodic variations of the refractive index in all the directions of space (figure 2.6 c). This means that the incoming light vanishes evanescently as it is forbidden to propagate in all directions. Some of the typical 3D PCs include opals and inverse opals structures. Applications involved with these kinds of structures include micro integrated circuits (Jang et al. 2007) and advanced photonic applications (Arsenault et al. 2004) etc.

2.2.2 Rugate filters and their principle

Rugate filters (also known as gradient index filters (GIFs)) are optical filters made up of a dielectric medium where the structure shows a one-dimensional periodic and continuous variation in the refractive index resulting in the formation of photonic bandgaps. Compared to other optical structures, as in DBRs, where the variations take place in a stepwise manner, in GIFs, the variation is in sinusoidal shape.

To fabricate a rugate structure with a PBG designed at the desired wavelength (λ_0), it is pretty important to choose the sinusoidal profile carefully so that the resulting variation in the refractive index follows the same expression throughout the structure (Lorenzo et al. 2005):

$$N(x) = n_0 + \frac{\Delta n}{2} \sin\left(\frac{4\pi x}{\lambda_0}\right) \qquad (2.14)$$

where x demonstrates the coordinate and variations in the refractive index, n_0 stands for the average refractive index, Δn represents the contrast for refractive index, and λ_0 is the desired wavelength. As shown in equation (2.14) the central position of the PBG is extremely sensitive to the sinusoidal oscillations and upon the refractive index of the structure (n_0), which permits fine tuneability of the λ_0 or the oscillating frequency ($4\pi x$). Some of the widely used porous materials that utilize the rugate filters are porous silicon (pSi) and NAA, where the photonic properties have been exploited with diversity in a range of applications from sensing to drug delivery (Orosco et al. 2006),(Ruminski et al. 2010),(Law, Marsal, and Santos 2019).

2.3 Structural and surface modifications of Nanoporous anodic alumina

The attachment of the functional groups to the NAA surface aims to covalently hold several polymers, biomolecules, nanoparticles, DNA etc. (Abel Santos, Kumeria, and Losic 2014). Thus treatment with the functionalization substances mentioned above enhances the NAA surface along with preservation of its structure and morphology, which in turn can be helpful to prevent fouling and can be applied in biosensing (Amouzadeh Tabrizi, Ferré-Borrull, and Marsal 2020b) and drug delivery applications (Popat et al. 2004)(Porta-i-Batalla et al. 2016).

The surface functionalization of NAA is limited due to the presence of oxides and some other impurities caused by the preparation process (Han et al. 2007). One of the best strategies to overcome this limitation is to modify the surface by introducing different functional groups to improve the overall physicochemical properties of NAA.

Some of the best methods to modify the surface with different strategies and materials has been listed below.

Table 2.2 List all the essential modification strategies that can be applied for surface modification

Modification strategies	**Materials/templates**	**Summary**	**References**
Grafting	➢ Polyacrylic acid (PAA)	Hyperbranched structure excellent for covering the top of porous surface.	(Nagale, Kim, and Bruening 2000)
	➢ Poly(N-isopropylacrylamide) (PNIPAM)	Thermosensitive polymer widely known for its hydrophobic and hydrophilic switchable property at lower critical solution temperature.	(P. F. Li et al. 2009) (H. J. Wang et al. 2006)
	➢ Polystyrene sulfonate/poly-allylamine hydrochloride (PSS/PAH)	Easy modification along with high selectivity. Commonly used to entrap molecules inside nanopores effectively	(Porta-i-Batalla et al. 2016) (Dai, Baker, and Bruening 2006) (Krismastuti et al. 2015).
Chemical vapor deposition	➢ Carbon nanotube (CNT)/NAA composite ➢ NAA–carbon nanohybrid ➢ Chromium oxide (CrO_2) nanowire arrays assisted by NAA	Excellent technique to control thickness of desired coated material as compared to other techniques.	(Popp, Engstler, and Schneider 2009) (Rana, Kucukayan-Dogu, and Bengu 2012) (Fang et al. 2014)

Chemical vapor deposition	➢ Diamond-like carbon on NAA	-	(Q. Zhao et al. 2011) (Aramesh et al. 2014)
Thermal vapor deposition	➢ Platinum-coated NAA membranes ➢ Silver (Ag) nanocap arrays on NAA membrane	Simplest yet effective method used to improve chemical stability, conductivity, and magnetic properties.	(Cheow et al. 2008) (Nguyen, Ting, and Toh 2008) (Qiu et al. 2009)
Atomic layer deposition	➢ Iridium oxide (IrO_2) deposition inside NAA ➢ Pt and Al_2O_3 deposition on NAA membrane ➢ TiN–Al_2O_3–TiN composite inside NAA	Can be used for sequential and conformational deposition of several materials with controlled thickness over the NAA surface.	(Comstock et al. 2010) (Pardon et al. 2013) (Pitzschel et al. 2009)
Silanization	➢ 3-aminopropyl trimethoxysilane (APTES) ➢ Octadecyltrimethoxysilane (ODS)	A fast, effective, and reliable method to change the intrinsic as well as surface properties of NAA.	(Odom, Baker, and Martin 2005) (Mutalib Md Jani et al. 2009)
Electrochemical deposition	➢ Palladium nanoparticles (Pd) on the surface of NAA	Widely used to deposit several metals or composites over NAA surfaces. The main advantage includes ease of use	(Platt, Dryfe, and Roberts 2003)

Electrochemical deposition	➢ Gold (Au) nanoparticles inside NAA ➢ Nickel (Ni) and cobalt (Co) nanowires into NAA	and excellent transfer of materials as compared to other deposition techniques.	(Kondo, Nishio, and Masuda 2009) (Whitney et al. 1993)

2.3.1 Silanization of NAA structure

There are numerous functionalization methods reported so far to introduce active functional groups (for instance, carboxyl, amino, and hydroxyl) onto the surface of metal oxides (Biju 2014). Among them, Silanization chemistry is considered one of the effective and reliable methods to change the NAA's adsorption and wetting properties. The procedure followed is fast and straightforward apart from the suitability to perform at a moderate temperature without any heavy equipment. This simple procedure makes it one of the excellent strategies for several materials to be used in broad applications. The main principle behind this strategy is the condensation reaction that occurs between the silanol group (silane) and the hydroxyl groups (NAA in our case) that leads to the attachment of the silane groups on the surface. As a result, a stable bond forms on the surface of NAA and releases the free alcohol (OH) as the by-product of the reaction (Treccani et al. 2013).

Organosilanes are tetrahedral monomeric units based on silicon with a covalent or electrostatic linkage between the silicon atom and a carbon atom of another organic molecule (figure 2.7).

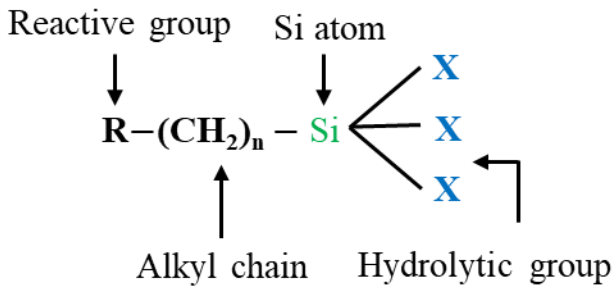

Figure 2.7: The general structure of the organosilane molecule with its reactive or functional and hydrolytic group along with carbon chain in the center and a tetrahedral core of silicon atom.

Different types of organosilanes are available, including PEG-silanes (Popat et al. 2004), amino (Guha Thakurta and Subramanian 2012), and fluorinated (Velleman et al. 2009). Amongst all the silanes mentioned above, enormous attention has been explicitly given to the amine groups of amino-silanes (Biju 2014),(Smuleac et al. 2005). Amongst the amino group category, the primary important ones are 3-aminopropyltriethoxysailane (also known as APTES), Diethylaminomethyltriethoxysilane etc.

APTES is frequently used to bond covalently on the surfaces of metal oxides (alumina, titania, and silica) for the attachment of lipids (Largueze, Kirat, and Morandat 2010), proteins (Baranowska et al. 2014) etc. The lack of secondary amines in the APTES structures makes them much more stable than other organosilanes.

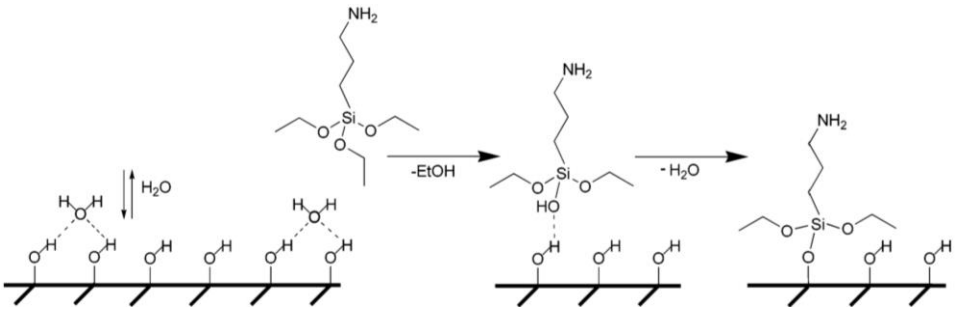

Figure 2.8: Schematic picture of hydrolysis mechanism of APTES followed by the condensation process at metal oxide surfaces (Howarter and Youngblood 2006) Adapted with permission, Copyright 2006, American chemical society.

In figure 2.8 the scheme shows the reaction of the APTES molecules with the hydroxyl groups (-OH) present on the surface of metal oxides and leads to the transformation of silane ethoxy groups (CH_3-CH_2-O-Si) to the silanol (Si-O) along with the loss of ethanol (CH_3CH_2OH) (Yamaura et al. 2004) (Howarter and Youngblood 2006).

The chemistry described above has been widely used for porous structures such as silica, and alumina. Usually, after obtaining these porous structures the surface itself contains some -OH groups because of the fabrication process. Just after this step, the treatment with APTES is performed for the immobilization of several molecules (Amouzadeh Tabrizi, Ferré-Borrull, and Marsal 2020a).

2.3.2 Assembly of Polystyrene Sulfonate/Polyallylamine Hydrochloride multilayers

Polyelectrolytes (PEs) are macromolecules consisting of dissociating groups in their repeating monomeric units. The electrolyte properties and the polymer

backbone are two of the critical constituents that build up the PEs structure. The structure can be divided into cationic (positive), anionic (negative), and amphoteric (both positive and negative) categories depending upon their charge. Most commonly used anionic groups are phosphonate ($–PO_3H^-$, $–PO_3^{2-}$), carboxylate ($–COO^-$), and sulfonate ($–SO_3^-$), whereas the cationic group primarily consists of primary ($–NH_3$), secondary ($=NH_2^+$), and quaternary ammonium ($\equiv N^+$). One of the essential properties of PEs is the ability of their functional groups to undergo the ionization process when placed in a polar solvent.

Based on the degree of ionization, polyelectrolytes can be classified into strong and weak polyelectrolytes. A weak polyelectrolyte consists of those polymers containing a weak acid and basic group and therefore depending on the pH of the surrounding environment, can easily lead to protonation or deprotonation. In contrast, a strong polyelectrolyte is usually not influenced by the pH. In addition, the classification of the polyelectrolytes can also be done based on pKa where PEs with the pKa values ranging between 0 and 14 can be termed as weak polyelectrolytes while those with less than 0 and greater than 14 falls under the strong category (Lyklema 1991).

Layer by layer (LBL) deposition of PEs onto the substrates is a simple and inexpensive method to obtain thin films with excellent tuneability (Decher, Hong, and Schmitt 1992)(Fares et al. 2019). These thin coatings can be referred to as polyelectrolyte multilayers (PEMs). There is alternate adsorption of charged anionic and cationic species in LBL methodology, which starts depending upon the charge a substrate possesses. Once known, the substrate is then dipped into a polyelectrolyte solution that is exactly the opposite of the substrate charge for adsorption of the PE layer. This step is followed by a rinsing step with deionized water to remove undesired or loosely bound

molecules from the surface. After that, the substrate is again dipped into the counter-ion polyelectrolyte solution, leading to the formation of the first bilayer (anionic and cationic) process. Usually, this step is repeated multiple times depending on the type of applications to obtain a multi-layered structure of PEs.

Some of the widely used anionic PEs are polyacrylic acid (PAA), and polystyrene sulfonate (PSS), whereas the cationic PEs is polyallylamine hydrochloride (PAH) (figure 2.9). The structure is described as below:

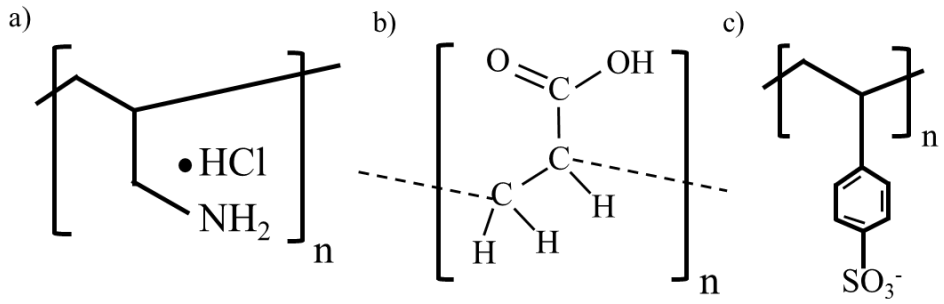

Figure 2.9: Schematic representation of the chemical structure of a) polyallylamine hydrochloride (PAH); b) polyacrylic acid (PAA); and c) polystyrene sulfonate (PSS).

2.4 Methods for loading of dye/drug molecules

Earlier treatments for drug delivery applications primarily consisted of the core-shell structures loaded with the drug molecules and a polymer film coating to prevent the early release. The main disadvantage, in this case, was the low amount of the drug-loaded into the structure since the area of loading is governed by the outermost layer covering the drug. Therefore, to overcome these limitations, porous structures were significantly explored over the past years due to their excellent drug loading capacity because of the high surface area to volume ratio (Ohta et al. 2005). Apart from this, porous materials offer

excellent biocompatibility, widely tunable in terms of chemistry, mechanically robust etc. Some of the methods through which the drugs onto these structures can be loaded are as follows:

2.4.1 Direct mixing method

To perform this method, the substrate is placed in a solution of a particular concentration of drug and allowed to stir for 1-2 hours, followed by the separation and drying process for 24 hours at 60-80° C. The method is widely used to load 2-deoxydadenosine, ibuprofen, ranitidine etc (Byrne and Deasy 2002)(Kang et al. 2007).

2.4.2 High-pressure loading method

It has been reported previously that pressure is one of the important parameters for efficient loading of the drug molecules inside the adsorbent (Domingo et al. 2002). Li et al. demonstrated the loading of Brilliant Blue inside hollow silica nanoparticles using a high pressurized loading procedure (Z. Z. Li et al. 2004). In this study, the drug solution is blended with the adsorbent material and placed in a high-pressure closed environment for 24 hours. This step is followed by the washing step to remove any undesired molecule. Afterwards, it can be dried in a vacuum for 5 hours at 65°.

2.4.3 Solvent evaporation

Usually, in this method, firstly, the polymer is dissolved in an organic solvent like dichloromethane (DCM), chloroform, etc., leading to the formation of an emulsion. After that, the solvent is evaporated either by using high temperature, stirring or in a vacuum. For instance, Sher et al. demonstrated the adsorption and loading study of ibuprofen from microporous polypropylene using two organic solvents, methanol and dichloromethane (Sher et al. 2007).

2.4.4 Drop casting method

It is considered one of the easiest methods for deposition of thin films, surface modification, or capillary filling of the porous substrates with drug molecules. This method involves a drop of the drug solution deposited on the top of the substrate either by using a dropper or a pipette. Once it dries, the same step can be repeated multiple times to either create a thin film or successive filling of the substrates. For this PhD thesis, we have applied and denoted this method as the Drop/dry method for the loading process of the cargo molecules inside the porous structures (Kumeria et al. 2013) (Kapruwan et al. 2021).

2.4.5 Vacuum loading

This method involves incorporating the adsorbent inside the drug solution followed by the evacuation process for the desired amount of time, after which the vacuum is released. Otsuka et. Al. used this method for the loading of the drug Phytonadione dissolved in chloroform and mixing it with a surface-modified silica gel followed by stirring for 6 hours. Thereafter, the obtained mixture was evaporated at room temperature under reduced pressure resulting in the formation of a powder that was then dried in a vacuum for 3 hours at room temperature (Otsuka, Tokumitsu, and Matsuda 2000).

2.4.6 Layer by Layer (LBL) deposition

This technique is particularly suitable for encapsulating the proteins, polypeptides, and poorly soluble drugs inside the porous structure. One example involves the LBL deposition of alternating layers of positive and negative polyelectrolytes on top of the substrates already filled with the drug molecules. This deposition leads to an electrostatic interaction between the layers on the surface, thus hindering the molecules from diffusing quickly (C. Wang et al. 2006).

2.4.7 Prolonged stirring in a drug solution

In this method, the substrate is placed in the drug solution for an extended period (24-72 hours) to thoroughly saturate the capacity of the substrate to hold the drug molecules inside, followed by a drying process. Since the drug is already loaded up to its maximum capacity, no vacuum treatment or stirring is required afterwards. Thus, this method can be used in almost all sorts of drug loading (Ohta et al. 2005).

2.5 Nanoporous Anodic Alumina Platforms for Drug Delivery Applications

Drug delivery refers to an approach that either includes formulations or a system that involves infusion of an active pharmaceutical compound inside the body and improves its safe transportation by controlling duration and place of release. An ideal drug delivery system (DDS) is where the drug concentration is maximum at the target site and remains constant for a longer time. In earlier times, this was performed with conventional drug delivery methods that included parenteral (injections), oral (pills, tablets, and capsules), or topical formulations (creams and ointments). Nearly a half-century ago, most of the drugs were designed into either capsule or pill formulations where the drug-loaded inside them used to release immediately upon contact with water without controlling the kinetics (Yun, Lee, and Park 2015). It was until Folkman et al., in the mid-1960s introduced implantable DDS and the first-ever zero-order release kinetics study by discovering that the passage of rabbit blood through silicone tubing filled with anaesthetic gases makes the rabbit asleep. This experiment successfully laid the foundation of an implant to be used as a drug-mediated carrier. He further added that a drug could replace anaesthetic gas, and eventually, it would release the drug at a constant rate (Folkman, Long, and Rosenbaum 1966). Unfortunately, conventional drug

delivery therapies require multiple dosages to maintain drug levels in the body. There is usually a rapid release of the drug directly into the blood circulation within a short time before reaching the desirable site, which might possess a risk of damaging healthy organs (Hoffman 2008). The main problem with these types of delivery vehicles includes poor patient compliance, lack of selectivity, unavoidable drug solubility, and biodistribution, along with unfavourable elution kinetics (Jain 2008).

With recent advances in nanofabrication technologies, drug delivery systems have achieved significant progress in terms of patient safety, bioavailability, and achieving required therapeutic efficiency (Ranade, Cannon, and Cannon 2011)(Silva 2004). As a result, two new branches, i.e., localized drug delivery systems (LDDSs) and targeted drug delivery systems (TDDSs), have emerged to efficiently deliver a drug inside the body using many nano-based drug carriers. These carriers include nanoparticles, liposomes, dendrimers, micelles, nanospheres, nanotubes, graphene (LaVan, McGuire, and Langer 2003)(Abel Santos et al. 2014). Both of these concepts have already been executed in clinical practices performing excellently in terms of cost-effectiveness, less painful technologies, controlled and reliable drug release profiles (Wolinsky, Colson, and Grinstaff 2012).

Amidst different categories of nanomaterials developed for drug release, inorganic nanoporous structures are the centre of attraction for most researchers today due to their ease of fabrication, cost-effectiveness, and ability to tune structural parameters precisely (Ferré-Borrull et al. 2014). In recent years, nanoporous anodic alumina (NAA), porous silicon (pSi), and titania were thoroughly investigated among all nanoporous materials specifically for developing new drug-releasing strategies due to their excellent physicochemical properties and biocompatible properties (A. Santos et al.

2011)(Alba et al. 2014)(Gulati et al. 2012). Among all the materials mentioned above, NAA remains one of the best choices due to its excellent chemical inertness, biocompatibility, enhanced mechanical strength, tuneable chemistry, and controlled pore dimensions and volumes for loading and releasing drugs in a controlled manner (Abel Santos et al. 2011)(Xifre-Perez et al. 2015)(Eckstein et al. 2018). In addition to its biomedical importance, NAA is also utilized in optical biosensing, energy production, and catalytic applications (Amouzadeh Tabrizi, Ferré-Borrull, and Marsal 2019)(Balderrama et al. 2015).

2.5.1 Biocompatibility of NAA

Several studies have demonstrated that biomaterials arouse the body's immunological response, altering their functional properties and action mechanisms (Morais, Papadimitrakopoulos, and Burgess 2010)(Trindade et al. 2016). Therefore, biocompatibility is one of the utmost parameters required for any biomaterial before its usage in real-life clinical practices. For example, Alumina (Al_2O_3) is a highly insoluble, nontoxic material widely used in dental and orthopedic treatments due to its bioinertness and excellent resistance (Aw and Losic 2016). However, some of the best uses of NAA are focused on their real-life clinical applications as implants, tissue, and stem cell engineering due to their high surface area, chemical stability, excellent topography, and high wettability. Therefore, enormous research activities have been carried out to understand the behaviour of NAA with different cell lines and tissues that include neuronal, connective tissue, epithelial, muscular, and blood cells (Haq et al. 2007)(Briggs et al. 2004)(Wolfrum et al. 2006)(Ishibashi et al. 2009)(Baranowska et al. 2014).

These studies prove that NAA offers excellent biocompatibility and does not provide a threat to neighbouring cells/tissues, and at the same time providing suitable cell attachment.

2.5.2 In Vitro Biocompatibility Studies

Extraordinary research to explore NAA in drug delivery studies was performed by Desai et al. where the team studied NAA capability thoroughly as cellular encapsulation to release immunoglobulin (IgG), glucose, and insulin. In this work, biocapsules consisting of nanoporous alumina membranes were developed using aluminium tubes as substrates. The potential use of these implantable biocapsules as an alternative treatment for type 1 diabetes was investigated. Pore sizes of 46, 58, and 75 nm were obtained using two-step anodization processes and filled with insulin-secreting MIN6 insulinoma cells within a collagen matrix. Results showed that the glucose molecules were actively released, while IgG release was significantly obstructed. Considerably, it was noted that the lack of nutrition inside the structure influenced the release of insulin. Results indicated that the release of insulin from these NAA biocapsules continued for up to 3 h, suggesting that the encapsulated cells could produce new insulin (Flamme et al. 2005)(Desai et al. 1999).

In another study by Karlsson and Tang, NAA membranes were prepared and subsequently coated with collagen I, serum, fibrinogen, IgG, and albumin to study in vitro cell viability of osteoblastic cells (MG63). Pore size-dependent responses were observed on protein-coated NAA membranes. The highest response in cell numbers was noticed when NAA membranes (20 and 200 nm pore size) were incubated with collagen I. On the other hand, cells cultivated on the fibrinogen-coated membrane were more viable on 20 nm than 200 nm structure; this was attributed to the physical characteristics, i.e., size and shape

of fibrinogen. It was also reported that albumin has more binding affinity to this substrate than IgG (Karlsson and Tang 2006). Pujari-Palmer et al. found that the nanotopographic surface of NAA has a significant impact on bone cells behaviour. NAA membranes with different pore diameters (20, 100, and 200 nm) and 60 µm thickness were taken in the study and tested for their osteoinduction and drug delivery kinetics. For cell growth study, bone marrow stromal cell lines (W20-17) were used and cultured on these nanoporous anodic alumina membranes. Alkaline phosphatase (ALP) expressions were measured to analyze the effect of different pore sizes on osteogenic differentiation in stromal cell lines. The potency of NAA to release an osteoconductive agent—bone morphogenic protein-2 (BMP-2) was also reported alongside. Also, an in-depth analysis was conducted based on the mechanism of cell proliferation, gene expression. The interaction of nanopores with cells has been depicted in figure 2.10 a), and b) where different cell morphology grew on different pore diameters (20 and 200 nm). On the one hand, the cells on the NAA membranes with a pore diameter of 20 nm were flat and round. In membranes with 200 nm, the cells were found to be in an elongated form. In figure 2.10 c) shows that the rate of cell proliferation was more on the control surfaces than NAA surfaces when analyzed with Alamar blue assay (figure 2.10 d). Not many significant differences were observed between alumina and control samples considering the proliferation rate among different pore diameters; Figure 2.10 e) shows higher ALP activity in cells on 200 nm membranes than 20 and 100 nm membranes after 14 days of culture. In terms of differentiation rate, figure 2.10 f shows that the differentiation rate was higher on the 200 nm membrane than 100 nm membranes without the addition of BMP-2 protein. No significant difference was observed for all the surfaces with the BMP-2 addition (figure 2.10 g); osteocalcin (OC) gene expression was found to be on the higher side on 200 nm membranes

compared to 20 nm surfaces, and the same pattern was observed when the cells were treated with BMP-2 (Karlsson and Tang 2006).

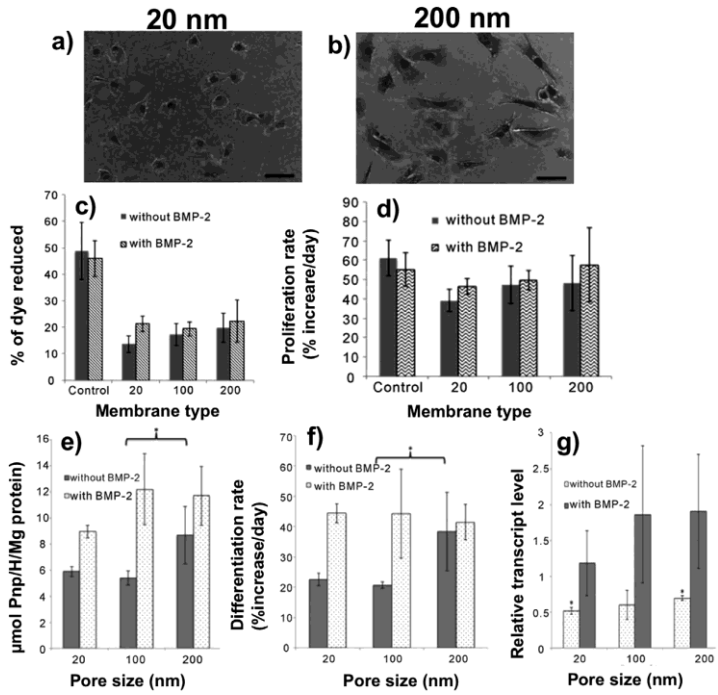

Figure 2.10: W20-17 cell morphology after cell culturing for 2 days on a) 20 nm and b) 200 nm. c) Alamar blue assay profile of proliferated cells after 7 days. Day wise analysis of increase in cell number from 2 to 7 days. e) Alkaline phosphatase (ALP) activity after 14 days of cell culture, with polystyrene as control and NAA (20, 100, and 200 nm), with and without the addition of BMP-2. f) Measurement of cell differentiation rate by analyzing the increase in ALP activity by time (12 days) from day 2 to day 14. g) OC gene expression with and without BMP-2 was analyzed at 14 days.(Karlsson and Tang 2006) Adapted with permission, Copyright 2014, Scientific

Research Publishing.

2.5.3 Cell Attachment on NAA Surfaces

The surface topography of NAA has attracted much attention in recent years, with many exciting research outputs put forward by researchers regarding the interaction between different cell lines and nanostructure surfaces. This, in turn, has enabled the development of new methods for enhanced cell culture processes with the possibility of deep understanding between cell adhesion, behaviour, and differentiation with regards to NAA surfaces. Titanium implants covered with a layer of NAA were prepared by Walpole et al. where aluminium was deposited onto titanium alloy, and subsequently, anodization was performed in 0.4 m phosphoric acid. The alumina layer was bonded to the titanium substrate via an interfacial layer consisting of dense anodized titanium oxide. To validate this coating process, mechanical measurements were performed to calculate shear and tensile strength, which was more than 20 and 10 MPa, respectively. The biocompatibility of this implant was examined against osteoblastic activity and its phenotype. It was observed that the NAA surface provides an excellent surface for osteoblast cell growth, but on the other hand, the osteoblastic phenotype was retained. NAA was placed in a cell culture medium along with the growing cells to analyze the dissolution rate. It was found that after 9 days of incubation, the membrane lost only 0.03% of its weight which is far below the toxic level. Enhanced biological performance was also reported by filling the porous structure with colloidal silica particles having a size of 20 ± 4.8 nm (Walpole et al. 2003). Hoess and co-workers (Friedmann et al. 2011) found that good cell growth conditions were obtained by cultivating hepatocytes cell line HepG2 on NAA membranes. The membranes were prepared to have pore diameters of 70 and 260 nm. Cell culture experiments demonstrated that the cells showed excellent

proliferation and adhesion on the NAA membranes for up to 4 days with normal morphology and no signs of toxicity. In addition, filopodia were found penetrating inside the larger pores with a diameter of more than 200 nm. The biomedical capability of NAA was tested against Vero cell lines, which belong to the kidney of Cercopithecus aethiops (African green monkey) (Poinern et al. 2014). Cell adhesion studies were conducted with in-house prepared NAA membranes, commercially available Whatman Anopore (Anodisc) membranes, and glass slides. Figure 2.11 a–c shows optical characterization after 24 h of cell interaction with all the substrates. In figure 2.11 d–f, field emission scanning electron microscopy (FESEM) images showed the presence of filopodia over the entire NAA surface, generating extracellular matrix (ECM) actively. It was reported that for the duration of the 72 h period, the cell proliferation rate was less for those cultured on glass slides than porous substrates.

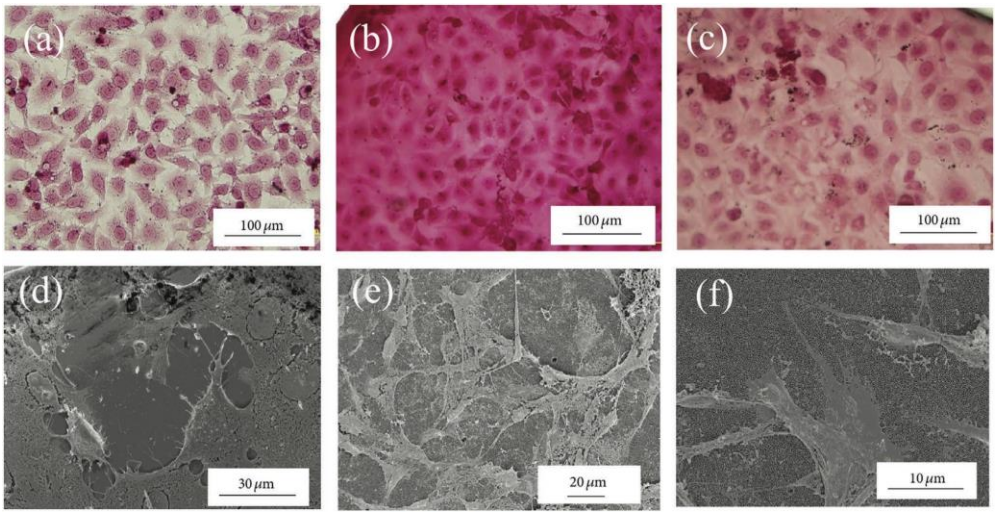

Figure 2.11: Optical characterization of Vero cells a) glass, b) Whatman membrane, and c) NAA in-house membrane, and SEM images at different magnifications d) glass, e) Whatman membrane, f) NAA in-house membrane.

(Poinern et al. 2014) Adapted with permission, Copyright 2014, Hindawi.

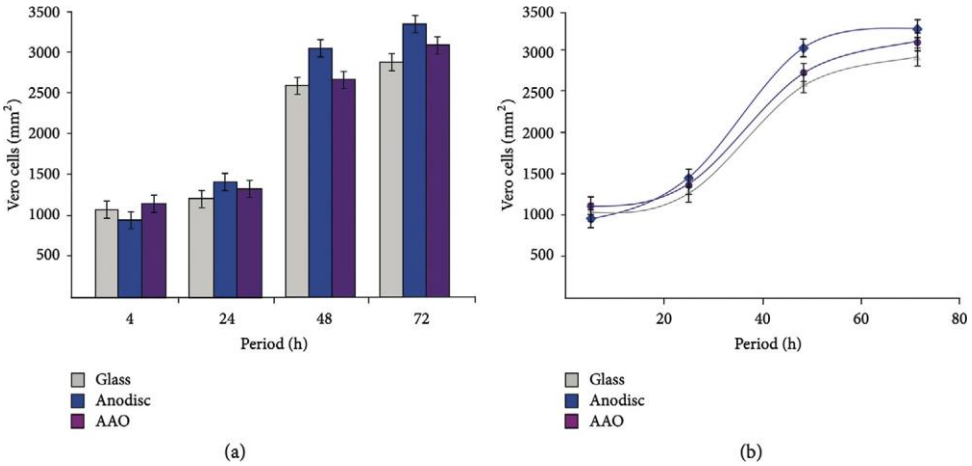

Figure 2.12: a) Vero cell proliferation study on three substrates after 72 h; b) comparison of Vero cell count against different substrates. (Poinern et al. 2014), Adapted with permission. Copyright 2014, Hindawi.

Also, there were no signs of any toxicity on the cells. To confirm Vero cell viability, a cell proliferation assay was performed, represented in figure 2.12 (a). It was found that at the end of 72 h, both the types, i.e., Anopore and in-house NAA membranes, were superior in terms of cell viability as compared to glass control (Figure 2.12 b).

In another study, to assess the proliferation and attachment of preosteoblast (MC3T3-E1) cell lines, Ni et al. fabricated NAA of different pore structures with pore diameters varying between 25 and 70 nm. It was found that after cultivating the cells for 7 days in a culture medium, in the beginning, moderate differences were observed in preosteoblast attachment, whereas the proliferation rate was found to be dramatically increased at the larger pore sizes i.e., 50 and 75 nm. It was reported that enhancing the osteoblast density

on the aluminium surface can be achieved by improving the surface roughness only and without any change in chemistry (Ni et al. 2014). Thakur et al. studied the living cells (vascular endothelial cells (ECV 304) response on the NAA surface to study the importance of pore depth. The cells were cultured on the nanoporous surface and after 1 day treated with polymerized actin in the presence of 3.7% formaldehyde. It was reported that for shallow pores (50 and 200 nm pore depth), the cells were found to be round with the presence of actin in an amorphous form throughout the cytosol distribution with no significant differences. However, on deep pores (2000 nm), the morphology and arrangement of the cells in its cytosol compartment solely depends upon the pore size (Thakur et al. 2012). To test the biocompatibility of different NAA structures, Wang et al. fabricated 600 nm long anodic alumina nanotubes (AANTs) through pulse anodization and conducted cytotoxicity experiments using Alamar blue and crystal violet assays (Y. Wang et al. 2014). Different concentrations of AANTs (1.56–100 μg mL^{-1}) were obtained for toxicity experiments carried out for 1–5 days on breast cancer cells (MDA-MB231-TXSA) and macrophage cells (RAW 264.7). It was demonstrated that even after 5 days, no toxicity patterns were observed in both the cell lines indicating that NAA tubes did not have any negative impact on cell growth and morphology (figure 2.13. a–f).

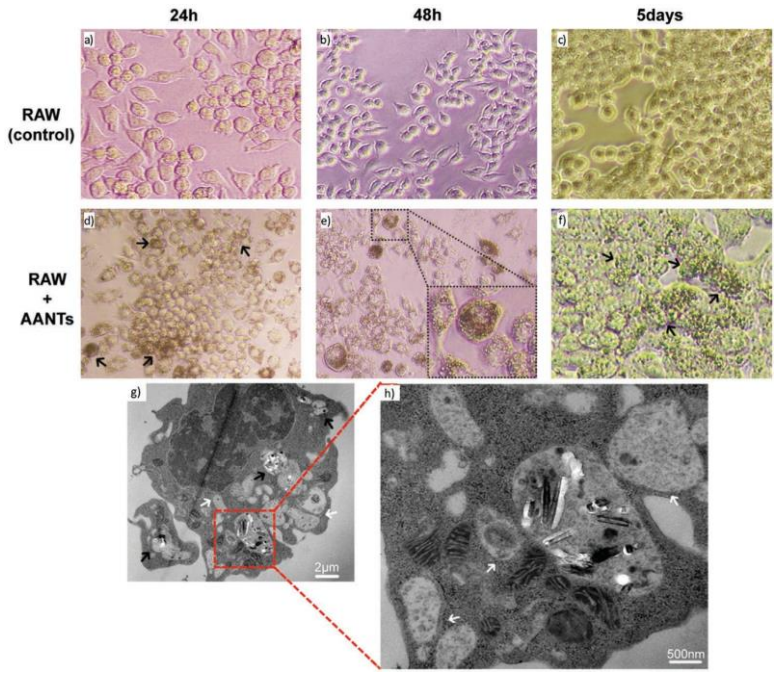

Figure 2.13: Optical characterization of AANTs (100 µg mL-1) after incubation with RAW 264.7 cell lines a), and d) 24 h, b), and e) 48 h, and c), and f) 5 days. Black arrows in (d)–(f) show that the cell is surrounded by AANTs along with the darker spot on the cells due to light refraction of alumina. g) TEM picture of internalized NAATs (100 µg mL^{-1}) by RAW 264.7 macrophage cell with white arrows denoting the blending of autophagic vacuoles h) enlarged view. (Y. Wang et al. 2014), Adapted with permission. Copyright 2014, Elsevier.

To see the interaction between AANTs and cell lines, transmission electron microscopy (TEM) examination was carried out as depicted in figure 2.13. g), and h). NAA tubes were seen inside the RAW 264.7 cells, where bonding of autophagosome with autophagic can be seen within the area highlighted. These results successfully demonstrate the uptake of AANT inside the cell. Similarly, another study was carried out with AANTs having lengths of 0.7, 2.5, and 5.8 µm fabricated through the pulse anodization process. It was shown

that all three different types of AANTs fabricated were taken up by the cells. However, AANTs with a length of 0.7 µm shows the lowest toxicity among all (Y. Wang et al. 2015).

2.5.4 In Vivo Biocompatibility Studies

Most of the research conducted using NAA as a template involves in vitro experiments, but when it comes to real-life applications, more in vivo and in-depth studies are required, which present profound challenges. In this regard, Wieneke et al. studied the effect of NAA coating on stents as a potential carrier for delivering the tacrolimus drug. In this study, 316 L stainless steel stents were covered with a thin layer of NAA followed by infiltration of 60 and 120 µg of the drug. Bare stents, coated stents, and drug-loaded coated stents were fabricated and implanted in the carotid artery of New Zealand white rabbits. Drug release was monitored by extracting whole blood at different time intervals and measuring with HPLC. It was shown that NAA-coated stents served as an excellent platform for loading and release of drug within the therapeutic range, followed by a significant reduction in neointima thickness (Wieneke et al. 2003). In addition, Rahman et al. demonstrated a novel method for ex vivo drug release in bones using the Zetos bioreactor (figure 2.14. a–g) (Rahman et al. 2015).

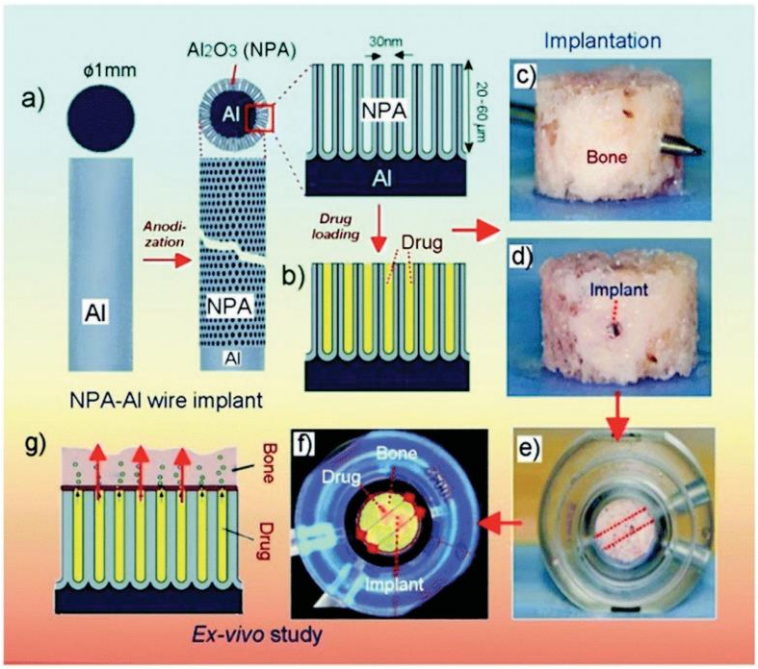

Figure 2.14: a-g) Schematic of fabricated and drug-loaded NAA implant insertion into ex vivo bone model and in situ fluorescence drug elution kinetics. (Rahman et al. 2015), Adapted with permission, Copyright 2015, Royal Society of Chemistry.

NAA implants with pore diameter (30–35 nm) and depth of 10–60 µm were fabricated. These NAA wires impregnated with rhodamine B (RB) dye were placed directly into the bone using needle puncture, and drug elution kinetics was measured by live fluorescence imaging. A biocompatibility study was also performed using human osteoblast cells, which responded with strong growth and adhesion to the NAA surface. Histology examination reveals the presence of live osteocyte cells and an insertion area demonstrating the harmlessness of the device to adjacent areas that make the system suitable for clinical practice. In addition, this approach did not have any impact on NAA and surrounding bone cells (figure 2.15. a–d).

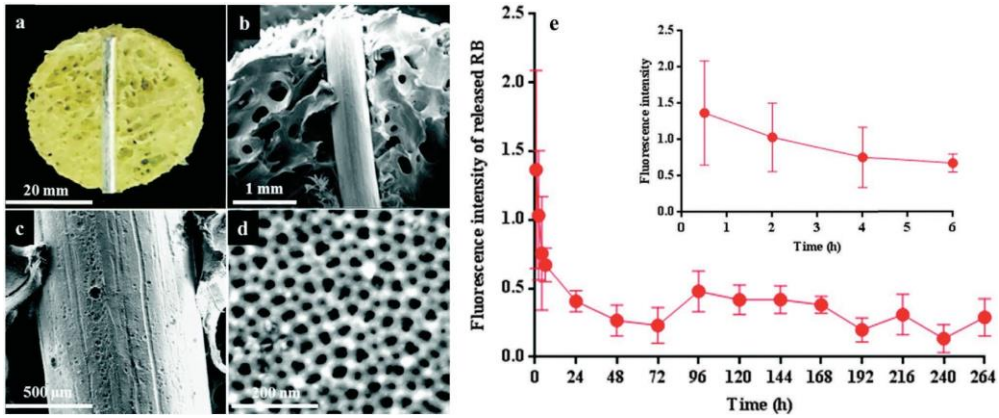

Figure 2.15: a) Digital image of the implant. b) SEM cross-section showing porous structure with an implant; c), and d) Homogenous surface morphology of NAA; e) Ex vivo drug elution kinetics from NAA implant (20.4 µm pore depth). Data represent mean and standard deviation from three replicates. (Rahman et al. 2015), Adapted with permission. Copyright 2015, Royal Society of Chemistry.

Different concentrations of drug profiles in bone were achieved, which showed the distribution of drug molecules from NAA implants in all directions. In addition, the results showed that by controlling pore length, it is possible to obtain an extended drug release profile (figure 2.15.e).

2.5.5 Stimuli-Based Strategies for Controlled Drug Release

Several protocols have been developed so far to release drugs in a controlled manner, but drug release remains inconsistent for the desired period. Therefore, to address the problem, new stimuli-based drug delivery systems based on NAA were introduced. As a result, several stimuli (pH, temperature, magnetic field, light, and ultrasound) triggered drug delivery systems have recently gained enormous attention (Abel Santos et al. 2014).

Although there are several procedures to fabricate different types of nanoporous anodic structures, the process usually results in crystalline lattice

defects, which promote nonspecific adhesion of several molecules on the surface leading to pore obstruction and biofouling. To overcome this challenge, Popat et al. reported the covalent modification of NAA surfaces with a pore size of 70 nm by polyethylene glycol (PEG) using PEG–silane chemistry. Different concentrations of PEG (10×10^{-3}, 20×10^{-3}, 40×10^{-3}, and 80×10^{-3} m) were used to demonstrate different grafting densities of polymer on NAA surfaces. In addition, the effect of different immobilization times (1, 2, 4, and 8 h) for 5×10^{-3} m concentrations was studied. To check the non-fouling properties, unmodified and PEG-modified alumina surfaces were tested against fibrinogen (1 mg mL^{-1}), and all the results were confirmed using X-ray photoelectron spectroscopy. It was reported that the thickness of the film was less than 2.5 nm and thus, unable to clog the pores, whereas with PEG-modified NAA surfaces, 70% reduction in protein attachment was achieved (Popat et al. 2004).

Jeon et al. developed an electrically responsive drug delivery system based on the NAA membrane. In this study, electropolymerization was done on the top surface of NAA membranes using polypyrrole doped with dodecyl benzenesulfonate anion (PPy/DBS). The main idea was to actuate pore size electrically by utilizing the drastic change in volume of PPy/DBS depending on the electrochemical state (figure 2.16). The pore actuation was confirmed with AFM images and later loaded with fluorescently labelled BSA. Apart from the fast switching time (less than 10 s), it was demonstrated that pores in the open state resulted in a high flux of drug from the NAA membrane, making this system suitable for emergency treatment of diseases like migraine and angina pectoris (Jeon et al. 2011).

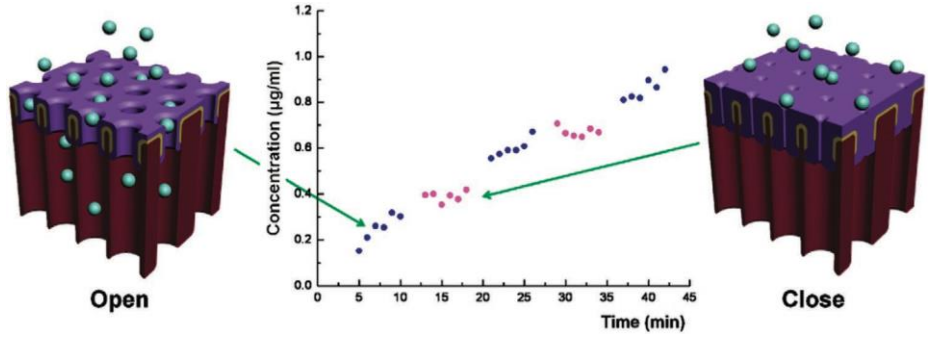

Figure 2.16: A schematic diagram of electrically responsive NAA membrane coated with PPy-DBS indicates a reversible pore opening reduction (drug release) between oxidation and reduction states (Jeon et al. 2011). Reprinted with permission, Copyright 2011, American Chemical Society.

In another study by Abelow et al., NAA membranes were coated with polypyrrole (PPy) and poly (3,4-ethylenedioxythiophone) (PEDOT) doped with chloride and p-toluene sulfonate (Tosylate) through vapour phase polymerization technique. Molecular diffusion rates of tannic acid were measured based on the oxidation or reduction state of the polymer. It was shown that the diffusion through these polymer-coated nanostructures was faster when the polymer is in an oxidation state while slower, being in the reduction state. The reason could be attributed to swelling/deswelling behaviour and the degree of confinement of polymer inside the porous structure (Abelow et al. 2014). Another pioneering study performed by Kumeria et al. reported the controlled photoresponsive molecular transport of Rose Bengal (RosB) dye across the nanoporous anodic alumina membranes (NAAM) using photoswitchable peptide (PSP). In this study, an azobenzene-derived peptide was immobilized along the internal part of 3-aminopropyl trimethoxysilane (APTES)-modified nanoporous channel for a change in effective pore diameter of the structure and subsequently, tracking the movement of dye molecules using a change in cis/trans configuration of the

peptide. The NAAM/PSP structure was first treated with light with a wavelength of 400 nm for 60 min, which resulted in low molecular transport; however, when the exposure was changed to 364 nm, an increasing trend was observed in the dye concentration due to change in the isomeric property. It was shown that exposing the structure to 364 nm wavelength leads to reversible switching in azobenzene structure from trans to cis isomer (Kumeria et al. 2015).

Noh utilized NAA nanotubes as a drug delivery reservoir for the widely used antibiotic Amoxicillin (≈8 nm). With the unique geometrical features of fabricated NAA, i.e., almost similar pore size and spacing between the neighbouring nanotubes (20 nm) and height of 38 µm, sustained-release was observed for nearly 5 weeks. The drug released from the pores was shown to be proportional to the square root of time calculated using the Higuchi model (Noh 2011). In a similar study, the controlled-release profile of another antibiotic, vancomycin, was achieved by Simovic et al., where NAA was decorated with biopolymer coating to reduce pore opening and closing. In this approach, the plasma polymerization tool was used to deposit a thin layer of polyallylamine on the top part of NAA, reducing the pore size by 5 nm (figure 2.17. a), and b). Three different periods (50, 120, and 200 s) of polyallylamine were deposited, and release was compared against samples without polymer deposition. It was shown that an increase in the deposition period of the polymer diminishes the drug release. On the one hand, where uncoated NAA samples eluted the drug within 45 min, the deposition of 50 s extended the release for up to 200 h, whereas for 120 s deposition, the release time period was increased to 500 h. Concerning the final deposition period, i.e., 200 s, within 500 h, only half of the drug was released, thus giving the possibility to tune pore size and control the drug release. Zero-order release was obtained after fitting the data into a zero-order equation (figure 2.17. c), and d). SEM

images have been shown in figure (2.17. e–h) without depositing polyallylamine and after the deposition time of 50, 200, and 300 s, respectively (Simovic, Losic, and Vasilev 2010).

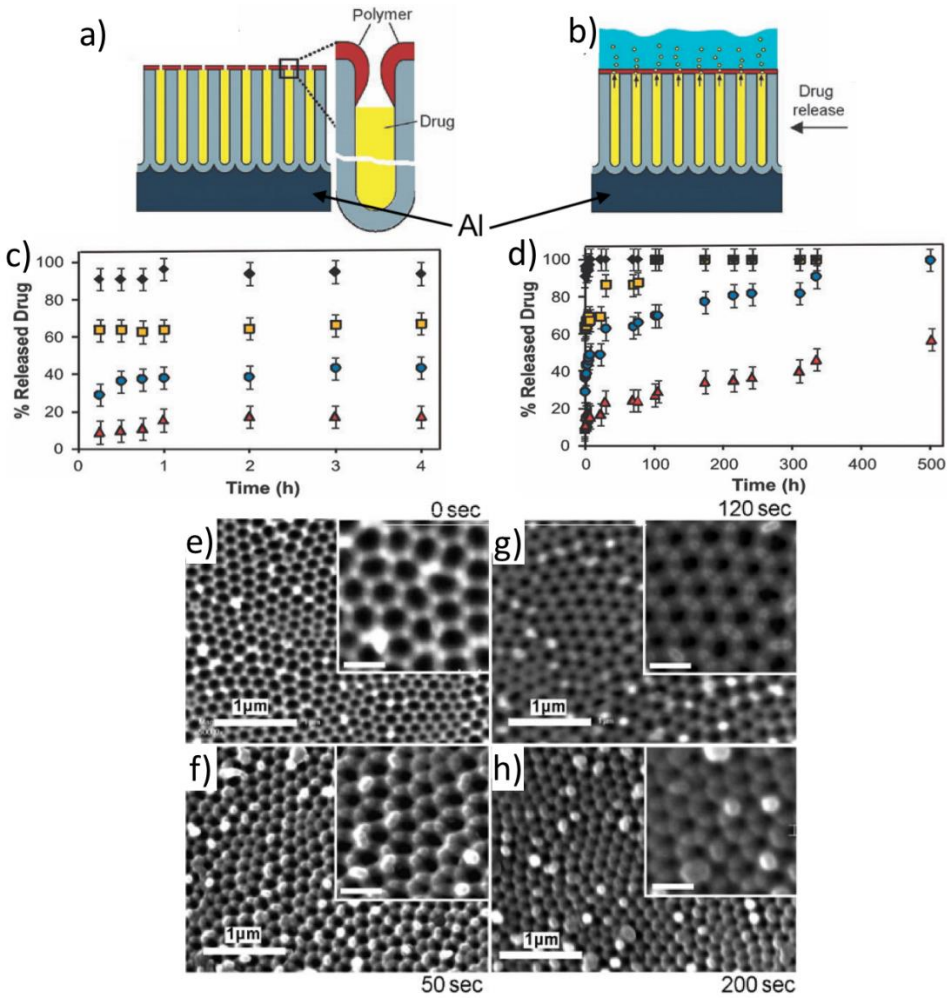

Figure 2.17: a) Schematic demonstrating the decrease in pore opening of NAA by deposition of polyallylamine using plasma polymerization tool. b) Diffusion of vancomycin from modified nanotube arrays into PBS medium. c,d) Controlled release profile of vancomycin from NAA without deposition and with controlled deposition time of 50 s (squares), 120 s (circles), and 200 s (triangles) for 4 and 500 h, respectively. e) SEM images without deposition

of polyallylamine and f–h) with deposition time of 50, 200, and 300 s, respectively. (Simovic, Losic, and Vasilev 2010), Adapted with permission, Copyright 2010, Royal Society of Chemistry.

Recently, Porta-i-Batalla et al. from our group reported a stimuli-driven drug delivery system using pH-responsive polyelectrolytes and NAA as a template. Drug release kinetics were evaluated based on a change in pH and the number of polyelectrolyte layers (Porta-i-Batalla et al. 2016). In brief, NAA was fabricated with two-step electrochemical anodization with a pore size of 130 nm and a depth of 15 µm. These uniform NAA structures were dipped alternatively in a solution of negative poly (styrene sulfonate) (PAS) and positive poly (allylamine hydrochloride) (PAH) to get two, five, and eight layers, respectively (figure 2.18. a–h). The dipping time of NAA in both the electrolytes was set to 30 minutes followed by 10 minutes rinsing in deionized water. Doxorubicin (DOX) was chosen as a model drug for this study. Polyelectrolyte-coated samples were placed in 1 mg mL^{-1} of DOX solution, and the pH was adjusted to 2.0 to increase the permeability of polyelectrolytes layers and for the fusion of DOX molecules inside PSS/PAH layers. Afterwards, pH was changed to 8.0 to cause contraction of the polyelectrolyte multilayers, which results in entrapment of drug molecules inside the films. The drug release profile was measured using photoluminescence spectroscopy in two different pH mediums 5.2 and 7.4, for over 5 days (figure 2.19.). It was demonstrated that DOX was released at a faster rate at acidic pH and was found to be in correlation with the number of polyelectrolyte bilayers. On the other hand, at alkaline pH, the drug release kinetics were not linear with the number of polyelectrolytes bilayers, suggesting that only the drug located near the release medium was released. To test the pH responsiveness of the system, a sudden change of pH was performed during the release, which led to another burst release confirming the same.

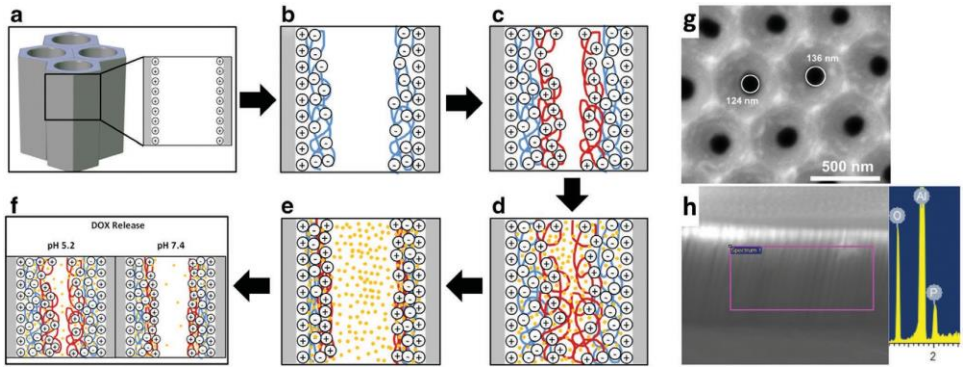

Figure 2.18: Schematic visualization of polyelectrolytes deposition in NAA structures. A) NAA pore walls were coated with positively charged APTES molecules. B) Deposition of negative PSS layer. C) PSS-coated NAA were dipped in PAH solution to get a positive layer; d) At pH 2.0, DOX loading into swollen multilayers. E) Confinement of DOX molecules due to contraction at pH 8.0. f) Release of drug molecules at different pH (5.2 and 7.4). g) SEM image of NAA pore diameter. H) Cross-sectional image of NAA with EDX spectra confirming polyelectrolyte deposition. (Porta-i-Batalla et al. 2016) Adapted with permission, Copyright 2016, Springer.

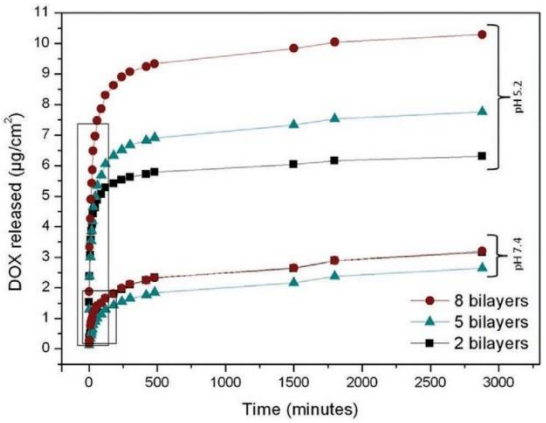

Figure 2.19: Drug release kinetics from NAA coated with different polyelectrolyte layers at different pH (5.2 and 7.4) with two different burst releases shown. (Porta-i-Batalla et al. 2016), Adapted with permission,

Zhao et al. recently developed a dual stimuli (pH and temperature) NAA membrane for controlled release of dexamethasone drug (X. P. Zhao et al. 2018). In this study, NAA membranes were fabricated by two-step anodization in which the first part was coated with biocompatible colipid and the remaining part was used for drug loading. FITC was coated selectively onto APTES-modified NAA and observed with laser scanning confocal microscopy (LSCM). The electrochemical behaviour of as-prepared NAA membranes was tested for pH responsiveness and temperature dependency using the voltammetry technique. The drug release measurement was performed using UV–VIS under different pH conditions (5.2, 6.4, and 7.4) and different temperatures (25, 35, 40, and 50°C). It was found that there was an increase in drug elution kinetics of about fourfold to sixfold at acidic pH and high temperature (50°C). To investigate the versatility of the NAA membrane, another anticancer drug (doxorubicin) was tested. No significant differences were found between the drug release kinetics of both the drugs, with higher release efficiency at pH 5.2 compared to neutral pH (7.4).

Chapter 3

Experimental

3.1 Experimental methods

3.1.1 Overview

This chapter reveals the experimental approach towards the fabrication of different photonic structures based on nanoporous anodic alumina. In addition, it also reveals the chemical modifications applied on to as prepared structures to enhance the surface chemistry followed by the measurements with different characterization techniques. To begin, the electrochemical setup used in the lab is illustrated with digital pictures to grasp a basic idea about the chemical process. The software that helps in continuous monitoring has also been shown with the input parameters. This step is followed by several surface treatments that have been listed in the subsections to modify the nanostructure for the real-time monitoring of the drug release. To confirm the modifications, all the characterization techniques involved have been elaborated as well. Finally, the transfer matrix method (TMM) has also been applied to obtain information about the changes in the optical properties of the nanostructured material as they are filled with a drug or as they release it.

3.1.2 Electrochemical setup

In this chapter, we provide a more detailed explanation of the configuration of the electrochemical cell used along with its components. Different anodization profiles with varying current (I) and voltages (V) have been applied to fabricate NAA structures controlled by the LabVIEW program. Usually, these types of programs are installed on the PC to monitor and control the anodization procedure. A high-speed GPIB-USB interface is required to communicate with the PC,

The fundamental part of an electrochemical cell consists of 3 main things:

1) Top cover (1.1 – 1.5)

2) Base reservoir (2.1 – 2.5)

3) Electrolyte

Table 3.1: showing the details of the top cover and base reservoir

1) Top cover of the electrochemical cell	2) Base reservoir of the electrochemical cell
1.1. Electric motor	2.1. PVC Container
1.2. PVC cover	2.2. O-ring
1.3. Teflon stirrer	2.3. Copper plate
1.4. Attached manual thermometer	2.4. A small hole to hold the sample
1.5. Spiral Pt wire coiled around Teflon	2.5. Cooling plate attached to the thermostat

Figure 3.1 a) shows the top cover of the electrochemical cell made up of moulded polyvinyl chloride (PVC) material **(1)**, through which a hole is drilled to place a thermometer inside **(2)**. PVC provides excellent insulation, chemical resistance to the types of acids used in this thesis (oxalic and phosphoric). Furthermore, a circular platinum wire serving as a cathode **(3)** goes through the plastics on the inside part, and a small part of this wire **(4)** is protruding to make a direct connection with the source **(5)**. A motor **(6)** is also attached to the top cover along with the Teflon stirrer **(7)** connected to a power source which is responsible for the homogenous stirring **(8)** during the anodization process. The whole electrochemical setup is designed so that the top cover is a little broader than the base, thus allowing it to be closed easily and perform the anodization. The base reservoir contains the sample **(9)** and the electrolyte. An O-ring **(10)** ensured the tightness and at the same time prevents leakage of the electrolyte from the chamber on the top of the PVC container **(11),** which is tightened to the copper plate **(12)** with the help of the screws. This copper plate serves as an excellent electrical/thermal base & thus in direct contact

with the cooling plate **(13)**. The copper plate has a hole that enables inserting a wire connected directly to the source (anode). Several anodization processes generate a vast amount of heat, and if not controlled correctly could lead to major changes in the pore geometry and structural variations and, in some cases, burning of the samples. To preserve the temperature inside of the electrochemical cell during the anodization process, a powerful thermostat **(14)** containing cooling liquid is distributed to the cooling plate with the tubes covered with the Armaflex rubber **(15)**. The whole anodization process mentioned above can be controlled by the LabVIEW software installed in the PC **(16)**. This program helps to construct multiple complex profiles of current density (J) and voltage (V) along with the constant monitoring and complete control on several crucial parameters such as total charge (Q) and anodization time (t).

Figure 3.1: Detailed photographs of the setup used for NAA fabrication; a) top cover made up of PVC motor, manual thermometer, and coiled Pt. wire (1-3, and 7), b) Completed electrochemical chamber with an outwards Pt. wire (4, and 6), c) base reservoir to hold the samples and liquid with a rubber O-ring

(9-11), d) Copper (Cu) plate with the screws (12) and L shape key, e) The electrochemical cell along with the power supply (K2400), computer setup, and attached thermostat for cooling with Armaflex rubber (5, 8, and 13-16).

3.1.3 LabVIEW Software

To monitor and record different anodization processes, a custom-made application based on the LabVIEW platform was designed. The utilization of this program helps to define crucial anodization parameters including total current charge or anodization time. The program is designed in such a way that if anything goes wrong during the process, it can be stopped immediately and restarted from the same point by recalculating the parameters. Figure 3.2 demonstrates a screenshot as an example with all the parameters included to obtain a sinusoidal structure in real-time.

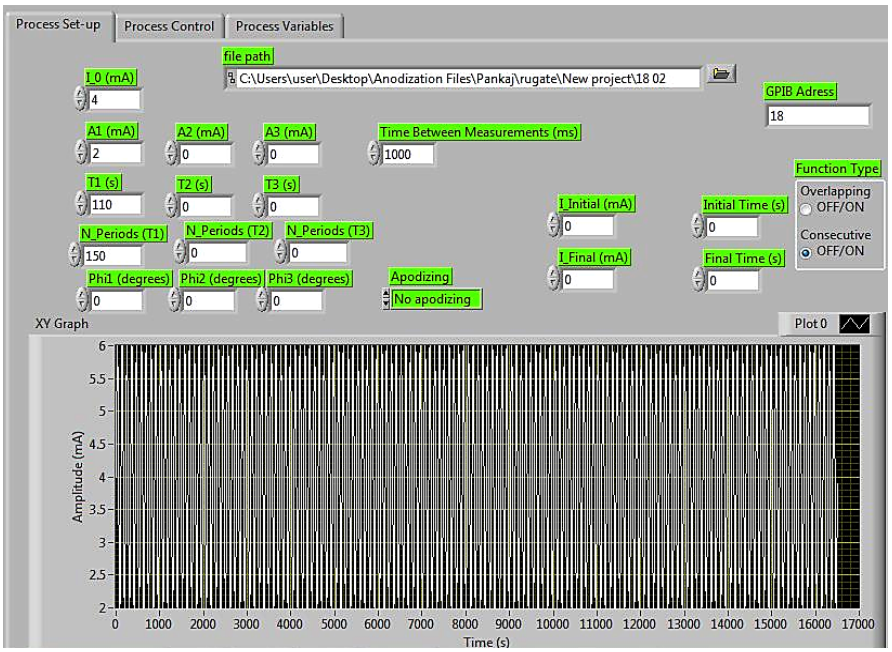

Figure 3.2: Digital photographs for the sinusoidal anodization profile with

different anodization parameters to obtain NAA-GIFs.

In addition, another screenshot (figure 3.3) has been captured that has been utilized in this thesis for the fabrication of straight channels by applying constant potential anodization.

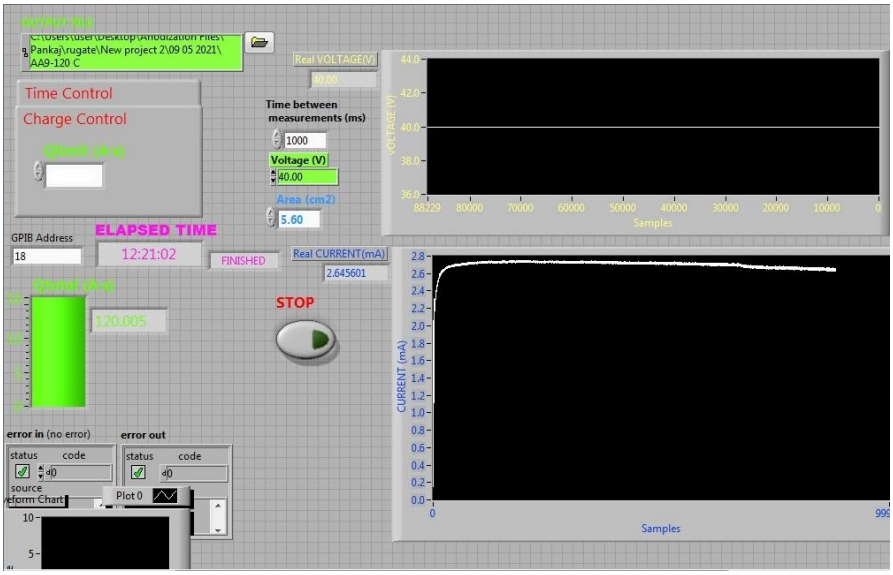

Figure 3.3: represents the current vs time curve obtained through constant potential anodization profile in real-time to obtain the bottom part of the Hy-NAA-GIF structure.

3.1.4 Commercial Aluminium foils

All the NAA structures prepared in this PhD thesis have been prepared using high purity aluminium foils bought from Goodfellow Cambridge Ltd. The detailed characteristics of the purchased Al foils are shown in table 3.2 below:

Table 3.2: Detailed characteristics of purchased aluminium foils

Characteristics	**Information**
Supplier	Goodfellow Cambridge Ltd.
Code	AL000650 (246-417-715)
Size	50 × 50 mm
Purity	99.999 %
Thickness	0.5 mm
Temper	As Rolled
Impurities (%)	Cu (0.3), Mg (1.2), Fe (0.3), Si (0.8)

3.1.5 Electropolishing of Al substrates

As obtained, commercial Al sheets have a lot of surface roughness which hinders the ordered pore growth and arrangement of NAA during the anodization process. Therefore, a pre-treatment step called electropolishing is applied to make the NAA surface more homogenous. Before starting the electropolishing process, the Al substrates are cleaned in a sequence of acetone, ethanol, and water to remove impurities from the production process. After that, the aluminium (anode) and Pt wire (cathode) are submerged in a mixture of perchloric acid ($HClO_4$) and ethanol (EtOH) with a ratio of 1:4 (v/v) at 20 V for 4 minutes at a temperature of 0° C. Alternating stirring was used with the change in direction at 300 rotations per minute after every 60 s to ensure the smoothness. After completing the process, the substrates are adequately rinsed with EtOH for 2-3 minutes, followed by the rinsing with deionized water (Purelab Option-Q, 18.2 MΩ-cm) followed by air-drying for 30-60 seconds (figure 3.4).

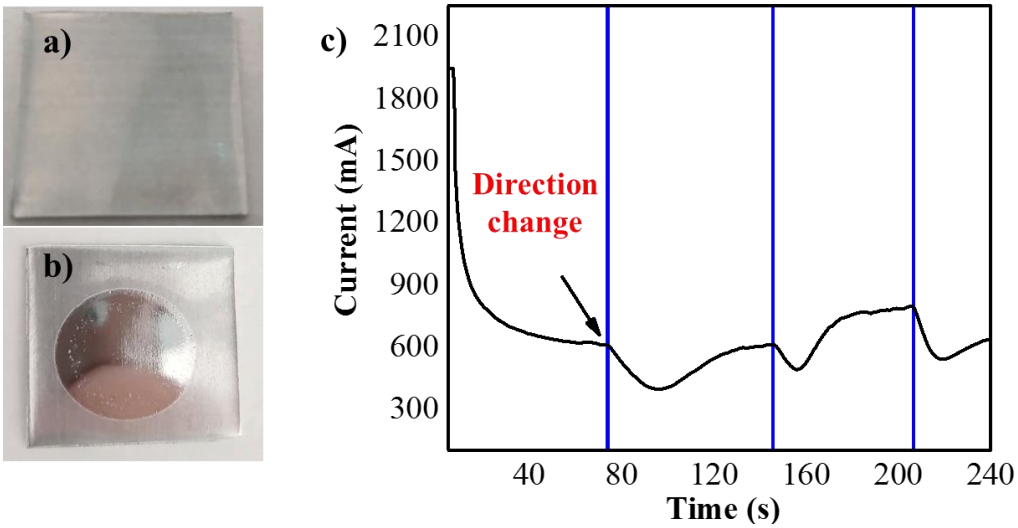

Figure 3.4: Digital photographs of the before and after electropolishing effect of the commercially purchased aluminium substrates, a) without electropolishing, b) with electropolishing, c) represents the graph representing the current-time transients for the electropolishing procedure applied for 4 minutes.

3.1.6 NAA-GIFs fabrication

The fundamental introduction for the GIFs has already been explained in chapter 2, section 1.2. Amongst all the optical structures, NAA-GIFs represents a particular class where an intense and narrow band can be achieved by the periodic modulation of the effective refractive index, which can then be further tuned for multiple applications, including bio-sensing (Law et al. 2018), photocatalysis (Lim et al. 2018), lasing technology etc. (Hideki Masuda et al. 2006). Although there are numerous methods to obtain NAA-GIFs, in this PhD dissertation we have mainly focused on the fabrication process through the one-step anodization protocol mentioned in here (Acosta et al. 2019). The conditions applied and surface modifications processes are briefly introduced in the following sections. The primary in-depth strategy to apply

these modified NAA structures has been shown in chapters 4 and 5 along with some conclusive analysis.

To obtain NAA-GIFs structure, a single step modified anodization process was followed. In this procedure, after the electropolishing step, the aluminium substrates were placed in an electrochemical cell with a solution of 0.3 M oxalic acid at 5°C under controlled stirring. After that, the anodization process was started by applying a current density-time sinusoidal anodization profile according to the following equation:

$$J(t) = J_1 \times \left[sin\left(\frac{2\pi}{T_i} \times t\right)\right] + J_o \quad (3.1)$$

where $J(t)$ refers to as current density at time t as a function of J_1 (current density amplitude), T (time period of sinusoidal signal), and J_o(offset current density).

3.1.7 Hybrid nanoporous anodic alumina gradient-index filters (Hy-NAA-GIFs) fabrication

This section explains an approach where two different anodization regimes are combined in one process to obtain Hy-NAA-GIFs structure. The types of anodization applied are sinusoidal current-density and constant potential anodization. To start fabricating the structures, the aluminium firstly was electropolished similar to the protocol mentioned in section 3.2.3 above. This step was followed by treatment of the polished aluminium with the sinusoidal current-density anodization having 0.3 M oxalic acid under controlled stirring at a temperature of 5.5°C. This anodization profile was controlled based on the following equation (3.2):

$$j(t) = j_0 + j_1 \cdot \sin\left(\frac{2\pi}{T} t\right) \text{ for } 0 < \text{t} < \text{N} \,.\text{T} \quad (3.2)$$

where *j(t)* corresponds to the current density at time (t), j_0 and j_1 are the average current density and the amplitude of sinusoidal current density variations. *T* represents the time period of the sinusoidal variations and N is the number of cycles applied.

Once it finishes, without dismantling the cell, constant potential anodization is applied for a desired amount of time. Figure 3.5 shows the pore length vs charge curve obtained for Hy-NAA-GIFs to prepare different length structures at the bottom by applying controlled charge through the system. The charge values obtained were 4.7, 7.3, and 32.5 C for short, medium, and long Hy-NAA-GIFs samples.

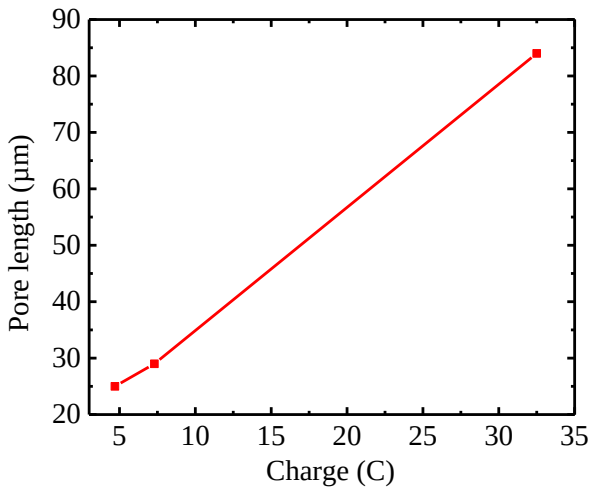

Figure 3.5: the curve shows the total amount of charge required to obtain different pore lengths at the bottom part for Hy-NAA-GIF.

3.2 Post-treatments

3.2.1 Pore widening (PW)

One of the most convenient ways to gain control over the porosity of NAA structures is through the pore widening (PW) method. To achieve this, the

samples are placed in a wet chemical etchant of 5 wt % phosphoric acid at 35° C for a different amount of time to attain the structure with different porosities. Figure 3.6 displays the SEM images obtained for NAA structures after the pore widening process with a pore diameter of 30 nm for 0 min, 39 nm after 10 min, and 45 nm after 15 minutes.

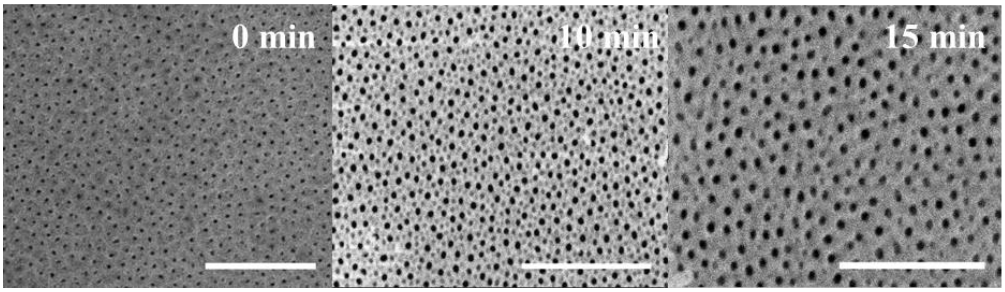

Figure 3.6: SEM pictures obtained after the treatment of NAA with phosphoric acid with the treatment time of 0, 10, and 15 min. respectively (Scale bar = 1 μm).

3.2.2 Polyelectrolytes deposition

A general introduction to different types of polyelectrolytes has already been provided in chapter 2 (section 2.3.2). They are widely used nowadays due to their ease of preparation and compatibility with varieties of substrates. In addition, it has been reported previously that the multilayers are capable of diffusing inside the nanoporous structures effectively thus enabling one to obtain several polyelectrolytic multilayers for trapping the molecules in a simple manner.

In this thesis, two different types of polyelectrolytes are being used, namely, PSS and PAH, for entrapment of the molecules inside the NAA. The polyelectrolytic solutions were prepared in 1 mg/mL in 5 mM $CaCl_2$ in deionized water. In brief, different types of NAA substrates were prepared and

dipped consecutively in a solution of PSS and PAH for 30 minutes followed by washing with deionized water in 10 minutes to obtain several multilayers.

3.3 Characterization techniques

A lot of optical techniques has been applied to investigate the light-matter (NAA in this case) interactions, such as Raman spectroscopy, surface plasmon resonance (SPRs), optical waveguides, photoluminescence (PLS), UV-Visible spectrophotometer (UV-VIS), and reflectance spectroscopy (RS) (Ferre-Borrull et al. 2015). To study the structural and morphological characteristics, SEM has also been performed to obtain the top and cross-sectional images for all the samples. In the previous years, numerous findings were reported based on the remarkable features and diversified properties of NAA, ranging from electrochemical sensors to drug delivery, molecular separation process, etc. The optical methodology serves as an excellent tool to analyze and modify the strategies in several situations without damaging the sample or causing any change in the surface properties. When combined with the NAA, this technology provides a wealth of information to be applied in a wide range of applications (Md Jani, Losic, and Voelcker 2013).

For the context of this PhD dissertation, the interaction of light with NAA has been studied mainly using Fourier transform infrared spectroscopy (FT-IR), UV-VIS, PLS and RS.

3.3.1 Electron Microscopy

Electron microscopy refers to a technique that utilizes an electron beam as a source of illumination, a sample stage (where the beam of electrons interacts with the sample), detectors (for monitoring the signals obtained through sample-beam interactions) and displaying system (to build up and see the processed images from the signal). The apparatus consists of an electron gun

situated at the top to generate the electron beam that emits electrons towards the samples with energy ranging from a few tens to thousands of electron volts. Usually, the electrons, when passed out from the gun, appear as a divergent beam which is then directed to a series of lenses and apertures to focus onto the spot available on the sample surface.

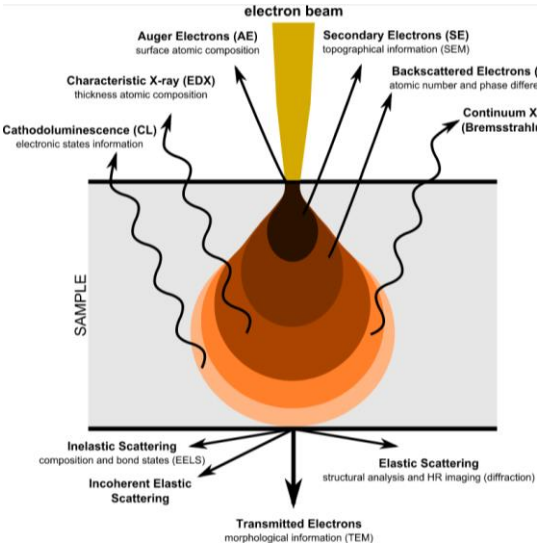

Figure 3.7: represents the interaction between an accelerated electron beam and a sample through the pear model (Dr Rudolf Winter, accessed 29 May 2021).

When the electron beam interacts with the sample, it experiences a pear-shaped distribution of the electrons on the surface and can penetrate in depth up to a micrometer range below the surface (figure 3.7). Due to these electron-matter atom interactions, several signals are discharged (inelastically or elastically scattering of electrons, light emission (cathodoluminescence), Auger electrons, etc.) and collected by a detector. Since the system uses a high electron beam and not photons, high-resolution images can be obtained easily.

It is an essential tool for analyzing surface morphology, crystal orientation, defects, elemental composition, etc. (Egerton, Li, and Malac 2004).

3.3.2 Environmental Scanning Electron Microscopy (ESEM)

ESEM is one of the most convenient and widely used techniques to obtain high-quality images of the samples, as the name suggests; in ESEM, the environmental stands for the extended version of SEM with a less tedious sample preparation process. The word scanning refers to a way of producing images. The main principle remains the same as in an electron microscope, where the surface of the sample is bombarded with the focused electron beam, and once the electron-matter interactions take place, wide varieties of signals are generated, which are then captured by the detector and sent for processing. In this case, the detector deployed is a kind of Everhart-Thornley detector, collecting the signals from back-scattered electrons. While the overall instrumentation inside ESEM is similar to a standard SEM, the main difference lies in the electron beam generation. In a typical ESEM, the electron beam is produced under vacuum while the samples chamber consists of high-pressure gas. This setup (figure 3.8) was required for a successful demonstration of samples measurements in wet or non-wetting conditions without any further modifications.

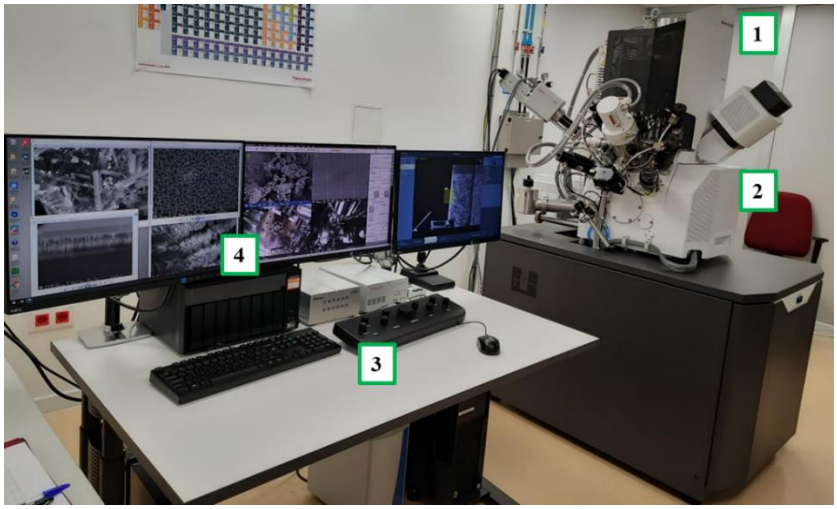

Figure 3.8: Digital photograph of FEI Quanta 600 used for this PhD: 1) Electron beam position, 2) sample stage, 3) controlling equipment, 4) PC setup to view the images.

3.3.3 Photoluminescence spectroscopy (PLS)

PL spectroscopy is a non-destructive, contactless method to obtain information about the optical and electronic properties of a material. In this technique, light is illuminated onto a sample, gets absorbed and the photoexcitation process takes place. This photo-excitation phenomenon drives the molecules to reach from ground state to excitation state. When returning to the ground state, they emit excess energy in the form of photons. These photons are then collected by the detector and converted into graphical form to analyze the information about the luminescence process. This type of spectroscopy is widely used in analytical and biological chemistry to demonstrate the behavior of molecules (figure 3.9).

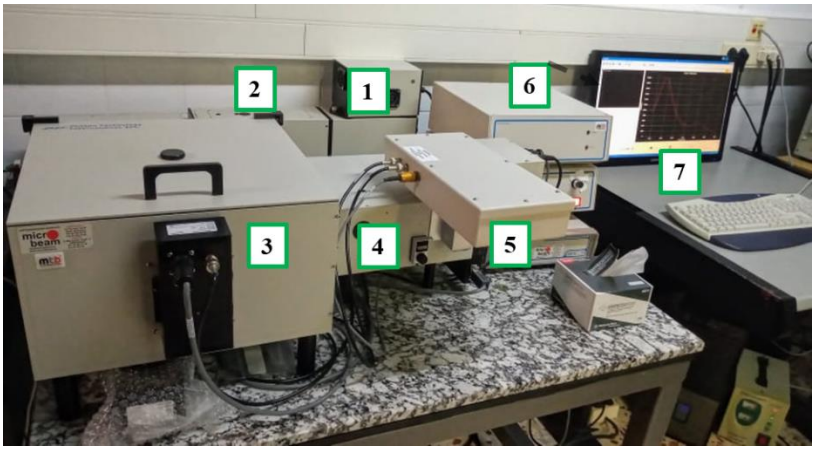

Figure 3.9: Quantamaster 400 Photon Technology International spectrophotometer used in this PhD thesis. 1) light source, 2) delta RAM XTM monochromator, 3) sample chamber, 4) monochromator for emission and grating, 5) detector, 6) power sources, 7) result window on PC. The arrow indicates the direction of light originating from the power source to the detector.

3.3.4 UV-Visible (UV-VIS) Spectroscopy

UV-VIS spectroscopy is one of the commonly used techniques to gather the initial details about the optical properties. It is considered one of the best methods to obtain the absorbance or transmission spectra for the molecules present in the solution or the solid form. As the name suggests, UV-VIS spectroscopy utilizes light in the visible and near-infrared ranges, which is responsible for the electronic transitions of the molecules. The basic principle involves measuring the intensity of light before (I_0), and after (I) it passes through the sample (figure 3.10). The ratio of this I/I_0 can be called transmittance with the notation (T). The absorbance (A) can be represented as (equation 3.3)

$$A = -log\left(\frac{\%T}{100\%}\right) \tag{3.3}$$

Apart from measuring the absorbance or transmittance, the equipment can also be customized to measure the reflectance spectrum. The detector measures the intensity of light reflected from the sample (I) and the comparison is done against the light reflected from the reference material (I_0). A ratio of I/I_0 gives information about the reflectance (%R). In general, a reflectance spectrum is registered by collecting the intensity of the light reflected as a function of wavelength (λ, nm).

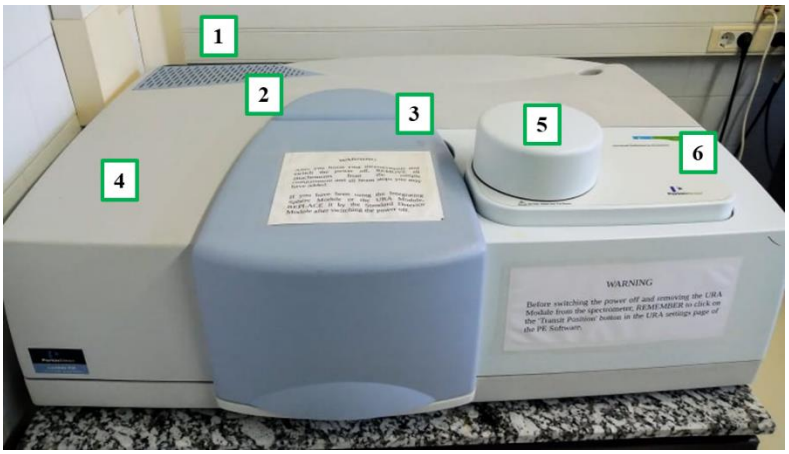

Figure 3.10: Perkin Elmer Lambda 950 model attached with a Universal Reflectance Attachment (URA) along with, 1) light source, 2) optical setup, 3) monochromator, 4) beam splitter, 5) sample stage, 6) detector. The arrow indicates the best possible movement of light from the power source to the detector.

3.3.5 Reflectance spectroscopy (RS)

Reflectance spectroscopy (RS) is one of the point probing technologies that are primarily used to determine the spectral composition of a sample. Basically, it reveals the extent to which the path of the incoming light is altered by a surface of the sample and register it in the form of intensity vs time.

In this thesis, RS has been applied to measure the release of the drug from the porous structures in real-time. To show this, flow cell measurements have been conducted using a USB 2000+ fiber spectrometer (Ocean Optics, Orlando, FL, USA), where the sample is illuminated by a fiber optic bundle (QR200-7-VIS-BX, Ocean Optics, USA) consisting of six illuminating fibers connected to a tungsten halogen light source (HL-2000-HP-FHSA, Ocean Optics, USA). Light from the illuminating bundle is imaged onto the sample surface by a converging lens in a 4-f configuration. The reflected light was collected with the same lens and directed to a reading fiber in the same bundle connected to the spectrometer. Spectra has been recorded from a circular spot having a diameter of 3 mm at 10 s time intervals for the wavelengths between 400 nm and 900 nm employing the spectrasuite software by Ocean Optics (figure 3.11).

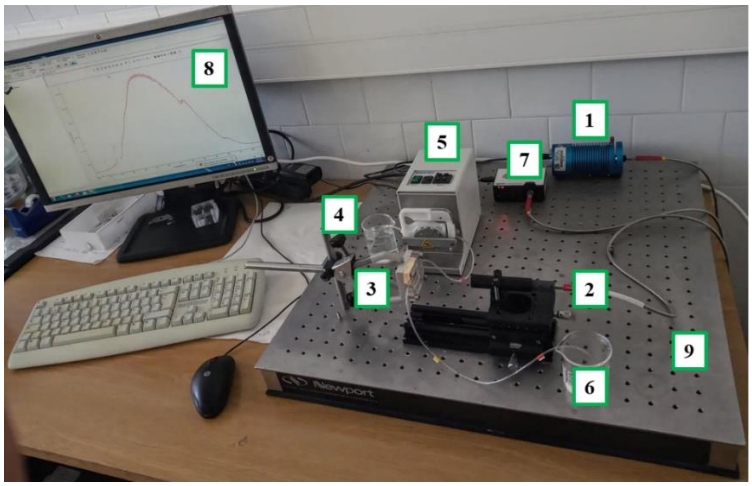

Figure 3.11: RS setup utilized in this thesis for real-time monitoring with the following accessories, 1) Light source, 2) Optical fiber bundle, 3) Sample holder, 4) Inlet, 5) Peristaltic pump, 6) Outlet, 7) Detector, 8) Graphical

analysis on PC, 9) Optical table.

3.4 Numerical simulations

This section presents a general introduction to the numerical methods used to study the properties and the changes inside NAA that occur during the infiltration and the release processes. The numerical simulation of the optical properties of the NAA structures is carried out by the Transfer Matrix Method (TMM) involves the modelling of the propagation and the reflection of light through several interfaces in a multi-layered structure.

3.4.1 Transfer matrix method (TMM)

The Transfer matrix method is one of the simplest and widely used methods to study the optical properties of thin films including reflection, transmission, band diagram calculation, and emission spectra (Zi, Wan, and Zhang 1998)(Zhang et al. 2000)(Squire et al. 2000)(Macleod 2010)(Yeh 2005). This method is intended for thin-film multilayer structures with definite thicknesses and uniform refractive indices, with the layers divided by interfaces at which a discontinuity of the refractive index exists. This permits the application of continuity boundary conditions and to solve the wave equations at each layer as well as at the incident, substrate, and transmitted media. TMM relies on the fact that if an electric field is applied to the multilayer system, then according to the Maxwell equations, it follows a simple continuous boundary condition while travelling from one layer to another. This means that if the electric field is known at the incident medium of the layer, then the electric field at the end of the multilayer can be calculated by matrix calculations.

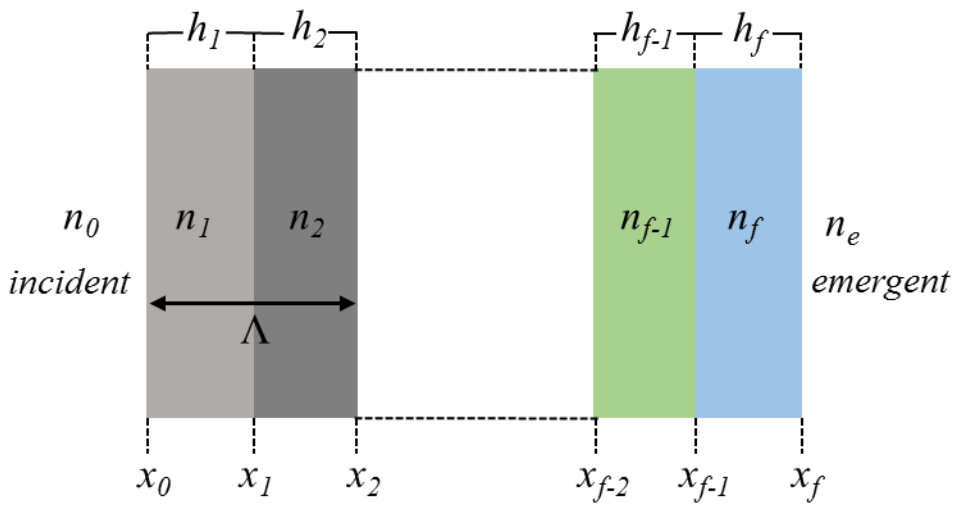

Figure 3.12: Schematic illustration of a multi-layered system consisting of f layers of a material with the height of h, the refractive index of n_1, period of Λ, and a thickness of h_1 respectively.

To obtain the transmission and the reflection process of the electromagnetic radiations penetrating through a multi-layered system using the TMM model, we deployed a one-dimensional structure made up of alternating stacks of nanoporous anodic alumina of varying refractive indices. As explained in figure 3.12. n_0 depicts the incident medium, whereas n_1 and n_2 represent the different refractive index in between the layers x_0-x_1 and x_1-x_2, respectively and ne represents the substrate's refractive index. In addition, h_1 and h_2 demonstrate the thickness of the as numbered layer and Λ can be referred to as the period ($h_1 + h_2$).

The structure can be defined as follows (equation 3.4):

$$n(x) = \begin{cases} n_{0,}\, x < x_0 \\ n_{1,}\, x_0 < x < with\ x_1 = x_0 + h_1 \\ n_{2,}\, x_1 < x < x_2\ with\ x_2 = x_0 + \Lambda = x_1 + h_2 \\ \vdots \\ n_{e,}\ x_f < x\ having\ x_f = x_0 + N\Lambda = x_{f-1} + h_2 \end{cases} \quad (3.4)$$

Also, the electric field distribution can be expressed as (equation 3.5):

$$E = E(x)e^{i(\omega t - \beta x)} \quad (3.5)$$

where the electromagnetic propagation is in the X direction, ω is the wave angular frequency, and ß represents the propagating wave vector. Considering these equations carefully, the distribution of the electric field in the nth layer can be represented in a scenario where the plane wave travels from the right direction and going out from the left. This can equate as follows (equation 3.6):

$$E_n(x) = \left(A_n e^{-i\beta_{nx}(x-x_n)} + B_n e^{i\beta_{nx}(x-x_n)}\right) \quad (3.6)$$

where A_n and B_n denotes the amplitude of the incident and emergent wave respectively at the interface of $x = x_n$, $ß_{nx} = \omega_n n\cos(\theta_n)/c$ shows the x component of the wave vector in which the symbol ω depicts the angular frequency, c is the speed of light, and θ_n is the angle of the ray in the n-th layer.

By applying the matrix notations mentioned above and the boundary continuity conditions at the interfaces, the amplitude of different layers can be related by

$$\begin{pmatrix} A_{n-1} \\ B_{n-1} \end{pmatrix} = D_{n-1}^{-1} D_n \begin{pmatrix} A_n \\ B_n \end{pmatrix} \quad (3.7)$$

where D represents Dynamical matrices which can also be inferred as (equation 3.8):

$$D_n = \begin{cases} \begin{pmatrix} 1 & 1 \\ n_n cos\,(\theta_n) & -n_n \cos(\theta_n) \end{pmatrix} \; for\ TE\ wave \\ \cdots \\ \begin{pmatrix} \cos(\theta_n) & cos\,(\theta_n) \\ n_n & -n_n \end{pmatrix} \; for\ TM\ wave \end{cases} \tag{3.8}$$

The description of the matrix which represents the incoming propagating wave that enters and exit within n-th layer is the propagation matrix given by the following equation 3.9:

$$P_n = \begin{pmatrix} e^{i\beta_{nx}h_n} & 0 \\ 0 & e^{-i\beta_{nx}h_n} \end{pmatrix} \tag{3.9}$$

where Pn represents the propagation matrix, h_n is the thickness of the nth layer. After combining the eq. (3.9) with the eq. (3.7), the equation of the transfer matrix for the nth layer can be derived (3.10):

$$M_n = D_n^{-1} P_n D_m \tag{3.10}$$

After that, for the overall multilayer system, the transfer matrix can be calculated as in equation 3.11:

$$M = \prod_{n=1}^{f} M_n = \begin{bmatrix} M_{11} & M_{12} \\ M_{21} & M_{22} \end{bmatrix} \tag{3.11}$$

The matrix mentioned in the above equation (3.11) allows to correlate the amplitude of the electric field at the incident to the emergent medium through the following expression in equation 3.12:

$$\begin{bmatrix} A_0 \\ B_0 \end{bmatrix} = \begin{bmatrix} M_{11} & M_{12} \\ M_{21} & M_{22} \end{bmatrix} \begin{bmatrix} A_e \\ B_e \end{bmatrix} \tag{3.12}$$

3.4.2 TMM applied for NAA-GIFs

In this thesis, the calculated reflectance spectra of NAA-GIF structures filled or covered with the drug molecule have been obtained with the TMM (S.

Bosch, Ferré-Borrull, and Sancho-Parramon 2001). However, in NAA-GIFs the effective refractive index with the depth of the pore shows a continuous modulation. To apply the TMM to the NAA-GIF structures, it is necessary to discretize such continuous variation of the refractive index into a finite number of uniform layers that approximate the variation of the refractive index.

In the simulations, a stacked NAA-GIFs (Acosta et al. 2019) composed of two structures obtained with two different time periods (T_{top} and T_{bottom}) representing one GIF stacked on top of another one has been considered. The GIFs are obtained by applying an anodization current consisting of a constant current density term plus a sinusoidal time-varying term (refer to chapter 4, equation 4.1). This applied sinusoidal anodization creates straight pores through the aluminium oxide matrix with a modulation of the pore diameter. In a first approximation, this modulation of the pore diameter can also be considered as sinusoidal, with two different length periods corresponding to the two different time periods, one for the top GIF (Λ_{top}) and one for the bottom GIF (Λ_{bottom}). This continuous variation of the pore radius results in a continuous variation of the volume fractions of aluminium oxide and pore contents as a function of the depth, which leads to the continuous variation of the refractive index with the depth into the NAA-GIF structure. In the simulations, each GIF filter consists of 100 periods, being the period length of the top GIF Λ_{top} = 164 nm and the period length of the bottom GIF Λ_{bottom} = 284 nm. Each period in the GIF is discretized into 8 layers. For each of such layers, a value of pore radius is obtained. This pore radius is then used to calculate a value of volume fraction of each of the material constituents at a given depth of the pore: Al_2O_3 host matrix, drug molecule attached to the inner pore surface and medium filling the pores. The average volume fraction for the aluminium host for both GIF structures has been considered as f (Al_2O_3) = 0.9, according to the fact that the average anodization current density is the

same for both GIF structures. This volume fraction is usually related to the average porosity in the material.

On the other hand, the sinusoidal variation of the pore radius produces a sinusoidal variation of the aluminium host volume fraction. The amplitude of this sinusoidal variation of the volume fraction has been taken as f (ampl) = 0.025. The amount of the drug molecule into the pores is modelled by assuming a constant volume fraction with the depth as the drug molecule forms a conformal layer on the pore surface. Different spectra were obtained for drug molecule volume fractions varying between f (dye) = 0.001 and f (dye) = 0.075. The remaining volume of the pore and the incident medium is considered to be water (the release medium), with a refractive index of 1.33. From the variation in depth of the volume fractions of the constituent materials of the NAA-GIF, the variation in depth of the refractive index is obtained applying the Bruggeman effective medium theory (Salvador Bosch et al. 2000) to the mixture of the material constituents (aluminium oxide matrix, release medium, and drug).

The NAA-GIFs model is completed by including a uniform aluminium oxide layer of about 40 nm thickness at the bottom of the GIF to take into account the barrier layer present in the structure as a consequence of its very preparation process. No substrate is considered for the model of the NAA-GIFs structure. The samples are prepared by anodization on aluminium foil substrates. However, the presence of the aluminium substrate provides a high reflectance of the sample in the whole spectral range that reduces the visibility in the spectrum of the high reflectance bands produced by the nanostructuring of the GIF. For this reason, the aluminium substrate is removed from the NAA-GIF structures for flow cell measurement.

The refractive index of aluminium oxide has been taken from the book from Palik (Palik 2012). The goal of the numerical study is to determine the impact on the optical properties of NAA-GIFs while it is being infiltrated with the drug, the refractive index of the drug has not been taken from a particular molecule, but it has been modelled theoretically with the Lorentz Oscillators model (S. Bosch, Ferré-Borrull, and Sancho-Parramon 2001) for the refractive index (n) and extinction coefficient (k). The parameters of the Lorentz Oscillator model have been chosen to obtain a drug molecule with maximum absorption at the same wavelength range as one of the high reflectance bands of the NAA-GIFs.

In figure 3.13, the extinction coefficient shows maximum absorption at 530 nm with a full width at half-maximum of 150 nm, and a maximum extinction coefficient of 0.2. These optical absorption properties are compatible with several drugs or dyes that could be infiltrated and immobilized into the pores. The periods of the GIF composing the NAA-GIF have been chosen so that one of the high reflectance bands lies in the range of the high absorption of the drug while the other high reflection band lies far from this high absorption range.

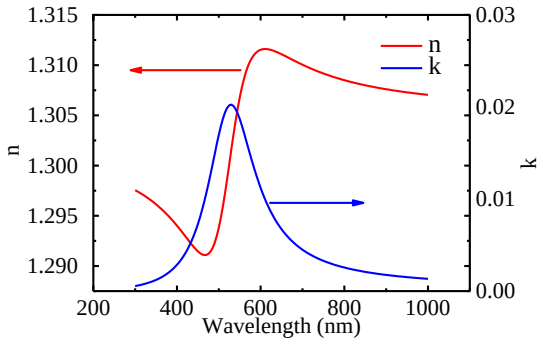

Figure 3.13: The refractive index (n) and extinction coefficient (k) for the drug

modelled by Lorentz Oscillators model and used in the numerical simulations.

To simulate the effect of the drug molecule filling the pores, NAA-GIF were simulated with four different volume fractions f (drug) = 0 (pores only filled with water), and f (drug) = 0.025, 0.050 and 0.075. Figure 3.14 a) show the calculated spectra obtained for increasing drug volume fractions. The arrows show that the maximum reflectance of the signal band decreases at a faster rate as compared to the reference band as the number of molecules within the pores increases. However, the rate of decrease of the signal band corresponding to the drug absorption region is bigger. These two observations can be explained by the increasing amount of drug molecules into the pores, which leads to propose the ratio analysis between the heights of these two maximum reflectance values as a measure for the amount of drug molecules present inside the pores.

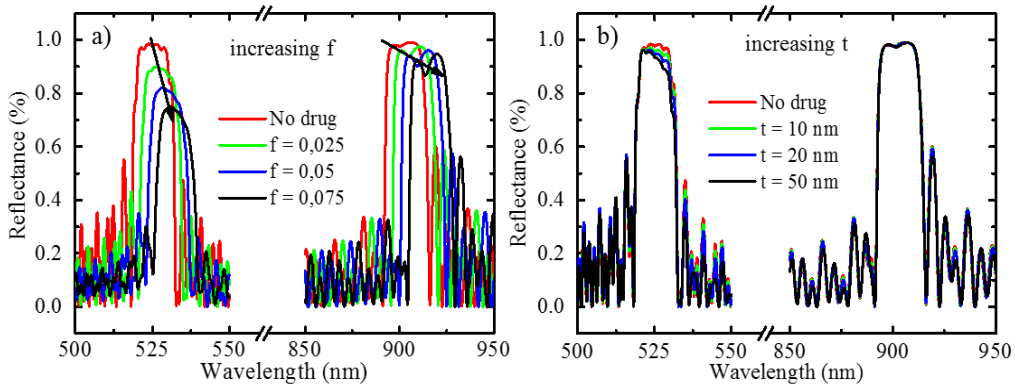

Figure 3.14: (a) Reflectance spectra obtained by numerical simulation considering different volume fractions (f) of a drug molecule filling the NAA-GIF pores, (b) calculated reflectance spectra for different thickness (t) of a

drug molecule layer on the NAA-GIF surface.

To evaluate whether the formation of a drug layer on the top surface of the NAA-GIFs influences the optical properties of the structure, such formations were also simulated by considering an additional continuous layer of drug with different thicknesses, t = 10 nm, 20 nm and 50 nm. Figure 3.14 b) shows the calculated reflectance spectra for the case where the drug molecules form a uniform layer on the top of NAA-GIFs surface. It can be observed that such a thin film on the top of the NAA-GIFs structure has a minor influence on the reflectance, causing only a slight decrease in the maximum reflectance of the signal band. This result can be explained by the fact that even a relatively thick layer of the drug on the top of the NAA-GIF represents a small amount as compared with the drug that can be filling the pores, even at volume fractions as small as f (drug) = 0.05.

3.5 Final remarks

This chapter demonstrates all the laboratory tools and software used to fabricate different types of NAA architectures with a detailed explanation. In brief, it gives a complete overview right from the pre-treatment of aluminium till the post-processing of NAA to obtain the NAA structure with the different chemicals involved. In addition, different types of NAA structures have been listed in a separate sub-section along with detailed protocols for easy reproducibility. It has been shown that the varying anodization processes clearly have an impact on NAA morphology. Also, different characterization techniques have been elaborated to gather details about NAA during the modification processes along with the basic principle. Finally, we give an overview of the numerical simulations applied to obtain the details about the filling of the drug molecules inside the porous material with the TMM method.

Chapter 4

Drug loading and release analysis based on Nanoporous Anodic Alumina Gradient Index Filters

4.1 Introduction

As discussed in chapter 3, a controlled sinusoidal anodization process results in a periodic variation of NAA, enabling one to obtain a photonic structure consisting of photonic stopbands placed within the desired region. Therefore, in this chapter, we plan to prepare an NAA-GIFs structure with two photonic stopbands (PSBs), where one of its stopbands falls in the same absorption region of the drug denoted as the 'signal band', whereas the second stopband is away from this absorption range which is termed as 'reference band'. The numerical simulations presented in chapter 3 confirm that the relative height of the photonic stopbands in the reflectance spectra of NAA-GIFs filled with the drug can be related to the relative amount of drug filling the pores. This chapter utilized a method named "Drop casting" (described in chapter 2) to fill the pores, followed by the measurements with the optical methods. For the ease of simplicity to the readers, the model drug i.e. Rh6G has also been denoted as "drug".

On the other hand, in sustained drug delivery approaches, the burst release of the target molecule has always been a significant challenge; therefore, different stimuli are used nowadays to hold the drug molecules and release them only when triggered by any specific stimulus. In this regard, pH-sensitive mechanisms draw massive attention as they are similar to the pH variations inside the human body. The best example of this can be seen in the gastrointestinal tract, where the pH remains acidic (pH-2.0) and changes to basic (pH-5–8) in the intestine. Also, the pH of the normal blood is 7.4 as compared to unhealthy or wound-affected areas, where it ranges from pH 5.0–7.4 (Schmaljohann 2006). Henceforth, polyelectrolyte multilayers (PEM) have been often used to coat the surface of nanoporous structures for the

sustained delivery of drug molecules (Porta-i-Batalla et al. 2016)(Deshmukh et al. 2013).

One of the most challenging problems, when PEM is used in NAA nanostructures is the determination of the degree of drug loading into the pores and the rate of release of the drug-loaded into the nanostructure. In this chapter, the optical properties of NAA-GIFs are exploited to evaluate such magnitudes. To this end, the effective medium of NAA-GIFs has been engineered in a sinusoidal fashion to obtain the PSBs in the visible spectrum. After that, the pore widening was performed to widen the pores of NAA-GIFs followed by the drop/dry loading with the cargo molecule and analysis of the change in relative height of reflectance bands with the UV-Visible spectroscopy. Once the changes between both the PSBs were correlated and verified, this method was applied to demonstrate the pH responsiveness aspect of NAA-GIFs. To demonstrate this, the samples were modified with the polyelectrolyte multilayers and the same cargo molecule where NAA-GIFs were used as reservoirs, PSS/PAH coating was employed as a pH-responsive coating. The presence of polyelectrolyte multilayers helps to prevent the early release of the dye molecules hence providing control capabilities to investigate the nature of release from NAA-GIFs. The methodology developed in this chapter acts as a tool for studying drug delivery from porous nanostructures.

4.2 Fabrication of NAA-GIFs

To evaluate the possibilities of using the stopband reflectance ratio as a measure of the released drug from porous anodic alumina, NAA-GIF samples with different lengths were prepared through a one-step electrochemical anodization process by applying a sinusoidal anodization profile described in here (Acosta et al. 2019). In brief, the aluminium substrates were treated with acetone, ethanol, and water in sequence to remove all organic impurities

present on the surface. Pre-treated aluminium foils were electropolished in a mixture of 4:1 v/v of ethanol: perchloric acid at 20 V for 5 min, alternating the stirring direction every minute. Electropolished aluminium substrates were then anodized in an electrochemical cell containing 0.3 M oxalic acid at 5 °C under controlled stirring.

All the samples were fabricated by applying a current density anodization profile through Keithley 2400 source meter, with constant monitoring utilizing a custom-built LabVIEW® program based on the following (Acosta et al. 2019) equation (4.1):

$$j(t) = \begin{cases} j_{\text{average}} + j_{\text{amplitude}} \cdot \sin\left(\frac{2\pi}{T_1} t\right) \text{ for } 0 < t < N \cdot T_1 \\ j_{\text{average}} + j_{\text{amplitude}} \cdot \sin\left(\frac{2\pi}{T_2} t\right) \text{ for } 0 < t - N \cdot T_1 < N \cdot T_2 \end{cases} \quad (4.1)$$

where $j(t)$ is the applied current density at the time (t), j_{average} corresponds to the average current density, $j_{\text{amplitude}}$ is the amplitude of the sinusoidal variations of such magnitude. Two different time periods of the sinusoidal time-varying term (T_1 and T_2) are used, the first for a time $t_{top} = N \cdot T_1$ while the second for a time $t_{bottom} = N \cdot T_2$, this is for N cycles for each time period (Figure 4.1). The constant current density and amplitude of the sinusoidal term are the same for the two phases of the anodization. The samples prepared in this study were obtained with j_{average} = 2.6 mA/cm^2, $j_{\text{amplitude}}$ = 1.3 mA/cm^2, T_1 = 152 s and T_2 = 210 s. Three different sets of samples were prepared with N = 150, N = 200 and N = 250.

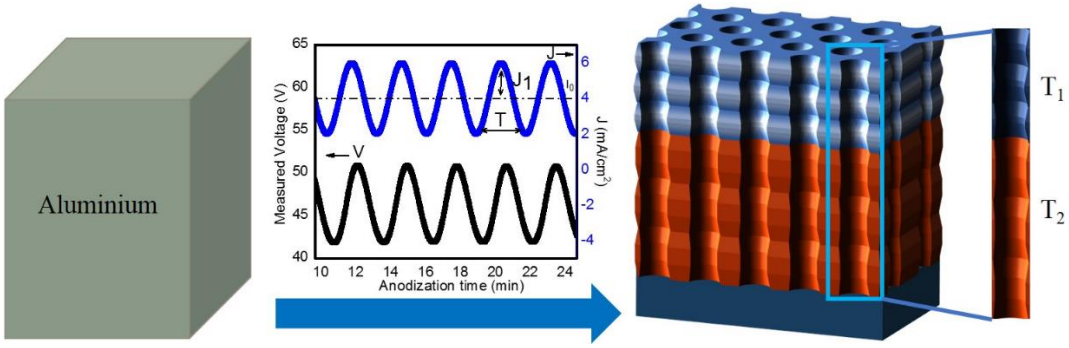

Figure 4.1: Schematic representation of the electrochemical strategy applied to produce nanoporous anodic alumina gradient-index filters (NAA-GIFs) through sinusoidal anodization. J_1 represents current density amplitude, I_0 represents offset current density, V and J correspond to measured voltage and applied current density, respectively, T is the time period of the sinusoidal variation. T_1 and T_2 represent the time periods used to obtain the two rugate structures that together form the NAA-GIFs in this study.

The aluminium layer at the bottom prevents reflectance bands with high contrast. For this reason, it was removed by chemical etching in a mixture of HCl (100 mL in 400 mL H_2O) and $CuCl_2$ (13.6 g added to the HCl/H_2O mixture). A pore-widening treatment was also performed for all the samples by wet chemical etching in 5 wt% H_3PO_4 at 35 °C for 15 min (Acosta et al. 2019). This treatment widened the average diameter of the pores from 30 nm of the as-produced samples to 45 nm.

4.2.1 Anodization profiles obtained for NAA-GIFs

Sinusoidal anodization profile aims to reshape the pore geometry in NAA-GIFs through continuous modulation of pore diameter in depth. Figure 4.2 a) represents the applied anodization current density and measured anodization voltage graphs as a function of time for different samples prepared by applying different numbers of periods, i.e., N = 150, 200, and 250. Figure 4.2 b) shows

the same magnitude for the sample with N = 150 between the time instants t = 18,000 s-29,000 s. Finally Figure 4.2 c) represents the magnified magnitude for the sample with N = 200 between the time instants t = 22,000 s-24,000 s.

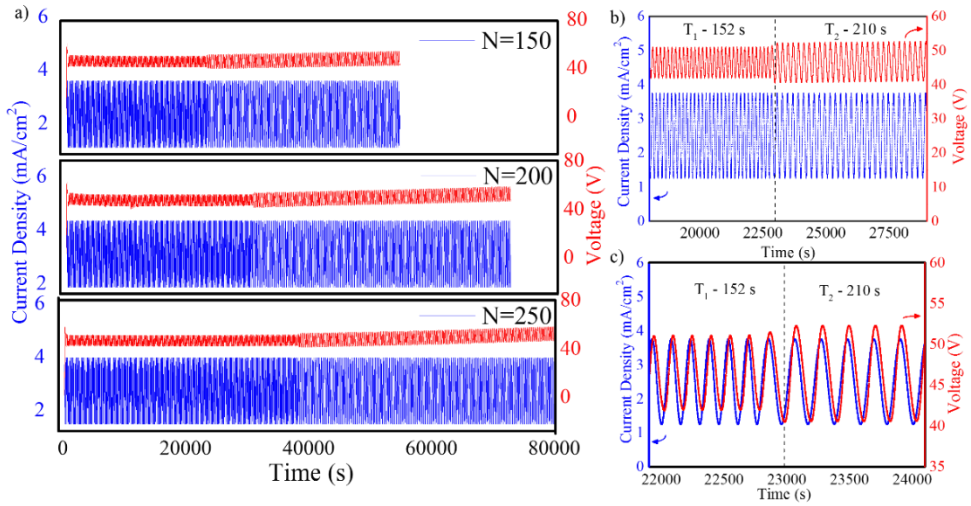

Figure 4.2: Complete sinusoidal anodization profile applied to obtain NAA-GIFs with parameters $j_{average}$ = 2.6 mA/cm^2, $j_{amplitude}$ = 1.3 mA/cm^2; T_1 = 152 s, T_2 = 210 s. (a) Applied sinusoidal current and resulting measured anodization potential for the different applied number of periods, indicated in the graphs; (b, and c) Detailed view of the data for N = 150 for the time instants between t = 18,000 s-29,000 s and 22,000.

Figure 4.2 a) depicts the evolution of the sinusoidal profile for all the three sample sets prepared in this study. As there are a large number of cycles, the current variation can hardly be distinguished while switching from T_1 to T_2 only a visual change in the curve can be observed. Figures 4.2 (b, c) show a detail of the applied current and measured voltage where the sinusoidal variation of both magnitudes is demonstrated. This figure shows how the sudden change in the period of the applied sinusoidal current produces a discontinuity in the amplitude of the measured voltage. The graph for the

measured anodization voltage shows a clear difference between the two-time intervals where the periods T_1 or T_2 are applied: the value obtained for the measured voltage when a current of period T_1 is applied is between 41–50 V with an average of 45 V, while when a period T_2 is applied, the value varies between 40–52 V with an average of 46 V. Furthermore, after the change of period from T_1 to T_2, the average value of the measured voltage increases at a rate of 0.02 V/s. This increased rate in the voltage per second was observed for all the different applied number periods. Figure 4.2 c) also shows that the measured voltage shows a delay with respect to applied current density for both time periods. This delay is found to be 48 s.

The results mentioned above confirmed that by applying a controlled sinusoidal anodization current, the electrochemical system responds with a sinusoidal measured anodization voltage of the same period. As the voltage is mainly applied across the barrier layer at the bottom of the pores and its value directly relates to the thickness of the barrier layer, the varying voltage results in a modulation of the pore diameter. The voltage delay with respect to the current is explained by the fact that the thickness of the barrier layer increases when voltage increases and decreases when the voltage decreases, but this response needs some time, as the barrier layer needs this time to adjust its thickness. The change in voltage amplitude can be explained by the fact that for a longer period T, the barrier layer has more time available to adjust its thickness and thus, it can reach a bigger amplitude in thickness, which is translated into a bigger amplitude in the measured voltage (Losic and Lillo 2009) (Montero-Moreno et al. 2009).

4.3 Scanning Electron Microscopy (SEM)

Figure 4.3 represents the structural characteristics obtained through Scanning Electron Microscopy (SEM) of NAA-GIFs. Figure 4.3 a) shows a top-view SEM

picture of a sample corresponding to N = 200, Figure 4.3 b) shows an image of the cross-section parallel to the pores of the same sample, while Figure 4.3 c) shows a magnified view of the cross-section in b). The cross-section was obtained by breaking the as-produced sample pressing its border with the tip of a tweezer. These images demonstrated the engineered effective medium of NAA-GIFs resulting from voltage change in a sinusoidal fashion. The top view reveals the random distribution of nanopores with the average pore diameter (d_p) of 45 ± 4 nm and an average inter-pore distance of 116 ± 12 nm (Figure 4.3 a). The cross-sectional SEM picture of the NAA-GIF reveals a total thickness of approximately 37 µm, corresponding to an anodization time of N = 200 periods with time periods T_1 = 152 s and T_2 = 210 s (figure 4.3b). Inset shows the magnified version with the arrows depicting the modulated structure due to sinusoidal pulses (figure 4.3 c), allowing the desired molecules to move freely within the nanoporous structure.

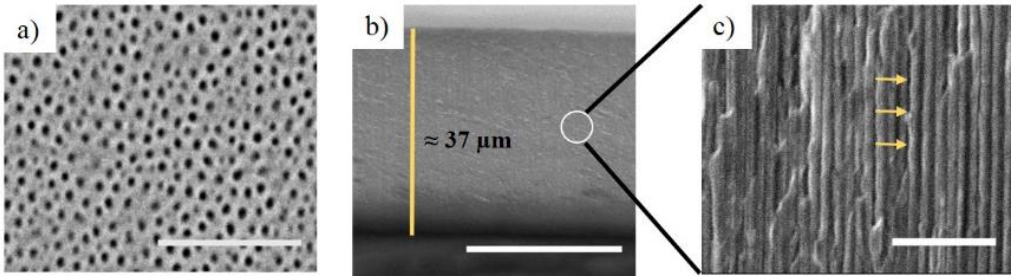

Figure 4.3: SEM pictures of as-produced (without any modification) NAA-GIFs for samples with N = 200; (a) Top view (Scale bar = 1 µm); (b) cross section (Scale bar = 25 µm); (c) Magnified view of figure (b) showing the modulations in the structure (Scale bar = 1 µm).

4.4 Rhodamine 6G (Rh6G) loading

For this study, Rh6G was used as a cargo molecule due to its high fluorescence properties and wide use in diagnostic applications. The loading procedure

inside the NAA-GIFs was accomplished by two different methods: drop/dry and layer by layer deposition methods (LBL).

In the first method, also denoted as the drop/dry method, the relative height of the photonic stopbands was tested and verified along with the simulations by only using Rh6G dye inside NAA-GIFs. To achieve this, a 10 µL drop of the cargo molecule (1 mg/mL) in water was dropped onto the surface of NAA-GIFs and dried at room temperature. In total, 6 drop/dry cycles were performed, followed by measurement with UV-Visible spectroscopy after each cycle (Figure 4.4). This method does not involve the incorporation of polyelectrolytes or other modifications inside the NAA-GIFs.

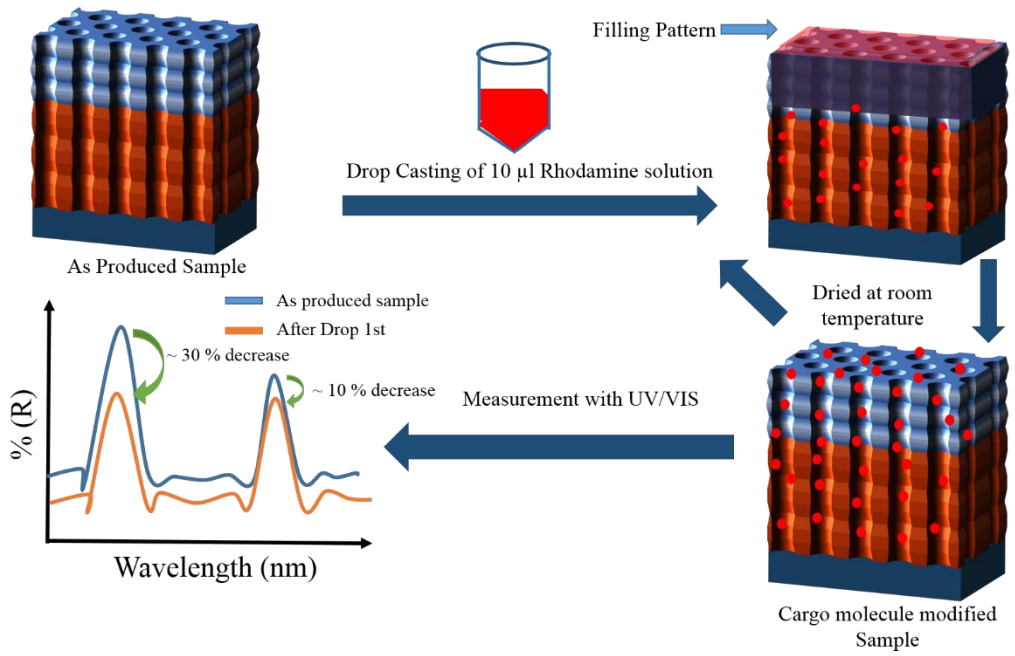

Figure 4.4: Illustration of drop/dry method performed by drop-casting (10 µL) of Rh6G on the surface of NAA-GIFs followed by the drying procedure in the air and measurement with UV-VIS Spectroscopy. This procedure was

repeated for 6 drop/dry cycles for the optical characterization of NAA-GIF.

4.4.1 Ultraviolet-Visible Spectroscopy analysis (UV-VIS)

The photonic nanostructures prepared in this study were designed to display two stopbands where one of the bands falls within the broad absorption wavelength range of Rh6G dye serving as a "Signal band" while the other stopband is far away from this region, acting as a "Reference band". To confirm the as-prepared samples show the bands at the desired wavelengths after the pore-widening process, UV-Visible spectra of NAA-GIF were recorded and measured. Figure 4.5 shows the obtained spectrum from UV-VIS showing the two expected signal and reference bands for all the time periods in the desired wavelength ranges. In this study for all the samples, the produced reflectance spectra were not recorded, but it can be assumed from the analysis from our group's previous research that one can expect a blue shift of around 25–30 nm with the 15 min pore-widening process using 5 wt% H_3PO_4 at 35 °C (Acosta et al. 2019).

Figure 4.5 a) shows the reflectance spectrum for the sample fabricated with N = 150, the signal band was positioned at 474 nm. The average reflectance estimated from three different samples is 50.1% and at 678 nm for the reference band with an average reflectance of 38.9%. Similarly, for the sample with N = 200 (figure 4.5 b), the signal and the reference band were found at 478 and 724 nm with an average reflectance value of 60.1% and 43.2%, respectively. In addition, a side lobe was also observed in this sample, which might occur due to a sharp truncation of the refractive index at the boundaries of the NAA-GIFs (Ilyas et al. 2007). Figure 4.5c) shows the results for samples fabricated with N = 250 where the positions obtained for the signal band were at 472 nm with an average reflectance of 50.6% and 698 nm having an average reflectance of 38.6% for the reference band (Figures 4.5 a–c.) With these

results, we achieved and confirmed one of the bands within the absorption region of the Rh6G dye molecule while the other band was obtained far from this region.

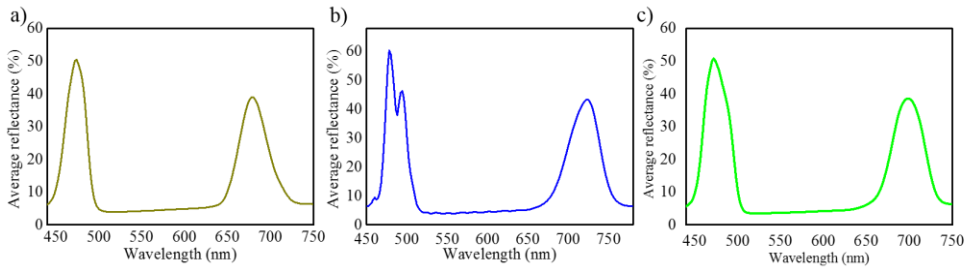

Figure 4.5: UV-Visible Spectra of NAA-GIFs with varying number of periods, i.e., (a) N = 150, (b) N = 200, (c) N = 250.

In order to confirm the results of the simulations described in chapter 3, drop/dry experiments were conducted using Rh6G as a cargo molecule due to its excellent fluorescence properties. The results showed similar behaviour as observed in the simulation. Figure 4.6 (a, and b) show the UV-Visible spectra obtained after each drop/dry cycle and the evolution of the ratio of the two reflectance maxima with the number of drop/dry cycles. Figure 4.6 a) demonstrates that the addition of the first drop of the dye leads to a drastic change in the effective medium of the NAA-GIFs and the reflectance reduces from about 55% down to approximately 25%. The trend continues to follow as drop/dry cycles are applied. In total, the overall reflectivity was reduced from 54% to 3.5% after the 6th drop addition. Figure 4.6 b) shows the ratio between the relative heights of the signal to the reference band showing a decreasing trend indicating the successful filling process of the NAA-GIF structure with the dye molecules. This trend indicates that the filling of the pores is not uniform: as the number of drop/dry cycles is increased, the amount of cargo molecules that can be infiltrated in the pores is exponentially reduced.

This can be explained by the fact that the increasing concentration inside the pores makes more difficult the infiltration of further substances.

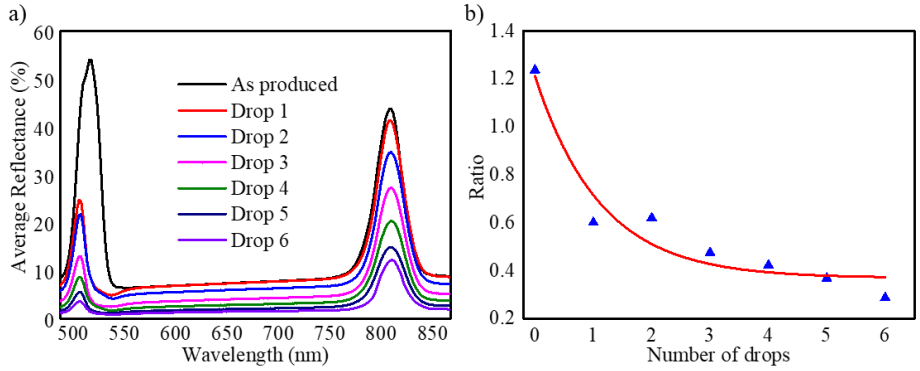

Figure 4.6: (a) UV/VIS reflectance spectra for NAA-GIFs with N = 200 periods measured after each cycle of the drop/dry experiment; b) points: ratio of the maximum reflectance of the signal band to the maximum reflectance of the reference band, as obtained from the spectra in a) as a function of the number of drop/dry cycles. The line is a non-linear fit to illustrate the trend.

The above analysis confirms that the simulation results (performed in chapter 3) are in good agreement with the experimental results and prove that the drop/dry method is useful to infiltrate the NAA-GIFs effectively and to demonstrate a way of analyzing the successful filling of pores. Furthermore, the relative height of the signal band with respect to the reference band can be used to measure the relative amount of absorbing species (dye or drug) within the nanopores.

4.5 Polyelectrolyte multilayers and Rh6G loading

In a separate set of experiments, keeping in mind the swelling/contraction nature of PSS/PAH polyelectrolytes at acidic and alkaline pH, respectively, NAA-GIFs after the APTES and polyelectrolyte functionalization were first placed in an acidic solution of Rh6G dye in water (100 µg/mL) having pH of

2.4 with a mild stirring overnight for the incorporation of dye molecules. Afterwards, the pH was changed to 8.4, and samples were stirred for another 3 h, causing molecules to be trapped inside the multilayers. After successful deposition, the samples were thoroughly washed with deionized water to remove unwanted molecules from the surface (figure 4.7).

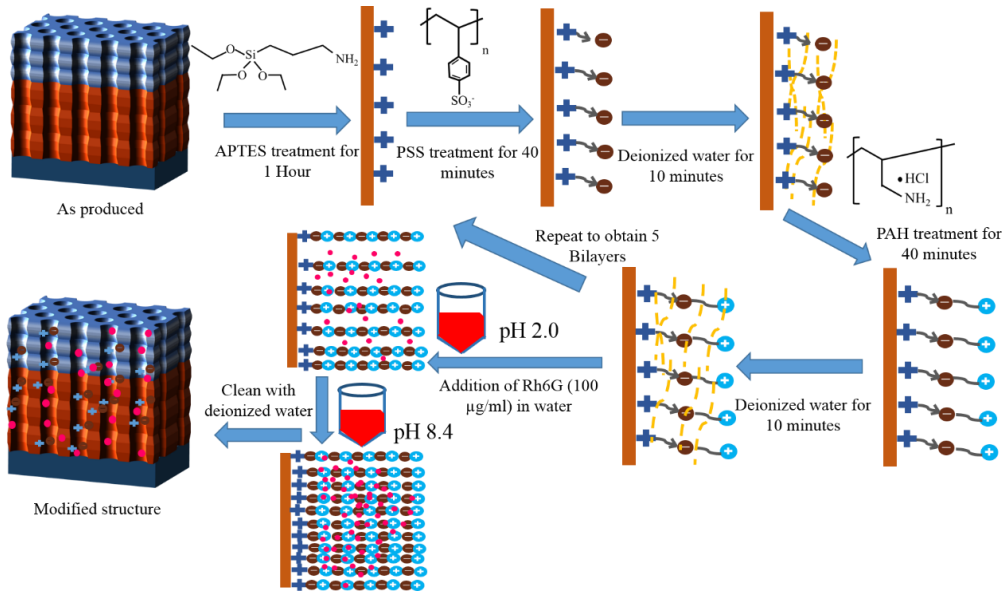

Figure 4.7: Schematic illustration of polyelectrolyte layer by layer deposition and drug loading.

4.5.1 Fourier-transform infrared spectroscopy (FT-IR)

Figure 4.8 represents FT-IR spectra of (a) as-produced, (b) after incorporation with 5 Bilayers (PSS/PAH) and (c) after Rh6G dye infiltration inside NAA-GIFs. Curve (a), corresponding to as-produced NAA-GIFs, shows a weak absorption band at 3420 cm^{-1} due to the −OH stretching. Upon modification with multilayers of PSS/PAH, curve (b), bands appear at 1123 and 1170 cm^{-1} representing SO^{3-} stretching vibrations. Another influential band can be observed at 2927 cm^{-1} indicating typical alkyl CH_2 symmetric stretch due to incorporation of PSS along with PAH. In addition, a strong and broad band

appears at 3420 cm^{-1} indicating the O-H stretching vibration. Due to the presence of characteristic aromatic ring in the structure, Rh6G shows a broad band between 1400-1530 cm^{-1} and at around 1600 cm^{-1} due to the presence of carbonyl group (curve c). Apart from this, another significant C-H stretching band can be observed at around 2970 cm^{-1}. Once the dye was deposited inside the polyelectrolyte layers, the bands representing it are difficult to interpret.

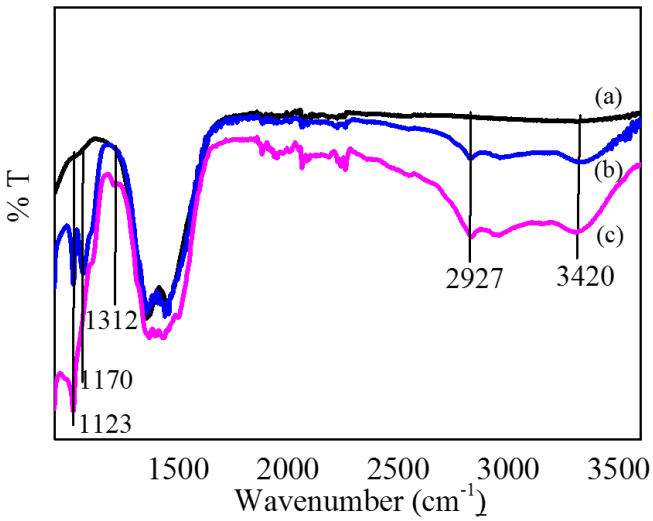

Figure 4.8: FT-IR analysis of NAA-GIFs after each deposition. (a) as produced, (b) PSS/PAH coated (5 Bilayers), c) after Rh6G modification.

4.5.2 Ultraviolet-Visible Spectroscopy

Figure 4.9 represents the UV-VIS spectra recorded after the modification step of NAA-GIFs with polyelectrolytes and Rh6G dye. In all the samples, a drastic change is observed after the modifications with polyelectrolytes and dye molecules, the values of which are shown in table 4.1.

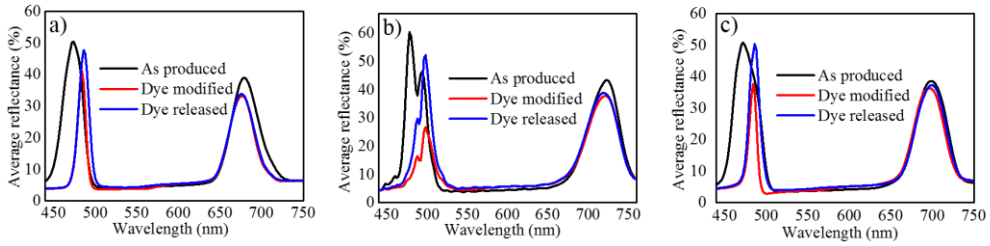

Figure 4.9: UV-Visible spectrum of modified NAA-GIFs with different number of periods i.e. a) N = 150, b) N = 200, c) N = 250.

In addition, table 4.1 shows the maximum average reflectance values recorded with the UV-Visible spectra during the loading process of NAA-GIFs for the samples N=150, 200, and 250.

Table 4.1: Maximum average reflectance for the signal band after each modification step

Time periods	**As produced (%)**	**Dye modified (%)**	**Dye released (%)**
N=150	50.44	41.02	47.70
N=200	60.34	26.76	52.21
N=250	50.82	37.59	50.28

4.6 Dye Release Monitoring Using RS

After loading the samples carefully with the polyelectrolyte multilayers and the drug, the release was monitored from NAA-GIFs under dynamic flow conditions in a custom-built flow cell. The influence of different pore lengths on the releasing behaviour of dye molecules from the pores has been studied. Figures 4.10 (a–c) shows the intensity spectra measured by the fiber spectrometer (described on the experimental part) at different times of the flow cell release experiments, for samples with N = 150, N = 200 and N = 250 (Refer to figure 4.11 for the whole release profile). Figures 4.10 (d–f)

represents the wavelength range corresponding to the signal stopband of the same three samples in figure 4.10 (a–c). The first curves in the graphs (black) represent the intensity spectra of the three samples (N = 150, 200, and 250) as they are placed inside the flow cell before wetting. During this state, the intensity spectra show the two high reflectance bands as relative intensity maxima. At a given instant, the PBS solution with pH 7.4 is flowed to fill the cell and to wet the pores. The moment at which the signal stabilizes is taken as the reference time, t = 0. The wetting process induces a redshift on the maximum wavelength of the Signal and the Reference bands, as well as a reduction in the maximum value of such intensity (Table 1). The spectra taken at instants *t* = 60 minutes and *t* = 120 minutes do not show a noticeable variation with respect to the one measured at *t* = 0. This corresponds to the phase in which the pH 7.4 solution flows into the cell. The successive spectra for t > 120 minutes show a gradual increase in intensity at the wavelength range of the signal band, while the intensity at the wavelength range of the reference band remains practically unchanged. This time range corresponds with the period in which the solution at pH 5.0 has flowed.

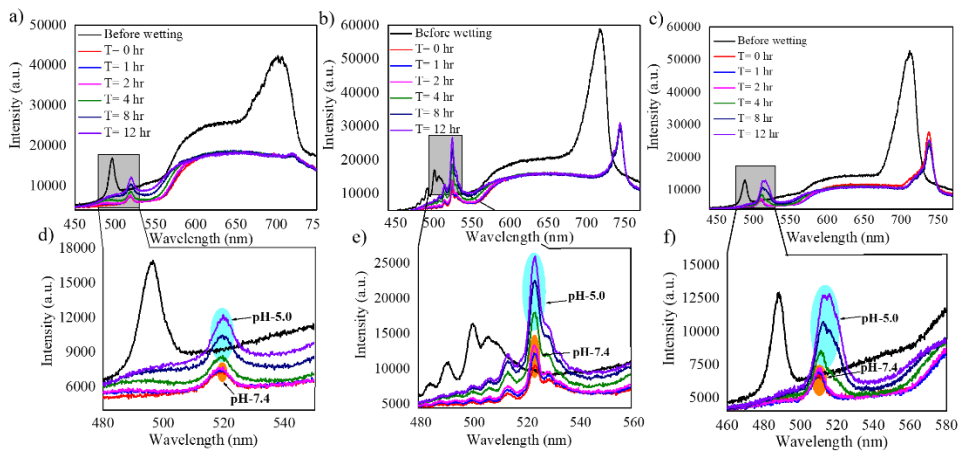

Figure 4.10: Intensity spectra obtained in the flow cell setup and under two pH conditions (5.0 and 7.4) for NAA-GIFs fabricated with a varying number of

periods. (a) N = 150, (b) N = 200, (c) N = 250. (d–f) represent the magnified view of the signal stopband for the data in (a–c), respectively.

Figure 4.11 represents the raw data (intensity vs time) registered in real-time at a time interval of 10 s while the different pH solutions are being passed through the sample.

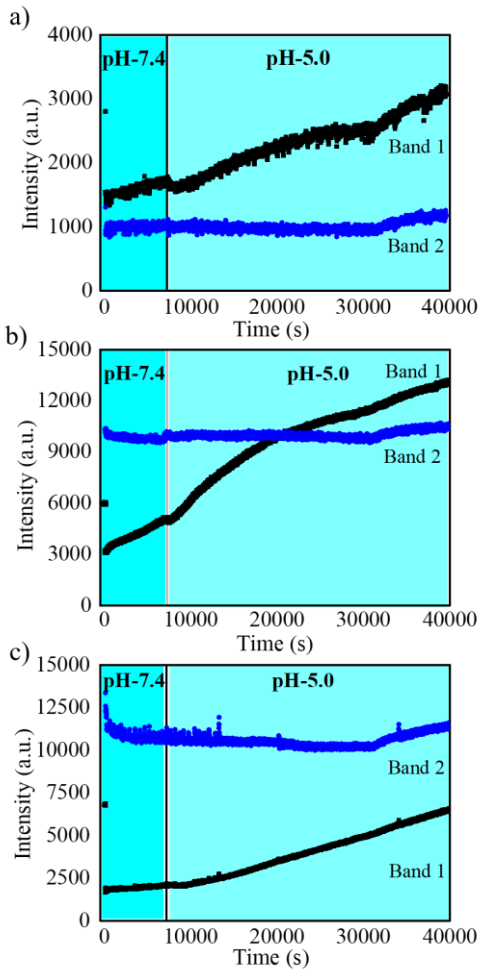

Figure 4.11: Maximum intensity of the signal band and the reference band as a function of time. The maximum intensities are obtained in real-time from measured intensity spectra of NAA-GIFs in the flow cell and as the drug is

released. a) N=150, b) N=200, c) N=250. In this study, the release dynamics obtained can be interpreted in three different phases: (a) the wetting; (b) the stabilization, (c) the release phase.

The wetting process refers to a process that leads to the liquid filling of the pores without any release process, which is possible because of the use of pH 7.4 solution. In the stabilization phase, the solution was introduced for enough time to stabilize the signal, and since the solution has a different refractive index than air, it leads to an abrupt change in the effective refractive index of NAA-GIFs resulting in a redshift for both stopbands followed by a sharp decrease in the maximum signal. This allows the signal to stabilize over time without producing any release. A small increase in signal for the sample with N = 200 is observed during such phase. This can be caused by the cleaning of loosely bound cargo molecules within the structure.

One of the important aspects of utilizing PSS/PAH multilayers in this study is their pH responsiveness. Herein, when pH is changed closely to the pKa value of the cargo molecule, the protonation/deprotonation process of polyelectrolytes takes place, which leads to swelling either by generation or reduction of the charges present in the multilayers (Delcea, Möhwald, and Skirtach 2011) (Koehler, Steitz, and Von Klitzing 2014) (Alba et al. 2014) (Porta-i-Batalla et al. 2016). Figure 4.7 demonstrates the maximum effect of this under acidic conditions where the final phase takes place, i.e., the release phase. This phase starts by flowing the solution of pH 5.0, due to which the protonation of amine groups present in PAH chain takes place, resulting in an increase in osmotic pressure allowing the cargo molecule molecules to diffuse out through the polyelectrolyte chains.

Table 4.2 enumerates the redshift recorded with the software at an interval of 10 s for the signal band before and after the wetting process during the flow

cell procedure for N = 150, 200, and 250. In all the cases, a redshift of 21-23 nm was observed.

Table 4.2: Redshift obtained for the signal band before and after the wetting process for samples with a different number of periods N

Samples	**Wavelength (nm) Before Wetting**	**Wavelength (nm) After Wetting**	**Red Shift (nm)**
N = 150	496	518	22
N = 200	500	523	23
N = 250	488	509	21

In order to show the capability of the spectroscopic measurement in the flow cell to evaluate the rate of release, the intensity spectra were registered every 10 s and analyzed. Figure 4.12 shows the ratio between the maximum of the signal band intensity to the maximum of the reference band of the registered spectra as a function of time. Each of the graphs a), b), and (c) correspond to samples with N = 150, N = 200 and N = 250, respectively. The three curves show an increasing trend after the introduction of the pH 5.0 solution. For the curve corresponding to N = 150, the increasing trend stops at approximately 7.7 h. Instead, for N = 200, it can be observed that the trend reduces its increase rate with time but without reaching a stabilization. Finally, for N = 250 the curve also shows a reduction of the increase rate, but with a smaller scale.

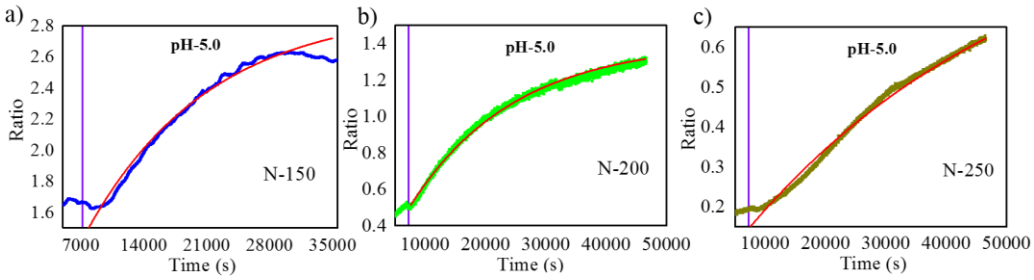

Figure 4.12: Ratio of the maximum intensity of the signal band to the maximum intensity of the reference band as a function of time, for samples with (a) N = 150, (b) N = 200, (c) N = 250. The line in each graph is the best fit for an exponential function as described in the text.

All the plots were fitted with an exponential function to a model consisting of a constant added to an inverted exponential decay (equation 4.2), i.e,

$$R(t) = R_{max} + A \cdot \left(1 - \exp\left(-\frac{t - t_{max}}{t_{release}}\right)\right) \qquad (4.2)$$

where $R(t)$ stands for the ratio as a function of time, R_{max} and t_{max} are taken for each graph as the ratio and time of the maximum measured ratio, while the model variables are the Ratio Amplitude (A) and the characteristic release time ($t_{release}$). During the analysis, neither points corresponding to the wetting nor the points corresponding to pH 7.4 are included in the fitting. The data that can be extracted from this model fitting help in correlating ($t_{release}$) between the different samples. The results of the fitting analysis are given in table 4.3.

Table 4.3: Characteristic Release Times estimated from the time evolution of the ratio between the signal band intensity and the reference band intensity.

Samples	$t_{release}$ **(minutes)**
N = 150	226.46
N = 200	288.15
N = 250	783.96

Since this study mainly focuses on the development of a methodology to evaluate the drug release from different porous nanostructures, the correlation between the characteristic release time and the pore length can be obtained. However, such correlation is not linear: a 33% increase in pore length from N = 150 to N = 200 results in a 27% increase in characteristic release time. Instead, a further 25% increase in length from N = 200 to N = 250 results in a 172% increase in characteristic release time. The correlation between the NAA-GIFs length and the characteristic release time can be explained by the fact that the time needed by the cargo molecule molecules trapped deeper in the pores is longer.

These experiments demonstrate that tailoring the optical properties of NAA in the form of NAA-GIFs permits the evaluation of the release dynamics of the cargo molecule in real-time. The analysis performed aims to provide the effect of pH responsiveness of the NAA-GIFs and to establish a method to compare the performance of several different nanostructures used in drug delivery.

4.7 Final remarks

This study performed in this chapter successfully demonstrates the ability of NAA-GIFs to be used as an optical platform for analyzing the loading and release of a cargo molecule. To achieve this, NAA-GIFs composed of two

photonic stopbands have been obtained, infused with the cargo molecule, and monitored optically for their loading and releasing patterns.

Experiments consisting of successive drop-casting of the drug solution followed by solvent drying were carried out to load the NAA-GIFs with different amounts of drug and confirm the numerical predictions. UV-VIS spectroscopy can analyze the relative height of the high reflectance bands of the PSBs while it is being filled with the cargo molecule. Real-time release measurements were carried out in a flow cell connected to a fiber spectrophotometer that allows measuring the changes in the stopbands during the release process. In this regard, the modification of NAA-GIFs with the polyelectrolytes helps in preventing the burst release of the cargo molecule and thus opens up the possibility to measure the real-time changes in the maximum signal of the NAA-GIFs while different pH solutions are flown within the flow cell. This permits a study of the release dynamics from these porous structures. We believe that the methodology developed in this chapter, exploiting the optical properties of the porous nanostructures can be further applied to the study of drug delivery systems to obtain information about the filling process and real-time data for the drug release.

Chapter 5

Real-time monitoring of Doxorubicin Release from Hybrid Nanoporous Anodic Alumina Structures

5.1 Introduction

This chapter is one step forward from the advancements in the methodology that have been explored in chapter 4. With a view to drug delivery applications, recent advances in the local administration of the drug molecules have involved a range of nanoporous materials ranging from nanoporous silicon, anodic titania, and alumina due to their excellent drug loading capacity, stability, versatile chemical functionality, and biocompatibility. This local administration can be helpful in many cases as it leads to controlled drug release directly at the targeted site. Usually, the drug release from these nanoporous structures is calculated through the in-vitro collection of the sample at pre-fixed time intervals under static conditions (UV-Visible and PL spectroscopy). However, these static systems fail to imitate the dynamic behaviour of the drug release. When the releasing medium gets filled with the drug molecules after a specific time interval, the concentration gradient between the substrate (NAA in this case), and the medium decreases, which directly affect the drug release rate, thus resulting in an imprecise value. Since the fluids inside the body are always in dynamic motion, it is crucial to understand the kinetics and mechanisms involved in real-time to reveal the true nature of drug release from these nanoporous structures.

As explained in chapter 4, NAA-GIFs can be successfully used to measure the real-time release of the drug from the structure modified with the polyelectrolyte multilayers. The methodology adopted permits obtaining a correlation between the different pore lengths and characteristic time release ($t_{release}$). Keeping this analogy in mind, the ultimate aim of this chapter can be differentiated in the following ways:

1) Preparation of a single photonic stop band (PSB) that can be tuned to estimate the drug concentration within the nanoporous structure

2) Although the polyelectrolyte multilayers applied in the previous chapter permitted to differentiate the time events between the wetting and the start of the release process, it had been observed that the wetting process usually takes place in less than a minute, and therefore, in this chapter, we consider that distinguishing both the events is not an essential requirement to study the release dynamics.
3) The work described in the previous chapter consists of two stacked GIFs structures which were used to provide a wavelength range for signal and reference band. In this chapter, the GIFs structure with the PSB in the reference range is removed since the reference signal can be taken just from the spectrum of the whole sample in a wavelength range far from the drug absorption.

   In addition, instead of the second GIF, the structure is completed with a straight pore structure that acts as a reservoir for the drug. One of the objectives of this chapter is to study the influence of the length of this reservoir as well. To achieve the points mentioned above, the Hybrid nanoporous anodic alumina-gradient index filters (Hy-NAA-GIFs) has been engineered in such a way that leads to the formation of the top part displaying a single photonic stopband leading to the formation of a modulated structure while the bottom part in the form of the straight structure acts as a drug reservoir. Two different anodization processes namely, sinusoidal current anodization and constant potential anodization have been applied to obtain samples having different thicknesses. Also, a pore widening process is performed to increase the pore diameter to allow free movement of molecules and adjusting the position of the PSB within the absorption range, followed by the drug loading process with the drop-casting method (described in chapter 3). In addition, the loading process was characterized

for any changes in the relative height of the PSB and the changes in the spectrum far from the absorption region using UV-VIS spectroscopy.

This step was followed by the real-time analysis of the DOX release process using reflectance spectroscopy by measuring the changes occurring in the signal and comparing it with the reference to evaluate the influence of varying different pore lengths and flow rates. Finally, the registered spectra are processed with MATLAB and the maximum reflectance of the signal with respect to the reference has been taken as an estimate of the amount of the remaining drug inside the nanoporous structure. Then, the evolution with time this estimate has been fitted to a model consisting of a sum of two inverted exponential decay function revealing two different characteristic times ($\tau_1$and τ_2), demonstrating the diffusion-controlled release from Hy-NAA-GIFs.

5.1.1 Doxorubicin hydrochloride (DOX)

Doxorubicin hydrochloride (DOX), an anti-cancer drug, is chosen for this study. It is considered as a natural anthracycline widely used for chemotherapy purposes to eliminate several tumors in multiple cancer treatments. Although the mechanism is not fully understood yet, it is believed to interact with DNA through the intercalation process (Anders et al. 2013). It is used intensively in conjugation with several nanoscale materials for drug delivery applications (Senapati et al. 2018). The structure can be represented as follows

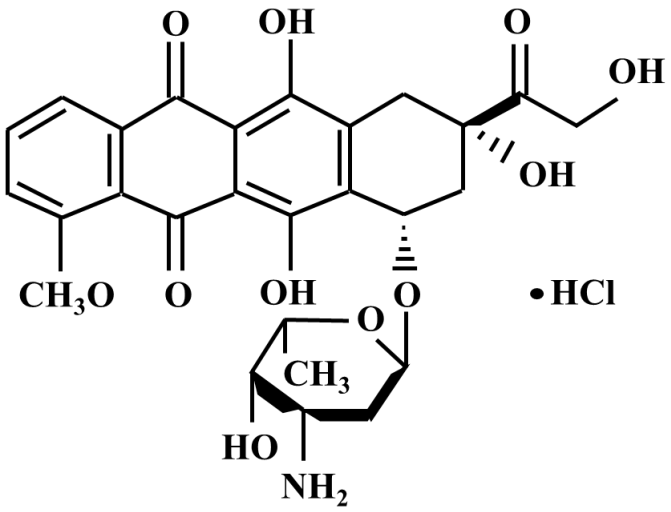

Figure 5.1: Structure of doxorubicin hydrochloride

5.2 Fabrication of Hy-NAA-GIFs

To determine control over the engineering of NAA, a heterogeneous approach was taken in this chapter which leads to the fabrication of advanced photonic architectures. As a result, Hy-NAA-GIFs samples were prepared by a one-step electrochemical process combining two different anodization profiles. The electropolishing step was similar to the one carried out in the previous chapter. To obtain the modulated structure on the top part of the Hy-NAA-GIFs, a sinusoidal current density profile variable with time was applied in an electrochemical cell containing 0.3 M oxalic acid at 5.5°C under controlled stirring. The sinusoidal parameter applied in this study were obtained with j_0 = 2.6 mA/cm^2, j_1 = 1.3 mA/cm^2 ; T = 133 s, N =150 periods. This step was followed by constant potential anodization profile to grow the straight channels by controlling a total employed charge with a voltage of 40 V to obtain different lengths of the bottom part of the structure. Following this procedure, three different sets of samples were prepared and denoted as short, medium, and long Hy-NAA-GIFs samples (figure 5.2).

The sinusoidal current density anodization profile was applied with a Keithley 2400 source controlled by LabVIEW® software program based on the following dependence of current density with time (equation 5.1):

$$j(t) = j_0 + j_1 \cdot \sin\left(\frac{2\pi}{T}t\right) \text{ for } 0 < t < N \cdot T \quad (5.1)$$

where *j(t)* corresponds to the current density at the time *(t)*, j_0 and j_1 are the average current density and the amplitude of sinusoidal current density variations. *T* represents the time period of the sinusoidal variations and N is the number of cycles applied.

It has been noticed with the previous experiments that removing the aluminium from the backside helps in improving the contrast of the PSB in the reflectance spectrum and also allows to see the interferometric color with the naked eye. Therefore, the aluminium layer at the bottom was etched in a solution of HCl (100 mL in 400 mL H_2O) and $CuCl_2$ (13.6 g added to the HCl/H_2O mixture). This step was followed by a pore widening step which was performed in 5 wt% H_3PO_4 at 35 °C for 10 min for all the samples fabricated.

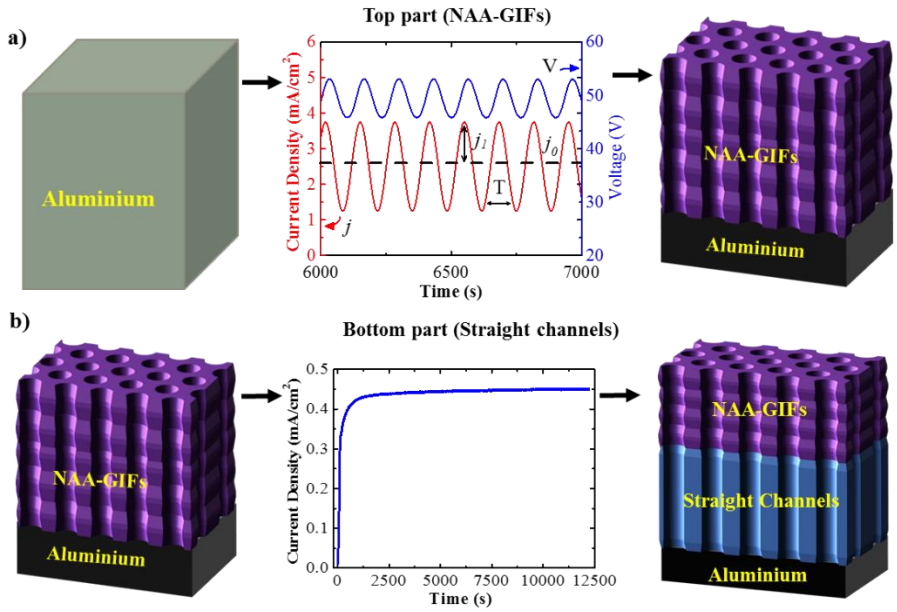

Figure 5.2: Schematic diagram of the electrochemical approach applied to prepare Hy-NAA-GIFs. a) represents a sinusoidal current density anodization profile j and V to obtain the modulated structure on the top part of the structure. j_1 is the measured cell current density for the amplitude of sinusoidal variations and j_0 represents the offset current density, T depicts the time period of the process; b) shows the constant potential anodization process to obtain the straight channels at the bottom.

5.2.1 Anodization profile

Figure 5.3 demonstrates the profiles obtained by combining the sinusoidal and constant potential anodization processes. Figures 5.3 a), d) and g) shows the sinusoidal profile consisting of applied current density and measured voltage along with the time for the samples fabricated with current density offset (j_0 = 2.6 mA/cm^2), current density amplitude (j_1 = 1.3 mA/cm^2); period (T = 133 s), number of periods (N =150). Figures 5.3 b), e) and h) depict the magnified version of the figures 5.2 a), d), and g) respectively) in between the time

instants t = 5,000 s - 8,000 s. Once the sinusoidal anodization is completed, a constant voltage of 40 V was applied and the current density vs time transients was recorded for all the samples to obtain different lengths at the pore bottom (figures 5.3 c), f), and i).

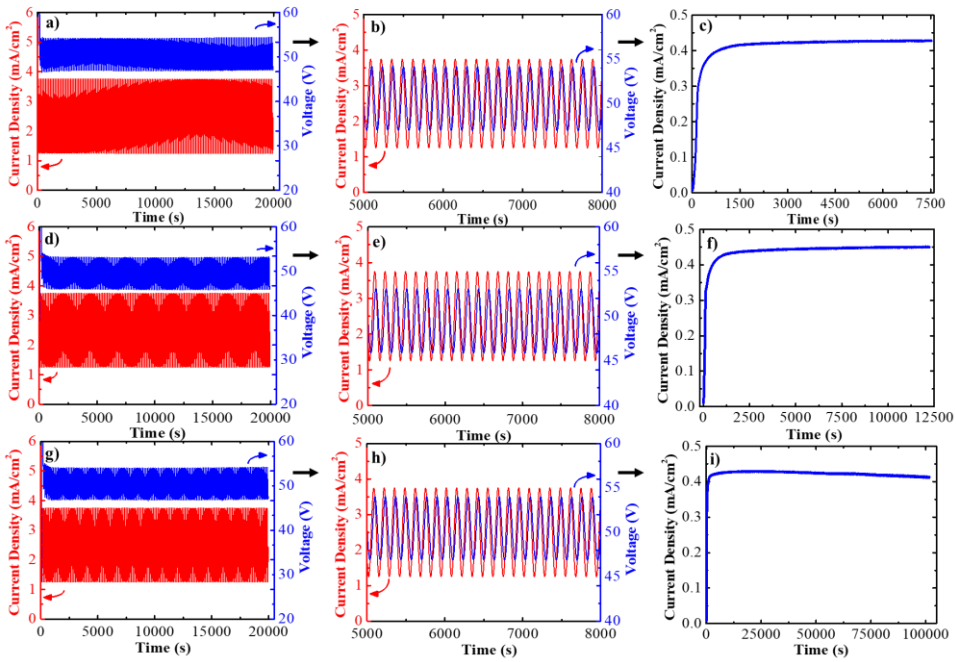

Figure 5.3: The figure represents the anodization curves obtained for Hy-NAA-PC as a result of sinusoidal and constant potential anodization for short (a-c), medium (b-f), and long samples (g-i) respectively.

Figures 5.3 a), d) and g) show the complete evolution of the sinusoidal anodization profile with the time instants between t = 0, and t = 20000 s. It can be apparent from all the graphs that there is an initial transient in the measured potential followed by the anodization voltage resembling the sinusoidal behaviour follows the current sinusoidal variations with a delay. Figure 5.3 b), e), and h) depict more detailed profiles of applied current density and voltage as a function of time where the delay can be observed along with the sinusoidal

behaviour of the measured voltage in between t = 5000 s - 8000 s. The anodization experiments performed allows a precise modulation of the porosity through sinusoidal variations with the anodization voltage varying between 45 V- 53 V with an average of 49 V for all the samples fabricated in this chapter. Figures 5.3 c), f), and i) shows typical current density-time transients curves during which the growth of the structure shifts from the modulated morphology to the straight channels with a constant anodization voltage of 40 V for all the samples. The anodization profiles described above confirmed the fabrication of a Hy-NAA-GIFs structure based on the electrochemical conditions provided. It has been shown that when a controlled sinusoidal current is applied, the system reverts to a sinusoidal anodization voltage with the same period for all the samples. Therefore, these variations in voltage lead to pore diameter modulation inside the structure. For the constant potential anodization method, a noticeable change in the current density-transient curves was observed for all the samples where an exponential increase in current density is observed until a maximum is achieved. Usually, this step is attributed to the rearrangement of pores on the surface for further growth of the structure. It should also be noted this anodization was performed subsequently to the sinusoidal current density anodization and without dismantling the cell, therefore one can presume the disordered arrangement of pores on the top of the surface. Also, a gradual decrease in current density is observed for long samples which could be possible because of the limitation in the diffusion of the ions deep inside the pores (Zaraska et al. 2010)(Nasirpouri et al. 2009).

5.3 Sample Characterization

5.3.1 Scanning Electron Microscopy

Figure 5.4 summarizes the structural characteristics gathered from SEM for the Hy-NAA-GIF structures fabricated in this chapter. Figures 5.4 a), b), and c) represent the top-view whereas figures 5.4 d), e), and f) show the cross-sectional image taken for as-produced structure for short, medium, and long samples respectively. Figure 5.4 g) represents the magnified version of figure 5.3 e) in graphical form.

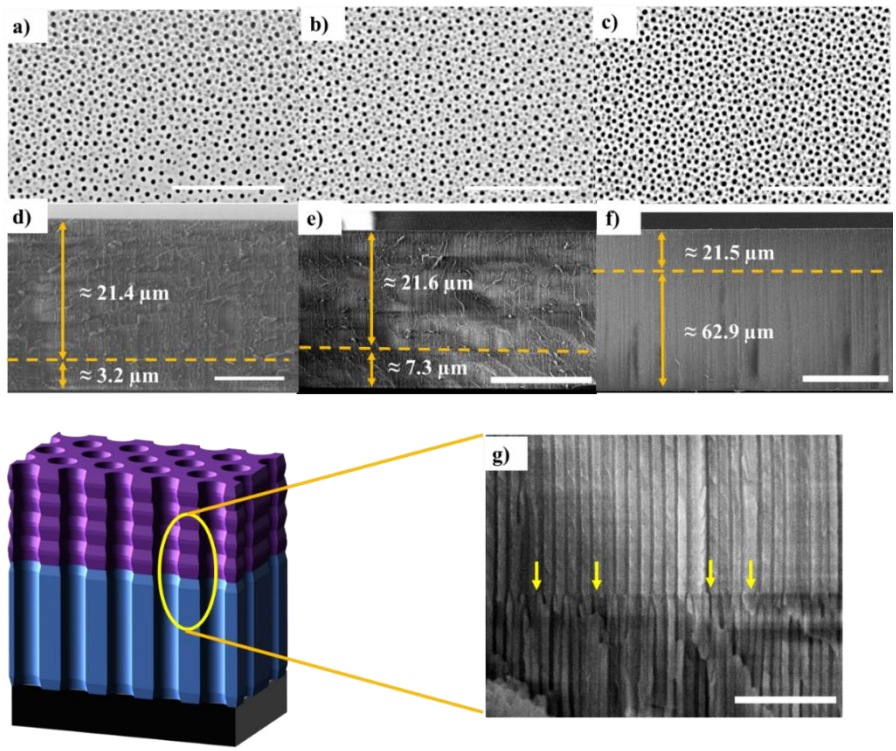

Figure 5.4: SEM pictures of Hy-NAA-GIFs structure obtained with the sinusoidal parameters and different current-density vs time parameters. a), b), and c) represents top view (Scale bar = 1µm) and c), d), and e) demonstrates cross-section (scale bar = 10, 20 and 50 µm respectively) for the short, medium, and long samples respectively. g) interface between the modulated

pore and straight pore parts of the structure caused by the change in the anodization process indicated by arrows.

The images were obtained to confirm the fabrication of a Hy-NAA-GIFs structure based on the aluminium with the sinusoidal current anodization and constant potential anodization profile. In figures 5.4 a), b), and c) the top-view SEM images reveals the random arrays of nanopores distributed across the surface with an average pore diameter of 39 ± 3 nm and an average interpore distance of 98 ± 16 nm estimated with the ImageJ software. The cross-section analysis was also performed for all the samples which help in measuring the total thickness of the prepared samples. For short samples, the modulated structure was found to be around 21.4 µm long while the straight channel was 3.2 µm long only (figure 5.4, d). On the other hand, the medium samples revealed a length of 21.6 µm for the modulated structure and 7.5 µm for the straight (figure 5.4, e). Similarly, the long samples showed a length of 21.5 µm for the modulated and 62.9 µm for the straight channel (figure 5.4 f). The obtained images clearly reveal a noticeable change in the structure while switching from sinusoidal to constant potential anodization process (figure 5.4, g). The measurements obtained for the Hy-NAA-GIF through digital images depict the correct translation of stacked layers of GIF fabricated through sinusoidal current anodization on the top part followed by the formation of straight channels as a result of constant potential anodization profile at the bottom.

5.3.2 UV-Visible Spectroscopy

As stated above, the Hy-NAA-GIFs structure is obtained by using a combination of two different anodization regimes. The analysis carried out in the previous chapter allows obtaining the correlation between the height of the stopband and the concentration of filling species within the rugate structure.

Therefore, in this chapter, the top part consists of GIF while the bottom part is straight pores. The GIF has a PSB that in the spectrum shows as a high reflection band which can be used as a ¨signal¨ to estimate the amount of drug within the pores. On the other hand, the bottom part adds length to the different pore structures with a minimal contribution to the spectrum (only Fabry- Perot interferences). For confirming the as-prepared samples to display the characteristics mentioned above, UV-visible spectra were recorded.

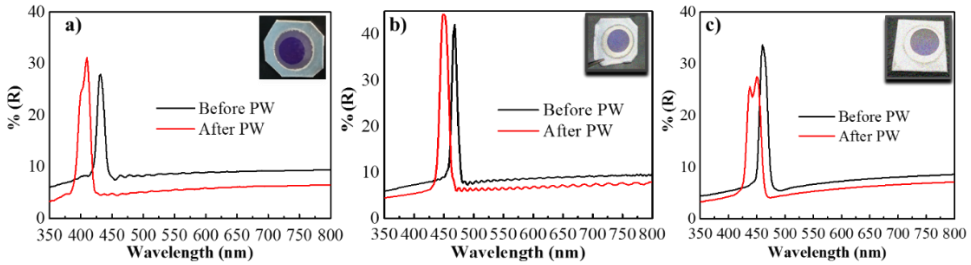

Figure 5.5: Reflectance spectra (a, b, and c) of Hy-NAA-GIFs structure obtained for short, medium, and long samples respectively. Inset shows the digital pictures of as-obtained samples showing the interferometric color.

For the short samples (figure 5.5 a), the maximum reflectance was recorded at 432 nm with a reflectance of 27.9 % before the pore widening (PW) whereas it shifted to 410 nm with a reflectance of 31.1 % after the PW process. For the medium samples (figure 5.5 b), the signal channel was recorded at 468 nm with a reflectance of 42 % and 448 nm with a reflectance of 44.3 % before and after PW. Finally, for long samples (figure 5.5 c), before PW, the signal channel appeared at 460 nm with a reflectance of 33.6 % while it moved to 450 nm with a reflectance value of 27.5 %. These results confirm the presence of the desired signal channel for the DOX within the maximum absorption region (480-500 nm), in addition to the necessary reference wavelength range required far from the absorption (700-850 nm). However, for the long samples,

an additional side lobe was observed as a result of sharp truncation of the effective refractive index specifically at the boundaries of the Hy-NAA-GIFs (Ilyas et al. 2007).

5.3.2.1 DOX analysis

To confirm the absorption of the DOX within the same range as defined as a PSB in the top part of the structure, UV-VIS spectra of the DOX were measured at a concentration of 5 μg/ml in PBS (0.01 M having a pH of 7.4) (figure 5.6 a). The drug was dissolved in a PBS solution and measured in a 1 cm optical path cuvette at room temperature. With this result, we were able to confirm the presence of the peak at 480 nm that falls within the desired region of the PSB with a characteristic full-width half-maximum (FWHM) of 104.1 nm.

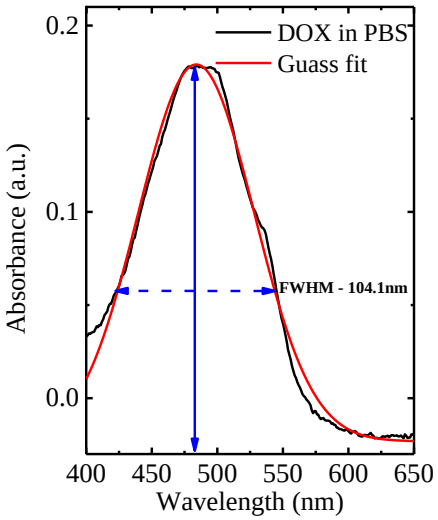

Figure 5.6: UV-Vis spectra obtained for doxorubicin in PBS having a concentration of 5 μg/ml with a FWHM of 104.1 nm.

5.3.2.2 DOX Loading by the drop-casting method

Inspired by the research in the previous chapter which in-depth describes the filling pattern of a drug inside the NAA-GIF structure having two PSBs (Kapruwan et al. 2021), we applied the drop-casting method here as well to define a metric as the ratio between the maximum reflectance and the average reflectance of a wavelength range far from absorption of DOX for Hy-NAA-GIFs.

In brief, DOX solution in ethanol (500 µg/ml) was prepared and 10 µL was dropped onto the surface of the sample followed by air-drying at room temperature. This step was repeated 6 times sufficient enough to fill the structure followed by the subsequent measurement by UV-VIS spectroscopy after each step.

Figure 5.7 a) represents the UV-VIS spectra recorded after each drop/dry cycle and their impact on the signal and reference wavelength ranges. As the first drop of the drug is added to the structure, it leads to a change in the effective medium of the Hy-NAA-GIFs resulting in a slight decrease in the maximum reflectance value from 31.1 % to 27.3 % at 410 nm. This value further fluctuates but overall a 31.9 % decrease in the value of reflectance is observed from 31.1 % to 21.2 % after the addition of the 6^{th} drop. In addition, minor variations in the reflectance value have also been observed in the non-absorption region (also referred to as reference wavelength range) of the hybrid structure which also leads to an assumption of a change in the dielectric constant of the medium of the straight channels due to penetration with the drug molecule. The trend observed during the infiltration process is not homogenous as it can be predicted that during the drop/dry procedure the concentration of the drug molecules inside the pores is continuously increasing, hence making it difficult for further molecules to enter inside.

Figure 5.7 b) shows a plot demonstrating a decrease in the trend of the maximum reflectance of the signal at a wavelength of 410 nm as compared to a slight change in the intensity of spectrum at a wavelength of 800 nm far from the absorption range.

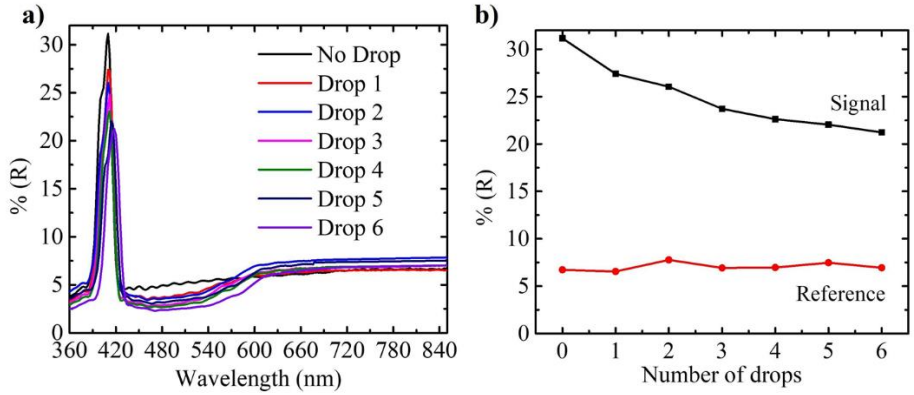

Figure 5.7: a) Reflection spectra recorded for Hy-NAA-GIF fabricated with j0 = 2.6 mA/cm2, j1 = 1.3 mA/cm2; T = 133 s, N =150 periods for short length sample after each drop/dry cycle, b) illustration of maximum reflectance obtained for the signal (410 nm) and reference wavelength ranges (800 nm) as a function of the number of drops applied.

The above-mentioned results successfully confirm that the drop-casting method is one of the effective methods to infiltrate the pores and simultaneously can be analysed for the successful filling by recording the spectra before and after filling using UV-Visible spectroscopy.

5.4 Real-time drug release measurements by Reflectance Spectroscopy

Once the Hy-NAA-GIFs was tested successfully for the infiltration of DOX with the drop-casting method, the same protocol was applied without any changes for DOX loading in all the samples for studying the release kinetics in real-time. Samples were placed in a flow cell setup that permits the

measurement of the sample reflected intensity while PBS flows through the porous structure, as described in the experimental methods (chapter 3). The spectra were registered every 10 seconds with a stabilization time of 10 minutes before the flow of PBS was first injected. Figure 5.8 shows two of the measured spectra as an example. Figure 5.8 a) corresponds to a 25 µm (short) sample in an experiment carried out at a flow rate of 80 µl/min while figure 5.8 b) corresponds to an 85 µm (long) sample in an experiment with a 140 µl/min.

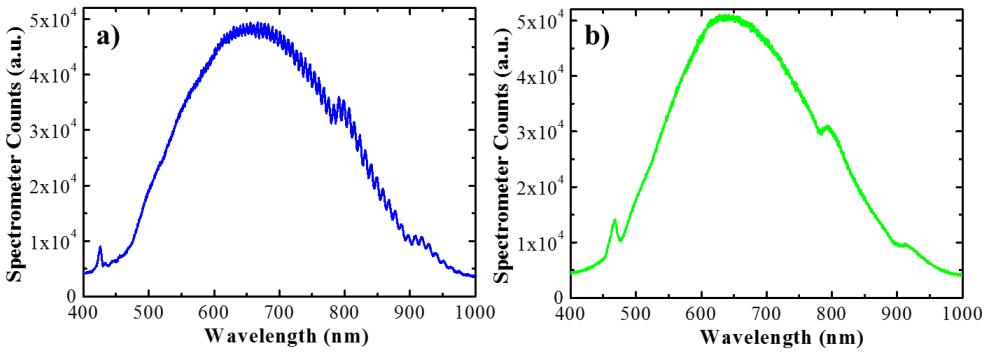

Figure 5.8: The measured spectra of Hy-NAA-GIFs with reflectance spectroscopy for short (a) and long (b) samples respectively.

The magnitude measured by the fiber spectrometer is a number of counts and corresponds to the combined lamp emission spectrum, sample reflectivity and detector sensitivity. The plots show different features, the main being the local maximum between 430 nm and 500 nm caused by the higher reflectance of the gradient-index filters present in the sample. The spectrum for the thinner sample also shows oscillations resulting from the Fabry-Pérot interferences between the two reflections of the spectrometer beam at the extreme interfaces of the porous nanostructure. These oscillations are not present in the long sample as the coherence length of the beam is too small to sustain them.

In the release experiment, time *t* is set *t = 0* at the instant the PBS is injected into the flow cell. At such an instant the wetting of the pores takes place and results in a turbulent flow on the very path of the spectrometer beam that severely interferes with the measurement. After this wetting, the signal stabilizes, and the measured spectra become reliable. The spectra shown in figure 5.9 correspond to instant *t = 1 min.* to $t = 3.6 \cdot 10^4\ s = 600\ min$. As the drug is released from the nanostructure its concentration within the gradient-index part of the porous structure decreases and produces an increase in the maximum signal of the local maximum. At the same time, since the drug has a very small absorption above 650 nm, the spectra should show very little variation in this range. To illustrate this point, figures 5.9 (a, and b) show the spectra in the wavelength ranges between 430 nm and 500 nm (Figure 5.9 a) and between 700 nm and 800 nm (figure 5.9 b), at the different release times indicated in the legend.

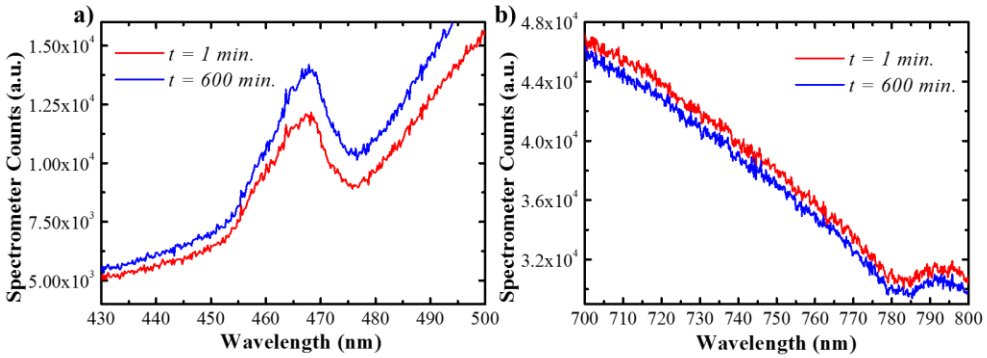

Figure 5.9: The spectra registered after wetting using reflectance spectroscopy at time instants t = 1 and 600 min. for signal (a), and reference wavelength ranges (b) in Hy-NAA-GIFs.

These two figures show that the maximum signal at the PSB wavelength range shows an increase of 15%, while the signal at the 700-800 nm range shows a

decrease of 3%. The increase in the PSB wavelength range confirms that it can be used to estimate the variation in DOX concentration within the gradient-index filters part of the nanopores. Figure 5.9 b) also shows that after 10 hours of measurement, the signal in the measurement systems has drifted. This drift must be compensated for to achieve reliable estimates of the drug release dynamics.

To compensate for the observed drift as well as for the possible noise in the measured spectra, a reference spectrum ($R(\lambda)$) for the 700-800 nm range is determined as the average of all measured spectra with reliable signal in this range in the release experiment. Here, the term reliable signal refers to all those spectra registered after the wetting process of the pores with the stabilized signal. Then, by comparing the spectrum $S_i(\lambda)$, taken at time instant t_i with the reference spectrum in the 700-800 nm range, it is possible to correct the spectrum in all the measured ranges. In this work, we modelled the effect of the fluctuations as an affine transformation. With this, within the 700-800 nm range the measured spectrum should be (equation 5.2):

$$S_i(\lambda) = A_i \cdot R(\lambda) + B_i, \;\; 700\,nm < \lambda < 800\,nm \tag{5.2}$$

where the constant A_i accounts for a change in scale (that could model a change in beam intensity) while B_i accounts for a change in background signal (that could be attributed to noise). Assuming constants A_i and B_i do not depend on the wavelength, they can be estimated by minimizing a merit function defined as (equation 5.3):

$$F(A_i, B_i) = \sum_{\lambda=700\,nm}^{\lambda=800\,nm} |S_i(\lambda) - A_i \cdot R(\lambda) - B_i| \tag{5.3}$$

The A_i and B_i that minimize F permit to obtain the corrected spectrum applying the inverse affine transform (equation 5.4):

$$S_{i,corrected}(\lambda) = \frac{S_i(\lambda) - B_i}{A_i}, 430\ nm < \lambda < 500\ nm \quad (5.4)$$

This corrected spectrum is then used to evaluate the height of the local maximum in the PSB wavelength range.

In this range, as it can be seen in Figure 5.9 a), the feature corresponding to the reflectance of the sample appears overlapped to a baseline corresponding to the combined effect of the straight pore structure optical properties and the lamp spectral intensity and detector spectral sensitivity. To properly evaluate the evolution of this maximum reflectance is necessary to distinguish the local maximum related to the gradient-index part of the structure from the baseline. This is accomplished by finding the best fit between the corrected spectrum $S_{i,corrected}(\lambda)$ and a model function consisting of the sum of a gaussian component (which accounts for the maximum in reflectance) plus a third-degree polynomial (which accounts for the baseline, equation 5.5):

$$G_i(f) = \alpha \cdot \exp\left(-\left(\frac{f-\beta}{2\sigma}\right)^2\right) + \gamma + \delta \cdot f + \epsilon \cdot f^2 + \theta \cdot f^3 \quad (5.5)$$

where f is the inverse of the wavelength ($f = \frac{1}{\lambda}$), which is proportional to the photon frequency or energy. In this function, parameter α is the height of the gaussian, β is the center frequency of the gaussian and σ is its spread. Parameters γ, δ, θ, and ϵ are the polynomial coefficients. By using the inverse of wavelengths as the variable of the fitting function, better parameter estimates are obtained. Figure 5.10 shows an example of such best fit for the same data shown in previous figure 5.9, after correction. The value of the Gaussian height, indicated in the figure, is used as an estimate of the maximum reflected intensity from the rugate part of the porous nanostructure.

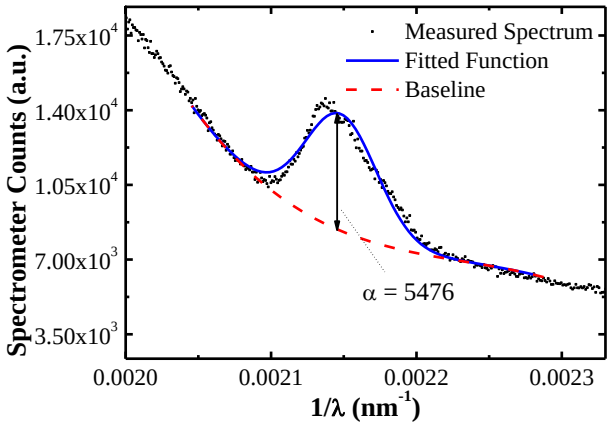

Figure 5.10:The fitted curve obtained for the maximum reflectance of the signal channel in Hy-NAA-GIFs.

Applying this process to all the measured spectra in a flow cell drug release experiment, the evolution with time of this signal (the Gaussian height, α) can be obtained. An example of the signal evolution with time is shown in Figure 5.11. Values for $t < 0$ are not represented as they correspond to the flow cell without the fluid. The first represented point in the plot corresponds to $t = 1{,}35\ min$. Before this time, the signal is distorted by the pore wetting process. When the signal stabilizes it shows a clear increasing trend. This trend has a steeper ascent at the beginning and then reduces its growth rate until it plateaus, indicating no more drug is being delivered from the porous nanostructure. All the measurements for all the studied samples show similar behaviors.

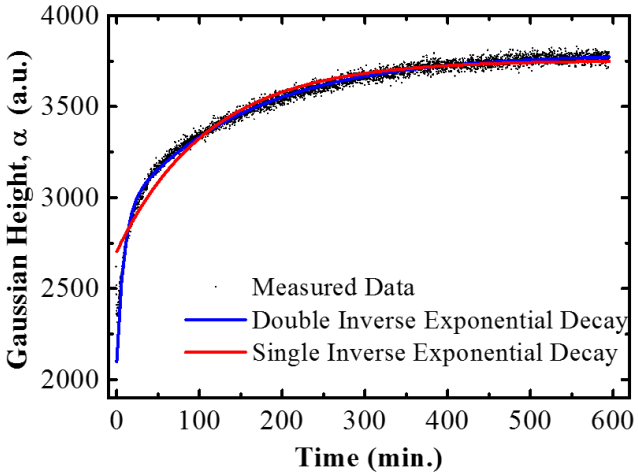

Figure 5.11: The graph represents the best fitting obtained with the model being applied for the time evolution of the signal for Hy-NAA-GIFs.

To extract information from the evolution of the signal with time, a further analysis by best fit to a model has been applied. Different models have been tested and the one that leads to the best results is the sum of two inverted exponential decays with the same starting point and with two different time constants (equation 5.6):

$$\alpha(t) = \alpha_0 + \kappa_1 \left(1 - \exp\left(-\frac{t}{\tau_1}\right)\right) + \kappa_2 \left(1 - \exp\left(-\frac{t}{\tau_2}\right)\right) \quad (5.6)$$

In this expression α is the value of a signal at $t = 0$ which is unknown because of the distortion of the spectra during the wetting phase. Parameters κ_1 and κ_2 are the relative weights of the two inverse exponential decay components. Finally, $\tau_1$and τ_2 are the time constants of the two exponential decays. Figure 5.11 includes the result of the best fit of the data to this double inverted exponential decay. In the previous chapter, a similar model with a single inverse exponential decay was used to analyze the time evolution of the signal. The best fit for a single inverse exponential decay is also shown in Figure 5.11.

It demonstrates that the simpler model cannot reproduce the two regimes of variation present in the data characterized by the two-time constants τ_1 and τ_2.

Figure 5.12 shows a summary of the obtained time constants for the three studied pore lengths (Figure 5.12 a) and the two studied flow rates (Figure 5.12 b). For the three pore lengths time τ_1 is between 2 and 16 minutes, while time τ_2 increases from 53 minutes for a total pore length of 24.6 µm to 170 minutes for the total pore length of 84.4 µm. If different flow rates are considered, Figure 5.12 b shows that time constant τ_1 is not influenced by the flow rate, with a value of 16 minutes for both flow rates. On the other hand, time constant τ_2 decreases with increasing flow rate from a value of 170 minutes for the slowest flow rate (80 µl/min) down to 71 minutes for the highest rate (140 µl/min).

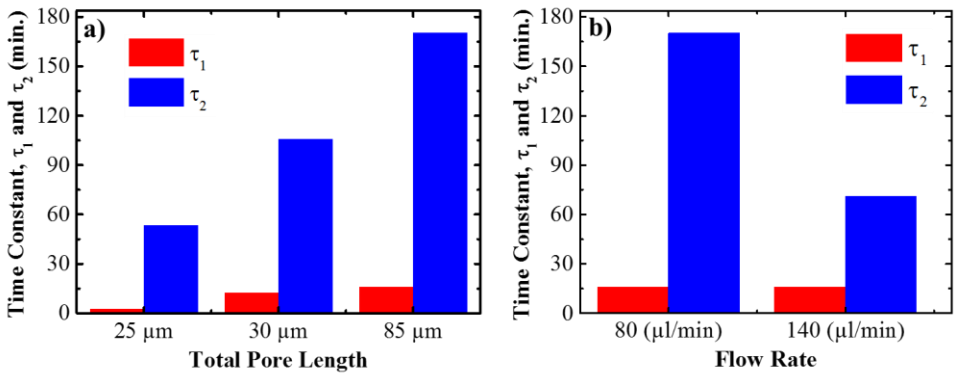

Figure 5.12: The trend in two different characteristic time release of drug from the whole structure as a function of total pore length (a) and flow rate (b) respectively.

These results suggest that the two characteristic times correspond to two different mechanisms in the release process. The increase of τ_2 with pore length and its decrease with flow rate are both in good agreement with a

diffusion-controlled release of the drug from the pores. Instead, τ_1 is fairly invariant both for the different pore lengths and the different flow rates. This may be related to a specific effect of the gradient-index filters top part of the pores. This part is the first to be filled by the liquid even before the liquid can reach the bottom, so the release from this part is started earlier and at a faster rate (hence the smaller τ_1 value) than the diffusion-controlled release from the structure considered as a whole.

5.5 Final remarks

The research carried out in this chapter demonstrates the ability of Hy-NAA-GIF to be used as an advanced photonic structure suitable for analyzing the loading and release of doxorubicin molecules. To demonstrate this, Hy-NAA-GIF structures were prepared, loaded with the drug solution using drop-casting method followed by the measurement with UV-Vis and afterwards, monitored in real-time by reflectance spectroscopy to further evaluate the releasing kinetics.

In comparison to the nanostructures with two PSBs prepared in the previous chapter, here nanostructures with only one PSB that can be tuned to fall within the drug absorption region are applied. Instead of a second PSB, in this work, the intensity of the spectrum in a wavelength range far from drug absorption acts as a reference. The drop-casting method helps to predict the changes in the filling process by analyzing the relative height of the PSB reflectance maximum with the average reflectance at the reference wavelength range. Once loaded with the drug, these structures are placed in a flow cell setup connected to reflectance spectroscopy setup and data processing capable of evaluating the drug release in real-time. This permits to obtain an estimate of the amount of drug infiltrating the pores as a function of time. This is then

analyzed with a model consisting of a sum of two inverted exponential decay functions with two different characteristic times, $\tau_1$and τ_2.

The experiments were conducted by varying two parameters i.e., different flow rates and pore lengths. Results show that increasing pore length results in a corresponding increase in τ_2, without much significant change in τ_1. On the other hand, increasing the flow rate also results in a decrease of τ_2, while τ_1 is unaffected. This reveals the existence of a contribution to release related to the wetting of the top GIF part of the structure characterized by τ_1 followed by a diffusion-controlled release from the whole length of the pore characterized by τ_2. We believe that the approach developed in this chapter can be further applied to gain information about the loading process of the drug and to further study the drug-releasing behavior in real-time from porous nanostructures.

Chapter 6

Summary and Conclusions

This chapter provides a general conclusion of each chapter and summarizes the main achievements obtained during the PhD thesis. In addition, a glance to the future work has also been proposed. The main aim of this thesis is to study and evaluate the possibilities of photonic nanostructures based on nanoporous anodic alumina in drug delivery applications.

To start with, in chapter 2 a state of art has been presented which discusses the fundamentals of NAA starting right from its history to the recent developments over the past few years. Also, different types of anodization methods along with the resulting structural characteristics have been elaborated. This chapter also provides a general introduction to photonic crystals and their surface modifications through wet chemical procedures. To load different molecules inside Nanoporous anodic alumina, a subsection has been included revealing all the methods that can be utilized for an effective filling. Finally, an overview of the different NAA platforms with possible applications has been discussed to grasp an idea about the utilization of this material in biomedical applications.

To gain more understanding about NAA, **chapter 3** describes the experimental methods and numerical simulations tools applied in this PhD thesis. Two different types of anodization processes i.e. sinusoidal current density and constant potential anodization methods have been applied to obtain advanced nanostructures revealing different PSBs that can be tuned within the desired region. It has been shown that the post-treatments directly affect the morphological and structural characteristics of the photonic structures. Several optical techniques such as PL, UV-VIS, RS have been used to record all the changes happening mainly in the PSB because of infiltration and release of drug molecules. To support this, the TMM method has been applied to gain knowledge about the optical properties of the photonic

nanostructures and how they change when loaded with the drug or when they release it.

Chapter 4 deals with the fabrication process of NAA-GIF through the sinusoidal anodization method described in chapter 3. The chapter focuses on the preparation of NAA-GIF structures with different lengths and a strategy has been used to utilize them as an optical platform for the loading and release of Rh6G. The structures were prepared specifically with the two PSBs where one of its bands falls within the absorption region of the drug while the other one is far from such absorption. In addition, the drop-casting method is effective in filling the pores with the drug. To test the pH responsiveness, the structures were modified with several polyelectrolyte multilayers and drugs. In a flow cell setup connected to the spectrometer, the samples were placed, and buffer solutions with different pH (5.0 and 7.4) that emulate the release medium flowed through the cell. The main reason for choosing different pH is to control precisely the start time of the release. The spectra with the changes in the maximum signal of NAA-GIF were registered in real-time. Finally, the data were fitted with a model consisting of an exponential function defining a clear relationship between characteristic time release and pore lengths.

Chapter 5 deals with an approach that uses two different anodization regimes i.e. sinusoidal current density and constant potential anodization combined in one electrochemical step leading to the formation of Hy-NAA-GIF. These structures were loaded with the DOX drug using the drop-casting method and measured to study the release kinetics in real-time with reflectance spectroscopy. Unlike in the preparation of NAA-GIF in chapter 4 which contains two PSBs, the main advantage of preparing these structures is a single PSB that can be tuned within the absorption region of the drug while instead of a second PSB, the intensity of the spectrum can also be used. Since most of

the fluids inside the human body are in dynamic motion, to mimic the system, different pore lengths and flow rates have been tested in a flow cell setup consisting of drug-loaded samples. All the spectra were fitted to a model consisting of a sum of two inverted exponential decay functions revealing the true nature of the diffusion-controlled release from Hy-NAA-GIF structures.

All the results gathered in this PhD thesis have the potential in designing advanced nanostructures for drug delivery systems. In addition, several complicated structures can also be obtained by revising the protocols mentioned in this dissertation. By carefully analysing the infiltration process and its characterization method, more knowledge can be acquired about the filling behaviour of the drug inside the porous materials. The polyelectrolytic multilayers have been successful to hold the drug molecules inside the structure and providing ample time to study the release kinetics in real-time. The exponential model applied has been explained fully to an extent where it can be modified accordingly for other porous platforms as well. Altogether, all the methods and characterization techniques applied are encouraging and open the possibilities to take one step further in developing these structures for several real-time applications in drug delivery systems.

References

Abelow, Alexis E. et al. 2014. "Electroresponsive Nanoporous Membranes by Coating Anodized Alumina with Poly(3,4-Ethylenedioxythiophene) and Polypyrrole." *Macromolecular Materials and Engineering* 299(2): 190–97.

Acosta, Laura K. et al. 2019. "Stacked Nanoporous Anodic Alumina Gradient-Index Filters with Tunable Multispectral Photonic Stopbands as Sensing Platforms." *ACS Applied Materials and Interfaces* 11(3): 3360–71.

Alba, María et al. 2014. "PH-Responsive Drug Delivery System Based on Hollow Silicon Dioxide Micropillars Coated with Polyelectrolyte Multilayers." *Nanoscale Research Letters* 9(1): 411.

Amouzadeh Tabrizi, Mahmoud, Josep Ferré-Borrull, and Lluis F. Marsal. 2020a. "An Optical Biosensor for the Determination of Cathepsin B as a Cancer-Associated Enzyme Using Nanoporous Anodic Alumina Modified with Human Serum Albumin-Thionine." *Microchimica Acta* 187(4): 1–9.

Amouzadeh Tabrizi, Mahmoud, Josep Ferré-Borrull, and Lluis F. Marsal. 2020b. "Highly Sensitive Remote Biosensor for the Determination of Lead (II) Ions by Using Nanoporous Anodic Alumina Modified with DNAzyme." *Sensors and Actuators, B: Chemical* 321: 128314.

Amouzadeh Tabrizi, Mahmoud, Josep Ferré-Borrull, and Lluis F Marsal. 2019. "Highly Sensitive Aptasensor Based on Interferometric Reflectance Spectroscopy for the Determination of Amyloid β as an Alzheimer's Disease Biomarkers Using Nanoporous Anodic Alumina." *Biosensors and Bioelectronics* 137: 279–86.

Anders, Carey K. et al. 2013. "Pharmacokinetics and Efficacy of PEGylated

Liposomal Doxorubicin in an Intracranial Model of Breast Cancer." *PLoS ONE* 8(5): e61359.

Aramesh, Morteza et al. 2014. "Multifunctional Three-Dimensional Nanodiamond-Nanoporous Alumina Nanoarchitectures." *Carbon* 75: 452–64.

Araoyinbo, Alaba O., Azmi Rahmat, Mohd Nazree Derman, and Khairel Rafezi Ahmad. 2013. "Using Gibbs Standard State Free Energy and a Power Regulating Device to Predict and Control the Fabrication of Nanoporous Alumina." *Advanced Materials Letters* 4(12): 899–904.

Arsenault, André et al. 2004. "Towards the Synthetic All-Optical Computer: Science Fiction or Reality?" *Journal of Materials Chemistry* 14(5): 781–94.

Aw, Moom Sinn, and Dusan Losic. 2016. "Nanoporous Alumina as an Intelligent Nanomaterial for Biomedical Applications." In *Intelligent Nanomaterials: Second Edition*, Hoboken, NJ, USA: John Wiley & Sons, Inc., 127–59.

Balderrama, Victor S. et al. 2015. "Design, Fabrication and Charge Recombination Analysis of an Interdigitated Heterojunction Nanomorphology in P3HT/PCBM Solar Cells." *Nanoscale* 7(33): 13848–59.

Baranowska, Malgorzata et al. 2014. "Protein Attachment to Nanoporous Anodic Alumina for Biotechnological Applications: Influence of Pore Size, Protein Size and Functionalization Path." *Colloids and Surfaces B: Biointerfaces* 122: 375–83.

Bard, Allen J., and J. A. A. Ketelaar. 1976. "Encyclopedia of Electrochemistry

of the Elements." *Journal of The Electrochemical Society* 123(10): 348C-348C.

Bengough, G. D., and J. M. Stuart. 1923. "Improved Process of Protecting Surfaces of Aluminum and Aluminum Alloys." *UK Patent*.

Biju, Vasudevanpillai. 2014. "Chemical Modifications and Bioconjugate Reactions of Nanomaterials for Sensing, Imaging, Drug Delivery and Therapy." *Chemical Society Reviews* 43(3): 744–64.

Bosch, S., J. Ferré-Borrull, and J. Sancho-Parramon. 2001. "A General-Purpose Software for Optical Characterization of Thin Films: Specific Features for Microelectronic Applications." *Solid-State Electronics* 45(5): 703–9.

Bosch, Salvador, Josep Ferré-Borrull, Norbert Leinfellner, and Adolf Canillas. 2000. "Effective Dielectric Function of Mixtures of Three or More Materials: A Numerical Procedure for Computations." *Surface Science* 453(1–3): 9–17.

Briggs, E. P. et al. 2004. "Formation of Highly Adherent Nano-Porous Alumina on Ti-Based Substrates: A Novel Bone Implant Coating." *Journal of Materials Science: Materials in Medicine* 15(9): 1021–29.

Byrne, R. S., and P. B. Deasy. 2002. "Use of Commercial Porous Ceramic Particles for Sustained Drug Delivery." *International Journal of Pharmaceutics* 246(1–2): 61–73.

Cheow, Pui Sze, Eugene Zhi Chao Ting, Mei Qi Tan, and Chee Seng Toh. 2008. "Transport and Separation of Proteins across Platinum-Coated Nanoporous Alumina Membranes." *Electrochimica Acta* 53(14): 4669–73.

Chu, S. Z. et al. 2006. "Large-Scale Fabrication of Ordered Nanoporous Alumina Films with Arbitrary Pore Intervals by Critical-Potential Anodization." *Journal of The Electrochemical Society* 153(9): B384.

Comstock, David J. et al. 2010. "Synthesis of Nanoporous Activated Iridium Oxide Films by Anodized Aluminum Oxide Templated Atomic Layer Deposition." *Electrochemistry Communications* 12(11): 1543–46.

Le Coz, F. et al. 2010. "Chemical Composition and Structural Changes of Porous Templates Obtained by Anodising Aluminium in Phosphoric Acid Electrolyte." In *Surface and Interface Analysis*, John Wiley & Sons, Ltd, 227–33.

Cregan, R. F. et al. 1999. "Single-Mode Photonic Band Gap Guidance of Light in Air." *Science* 285(5433): 1537–39.

Dai, Jinhua, Gregory L. Baker, and Merlin L. Bruening. 2006. "Use of Porous Membranes Modified with Polyelectrolyte Multilayers as Substrates for Protein Arrays with Low Nonspecific Adsorption." *Analytical Chemistry* 78(1): 135–40.

Decher, G., J. D. Hong, and J. Schmitt. 1992. "Buildup of Ultrathin Multilayer Films by a Self-Assembly Process: III. Consecutively Alternating Adsorption of Anionic and Cationic Polyelectrolytes on Charged Surfaces." *Thin Solid Films* 210–211(PART 2): 831–35.

Delcea, Mihaela, Helmuth Möhwald, and André G. Skirtach. 2011. "Stimuli-Responsive LbL Capsules and Nanoshells for Drug Delivery." *Advanced Drug Delivery Reviews* 63(9): 730–47.

Desai, Tejal A. et al. 1999. "Microfabricated Biocapsules Provide Short-Term Immunoisolation of Insulinoma Xenografts." *Biomedical Microdevices*

1(2): 131–38.

Deshmukh, Prashant K. et al. 2013. "Stimuli-Sensitive Layer-by-Layer (LbL) Self-Assembly Systems: Targeting and Biosensory Applications." *Journal of Controlled Release* 166(3): 294–306.

Diggle, J. W., T. C. Downie, and C. W. Goulding. 1969. "Anodic Oxide Films on Aluminum." *Chemical Reviews* 69(3): 365–405.

Domingo, C., J. García-Carmona, M. A. Fanovich, and J. Saurina. 2002. "Study of Adsorption Processes of Model Drugs at Supercritical Conditions Using Partial Least Squares Regression." *Analytica Chimica Acta* 452(2): 311–19.

Eckstein, Chris et al. 2018. "Nanoporous Anodic Alumina Surface Modification by Electrostatic, Covalent, and Immune Complexation Binding Investigated by Capillary Filling." *ACS Applied Materials and Interfaces* 10(12): 10571–79.

Eftekhari, Ali. 2008. Nanostructured Materials in Electrochemistry *Nanostructured Materials in Electrochemistry*. John Wiley and Sons.

Egerton, R. F., P. Li, and M. Malac. 2004. "Radiation Damage in the TEM and SEM." In *Micron*, Pergamon, 399–409.

Fang, Jinghua et al. 2014. "Multipurpose Nanoporous Alumina-Carbon Nanowall Bi-Dimensional Nano-Hybrid Platform via Catalyzed and Catalyst-Free Plasma CVD." *Carbon* 78: 627–32.

Fares, Hadi M., Qifeng Wang, Mo Yang, and Joseph B. Schlenoff. 2019. "Swelling and Inflation in Polyelectrolyte Complexes." *Macromolecules* 52(2): 610–19.

Ferré-Borrull, Josep, Josep Pallarès, Gerard Macías, and Lluis F. Marsal.

2014. “Nanostructural Engineering of Nanoporous Anodic Alumina for Biosensing Applications.” *Materials* 7(7): 5225–53.

Flamme, Kristen E. La et al. 2005. “Nanoporous Alumina Capsules for Cellular Macroencapsulation: Transport and Biocompatibility.” *Diabetes Technology & Therapeutics* 7(5): 684–94.

Folkman, J, D M Long, and R Rosenbaum. 1966. “Silicone Rubber: A New Diffusion Property Useful for General Anesthesia.” *Science (New York, N.Y.)* 154(3745): 148–49.

Friedmann, Andrea, Andreas Hoess, Andreas Cismak, and Andreas Heilmann. 2011. “Investigation of Cell-Substrate Interactions by Focused Ion Beam Preparation and Scanning Electron Microscopy.” *Acta Biomaterialia* 7(6): 2499–2507.

Fujiwara, Hiroyuki. 2007. Spectroscopic Ellipsometry: Principles and Applications *Spectroscopic Ellipsometry: Principles and Applications*. John Wiley and Sons.

Gordeeva, Elena O., Ilya V. Roslyakov, and Kirill S. Napolskii. 2019. “Aluminium Anodizing in Selenic Acid: Electrochemical Behaviour, Porous Structure, and Ordering Regimes.” *Electrochimica Acta* 307: 13–19.

Guha Thakurta, Sanjukta, and Anuradha Subramanian. 2012. “Fabrication of Dense, Uniform Aminosilane Monolayers: A Platform for Protein or Ligand Immobilization.” *Colloids and Surfaces A: Physicochemical and Engineering Aspects* 414: 384–92.

Gulati, Karan et al. 2012. “Biocompatible Polymer Coating of Titania Nanotube Arrays for Improved Drug Elution and Osteoblast Adhesion.”

Acta Biomaterialia 8(1): 449–56.

Han, Catherine Y., Gerold A. Willing, Zhili Xiao, and H. Hau Wang. 2007. "Control of the Anodic Aluminum Oxide Barrier Layer Opening Process by Wet Chemical Etching." *Langmuir* 23(3): 1564–68.

Haq, Furqan, Venkatramani Anandan, Charles Keith, and Guigen Zhang. 2007. "Neurite Development in PC12 Cells Cultured on Nanopillars and Nanopores with Sizes Comparable with Filopodia." *International journal of nanomedicine* 2(1): 107–15.

Hoffman, Allan S. 2008. "The Origins and Evolution of 'Controlled' Drug Delivery Systems." *Journal of Controlled Release* 132(3): 153–63.

Howarter, John A., and Jeffrey P. Youngblood. 2006. "Optimization of Silica Silanization by 3-Aminopropyltriethoxysilane." *Langmuir* 22(26): 11142–47.

Ilyas, S. et al. 2007. "Porous Silicon Based Narrow Line-Width Rugate Filters." *Optical Materials* 29(6): 619–22.

Ishibashi, Takeshi et al. 2009. "Localized Electrical Stimulation to C2C12 Myotubes Cultured on a Porous Membrane-Based Substrate." *Biomedical Microdevices* 11(2): 413–19.

Italian Patent 741753 (1936). 1936. "No Title."

Jain, Kewal K. 2008. "Drug Delivery Systems - An Overview." *Methods in Molecular Biology* 437: 1–50.

Jang, Ji Hyun et al. 2007. "3D Micro- and Nanostructures via Interference Lithography." *Advanced Functional Materials* 17(16): 3027–41.

Jeon, Gumhye, Seung Yun Yang, Jinseok Byun, and Jin Kon Kim. 2011.

"Electrically Actuatable Smart Nanoporous Membrane for Pulsatile Drug Release." *Nano Letters* 11(3): 1284–88.

Kang, Ho Jae et al. 2007. "Controlled Drug Release Using Nanoporous Anodic Aluminum Oxide on Stent." *Thin Solid Films* 515(12): 5184–87.

Kapruwan, Pankaj, Laura K. Acosta, Josep Ferré-Borrull, and Lluis F. Marsal. 2021. "Optical Platform to Analyze a Model Drug-Loading and Releasing Profile Based on Nanoporous Anodic Alumina Gradient Index Filters." *Nanomaterials* 11(3): 1–16.

Karlsson, M., and L. Tang. 2006. "Surface Morphology and Adsorbed Proteins Affect Phagocyte Responses to Nano-Porous Alumina." In *Journal of Materials Science: Materials in Medicine*, , 1101–11.

Keller, F., M. S. Hunter, and D. L. Robinson. 1953. "Structural Features of Oxide Coatings on Aluminum." *Journal of The Electrochemical Society* 100(9): 411.

Koehler, Ralf, Roland Steitz, and Regine Von Klitzing. 2014. "About Different Types of Water in Swollen Polyelectrolyte Multilayers." *Advances in Colloid and Interface Science* 207(1): 325–31.

Kondo, Toshiaki, Kazuyuki Nishio, and Hideki Masuda. 2009. "Surface-Enhanced Raman Scattering in Multilayered Au Nanoparticles in Anodic Porous Alumina Matrix." *Applied Physics Express* 2(3): 032001.

Krismastuti, Fransiska Sri Herwahyu, Haider Bayat, Nicolas H. Voelcker, and Holger Schönherr. 2015. "Real Time Monitoring of Layer-by-Layer Polyelectrolyte Deposition and Bacterial Enzyme Detection in Nanoporous Anodized Aluminum Oxide." *Analytical Chemistry* 87(7): 3856–63.

Kumeria, Tushar et al. 2015. “Photoswitchable Membranes Based on Peptide-Modified Nanoporous Anodic Alumina: Toward Smart Membranes for on-Demand Molecular Transport.” *Advanced Materials* 27(19): 3019–24.

Kumeria, Tushar, Karan Gulati, Abel Santos, and Dusan Losic. 2013. “Real-Time and in Situ Drug Release Monitoring from Nanoporous Implants under Dynamic Flow Conditions by Reflectometric Interference Spectroscopy.” *ACS Applied Materials and Interfaces* 5(12): 5436–42.

Largueze, Jean Baptiste, Karim El Kirat, and Sandrine Morandat. 2010. “Preparation of an Electrochemical Biosensor Based on Lipid Membranes in Nanoporous Alumina.” *Colloids and Surfaces B: Biointerfaces* 79(1): 33–40.

LaVan, David A, Terry McGuire, and Robert Langer. 2003. “Small-Scale Systems for in Vivo Drug Delivery.” *Nature Biotechnology* 21(10): 1184–91.

Law, Cheryl Suwen et al. 2018. “Nanoporous Anodic Alumina Photonic Crystals for Optical Chemo- and Biosensing: Fundamentals, Advances, and Perspectives.” *Nanomaterials* 8(10): 788.

Law, Cheryl Suwen, Lluís F. Marsal, and Abel Santos. 2019. “Electrochemically Engineered Nanoporous Photonic Crystal Structures for Optical Sensing and Biosensing.” In *Handbook of Nanomaterials in Analytical Chemistry: Modern Trends in Analysis*, Elsevier, 201–26.

Lee, Woo, Ran Ji, Ulrich Gösele, and Kornelius Nielsch. 2006. “Fast Fabrication of Long-Range Ordered Porous Alumina Membranes by Hard Anodization.” *Nature Materials* 5(9): 741–47.

Li, F. 1998. *Nanostructure of Anodic Porous Alumina Films of Interest in Magnetic Recording*. University of Alabama.

Li, Feiyue, Lan Zhang, and Robert M. Metzger. 1998. "On the Growth of Highly Ordered Pores in Anodized Aluminum Oxide." *Chemistry of Materials* 10(9): 2470–80.

Li, Peng Fei et al. 2009. "Thermo-Responsive Gating Membranes with Controllable Length and Density of Poly(N-Isopropylacrylamide) Chains Grafted by ATRP Method." *Journal of Membrane Science* 337(1–2): 310–17.

Li, Zhu Zhu, Li Xiong Wen, Lei Shao, and Jian Feng Chen. 2004. "Fabrication of Porous Hollow Silica Nanoparticles and Their Applications in Drug Release Control." *Journal of Controlled Release* 98(2): 245–54.

Lim, Siew Yee et al. 2018. "Engineering the Slow Photon Effect in Photoactive Nanoporous Anodic Alumina Gradient-Index Filters for Photocatalysis." *ACS Applied Materials and Interfaces* 10(28): 24124–36.

Lorenzo, Eduardo et al. 2005. "Porous Silicon-Based Rugate Filters." *Applied Optics* 44(26): 5415–21.

Losic, Dusan, and Mickael Lillo. 2009. "Porous Alumina with Shaped Pore Geometries and Complex Pore Architectures Fabricated by Cyclic Anodization." *Small* 5(12): 1392–97.

Lyklema, J. 1991. 1 *Fundamentals of Interface and Colloid Science, 1st Edition*.

Macleod, H. Angus. 2010. Thin-Film Optical Filters, Fourth Edition *Thin-Film Optical Filters*. CRC Press.

Masuda, H., and K. Fukuda. 1995. "Ordered Metal Nanohole Arrays Made by a Two-Step Replication of Honeycomb Structures of Anodic Alumina." *Science* 268(5216): 1466–68.

Masuda, Hideki et al. 2006. "Lasing from Two-Dimensional Photonic Crystals Using Anodic Porous Alumina." *Advanced Materials* 18(2): 213–16.

Md Jani, Abdul Mutalib, Dusan Losic, and Nicolas H. Voelcker. 2013. "Nanoporous Anodic Aluminium Oxide: Advances in Surface Engineering and Emerging Applications." *Progress in Materials Science* 58(5): 636–704.

Mir, M. A., M. A. Shah, and P. A. Ganai. 2020. "Nanoporous Anodic Alumina (NAA) Prepared in Different Electrolytes with Different Pore Sizes for Humidity Sensing." *Journal of Solid State Electrochemistry* 24(7): 1679–86.

Montero-Moreno, J. M., M. Belenguer, M. Sarret, and C. M. Müller. 2009. "Production of Alumina Templates Suitable for Electrodeposition of Nanostructures Using Stepped Techniques." *Electrochimica Acta* 54(9): 2529–35.

Morais, Jacqueline M., Fotios Papadimitrakopoulos, and Diane J. Burgess. 2010. "Biomaterials/Tissue Interactions: Possible Solutions to Overcome Foreign Body Response." *The AAPS Journal* 12(2): 188–96.

Mozalev, A., I. Mozaleva, M. Sakairi, and H. Takahashi. 2005. "Anodic Film Growth on Al Layers and Ta-Al Metal Bilayers in Citric Acid Electrolytes." In *Electrochimica Acta*, Pergamon, 5065–75.

Mutalib Md Jani, Abdul et al. 2009. "Nanoporous Anodic Aluminium Oxide Membranes with Layered Surface Chemistry." *Chemical*

Communications (21): 3062–64.

Nagale, M., B. Y. Kim, and M. L. Bruening. 2000. "Ultrathin, Hyperbranched Poly(Acrylic Acid) Membranes on Porous Alumina Supports." *Journal of the American Chemical Society* 122(47): 11670–78.

Nasirpouri, F., M. Abdollahzadeh, M. J. Almasi, and N. Parvini-Ahmadi. 2009. "A Comparison between Self-Ordering of Nanopores in Aluminium Oxide Films Achieved by Two- and Three-Step Anodic Oxidation." *Current Applied Physics* 9(1 SUPPL.): S91–94.

Nasu, Yusuke, and Shinji Yamashita. 2005. "Densification of Sampled Fiber Bragg Gratings Using Multiple-Phase-Shift (MPS) Technique." *Journal of Lightwave Technology* 23(4): 1808–17.

Nguyen, Binh T.T., Eugene Zhi Chao Ting, and Chee Seng Toh. 2008. "Development of a Biomimetic Nanoporous Membrane for the Selective Transport of Charged Proteins." *Bioinspiration and Biomimetics* 3(3): 035008.

Ni, Siyu et al. 2014. "Understanding Improved Osteoblast Behavior on Select Nanoporous Anodic Alumina." *International Journal of Nanomedicine* 9(1): 3325–34.

Nielsch, Kornelius et al. 2002. "Self-Ordering Regimes of Porous Alumina: The 10% Porosity Rule." *Nano Letters*.

Noh, Kunbae. 2011. "A New Nano-Platform for Drug Release via Nanotubular Aluminum Oxide." *Journal of Biomaterials and Nanobiotechnology* 02(July): 226–33.

O'Sullivan JP, and Wood GC. 1970. "Morphology and Mechanism of Formation of Porous Anodic Films on Aluminum." In *Proc Roy Soc Ser*

A Math Phys Sci, The Royal Society London.

Odom, Damian J., Lane A. Baker, and Charles R. Martin. 2005. "Solvent-Extraction and Langmuir-Adsorption-Based Transport in Chemically Functionalized Nanopore Membranes." *Journal of Physical Chemistry B* 109(44): 20887–94.

Ohta, Kotoe Machida, Masayoshi Fuji, Takashi Takei, and Masatoshi Chikazawa. 2005. "Development of a Simple Method for the Preparation of a Silica Gel Based Controlled Delivery System with a High Drug Content." *European Journal of Pharmaceutical Sciences* 26(1): 87–96.

Ono, Sachiko, Makiko Saito, and Hidetaka Asoh. 2005. "Self-Ordering of Anodic Porous Alumina Formed in Organic Acid Electrolytes." In *Electrochimica Acta*, Pergamon, 827–33.

Orosco, Manuel M., Claudia Pacholski, Gordon M. Miskelly, and Michael J. Sailor. 2006. "Protein-Coated Porous-Silicon Photonic Crystals for Amplified Optical Detection of Protease Activity." *Advanced Materials* 18(11): 1393–96. https://onlinelibrary.wiley.com/doi/full/10.1002/adma.200502420 (May 14, 2021).

Otsuka, Makoto, Kana Tokumitsu, and Yoshihisa Matsuda. 2000. "Solid Dosage Form Preparations from Oily Medicines and Their Drug Release. Effect of Degree of Surface-Modification of Silica Gel on the Drug Release from Phytonadione-Loaded Silica Gels." *Journal of Controlled Release* 67(2–3): 369–84.

Palik, Edward D. 2012. 1 Handbook of Optical Constants of Solids *Handbook of Optical Constants of Solids*.

Pardon, Gaspard et al. 2013. “Pt-Al2O3 Dual Layer Atomic Layer Deposition Coating in High Aspect Ratio Nanopores.” *Nanotechnology* 24(1).

Pitzschel, Kristina et al. 2009. “Controlled Introduction of Diameter Modulations in Arrayed Magnetic Iron Oxide Nanotubes.” *ACS Nano* 3(11): 3463–68.

Platt, Mark, Robert A.W. Dryfe, and Edward P.L. Roberts. 2003. “Electrodeposition of Palladium Nanoparticles at the Liquid-Liquid Interface Using Porous Alumina Templates.” In *Electrochimica Acta*, Pergamon, 3037–46.

Poinern, Gérrard Eddy Jai et al. 2014. “Chemical Synthesis, Characterisation, and Biocompatibility of Nanometre Scale Porous Anodic Aluminium Oxide Membranes for Use as a Cell Culture Substrate for the Vero Cell Line: A Preliminary Study.” *BioMed Research International* 2014: 1–10.

Popat, Ketul C, Gopal Mor, Craig A Grimes, and Tejal A Desai. 2004. “Surface Modification of Nanoporous Alumina Surfaces with Poly(Ethylene Glycol).” *Langmuir* 20(19): 8035–41.

Popp, Alexander, Jörg Engstler, and Jörg J. Schneider. 2009. “Porous Carbon Nanotube-Reinforced Metals and Ceramics via a Double Templating Approach.” *Carbon* 47(14): 3208–14.

Porta-i-Batalla, Maria et al. 2016. “Sustained, Controlled and Stimuli-Responsive Drug Release Systems Based on Nanoporous Anodic Alumina with Layer-by-Layer Polyelectrolyte.” *Nanoscale Research Letters* 11(1): 372.

Pottier, Pierre, Sara Mastroiacovo, and Richard M. De La Rue. 2006. “Power and Polarization Beam-Splitters, Mirrors, and Integrated Interferometers

Based on Air-Hole Photonic Crystals and Lateral Large Index-Contrast Waveguides." *Optics Express* 14(12): 5617.

Qiang, Zexuan, Weidong Zhou, and Richard A. Soref. 2007. "Optical Add-Drop Filters Based on Photonic Crystal Ring Resonators." *Optics Express* 15(4): 1823.

Qiu, Teng et al. 2009. "Controlled Assembly of Highly Raman-Enhancing Silver Nanocap Arrays Templated by Porous Anodic Alumina Membranes." *Small* 5(20): 2333–37.

Rahman, Shafiur, Gerald J Atkins, David M Findlay, and Dusan Losic. 2015. "Nanoengineered Drug Releasing Aluminium Wire Implants: A Model Study for Localized Bone Therapy." *Journal of Materials Chemistry B* 3(16): 3288–96.

Rana, Kuldeep, Gokce Kucukayan-Dogu, and Erman Bengu. 2012. "Growth of Vertically Aligned Carbon Nanotubes over Self-Ordered Nano-Porous Alumina Films and Their Surface Properties." *Applied Surface Science* 258(18): 7112–17.

Ranade, Vasant V., John B. Cannon, and John B. Cannon. 2011. *Drug Delivery Systems*. CRC Press.

Ruminski, Anne M. et al. 2010. "Porous Silicon-Based Optical Microsensors for Volatile Organic Analytes: Effect of Surface Chemistry on Stability and Specificity." *Advanced Functional Materials* 20(17): 2874–83.

Santos, A., J. Ferré-Borrull, J. Pallarès, and L. F. Marsal. 2011. "Hierarchical Nanoporous Anodic Alumina Templates by Asymmetric Two-Step Anodization." *Physica Status Solidi (A) Applications and Materials Science* 208(3): 668–74.

Santos, Abel et al. 2011. "Structural Engineering of Nanoporous Anodic Alumina Funnels with High Aspect Ratio." *Journal of Electroanalytical Chemistry* 655(1): 73–78.

Santos, Abel et al 2014. "Drug-Releasing Implants: Current Progress, Challenges and Perspectives." *Journal of Materials Chemistry B* 2(37): 6157–82.

Santos, Abel, Tushar Kumeria, and Dusan Losic. 2014. "Nanoporous Anodic Alumina: A Versatile Platform for Optical Biosensors." *Materials* 7(6): 4297–4320.

Schmaljohann, Dirk. 2006. "Thermo- and PH-Responsive Polymers in Drug Delivery." *Advanced Drug Delivery Reviews* 58(15): 1655–70.

Senapati, Sudipta, Arun Kumar Mahanta, Sunil Kumar, and Pralay Maiti. 2018. "Controlled Drug Delivery Vehicles for Cancer Treatment and Their Performance." *Signal Transduction and Targeted Therapy* 3(1): 1–19.

Sher, Praveen, Ganesh Ingavle, Surendra Ponrathnam, and Atmaram P. Pawar. 2007. "Low Density Porous Carrier. Drug Adsorption and Release Study by Response Surface Methodology Using Different Solvents." *International Journal of Pharmaceutics* 331(1): 72–83.

Shimizu, K., K. Kobayashi, G. E. Thompson, and G. C. Wood. 1991. "Novel Marker for the Determination of Transport Numbers during Anodic Barrier Oxide Growth on Aluminium." *Philosophical Magazine B: Physics of Condensed Matter; Electronic, Optical and Magnetic Properties* 64(3): 345–53.

Silva, Rubiana M. Mainardesand Luciano P. 2004. "Drug Delivery Systems:

Past, Present and Future." *Current Drug Targets* 5: 449–55.

Simovic, Spomenka, Dusan Losic, and Krasimir Vasilev. 2010. "Controlled Drug Release from Porous Materials by Plasma Polymer Deposition." *Chemical Communications* 46(8): 1317.

Smuleac, V. et al. 2005. "Polythiol-Functionalized Alumina Membranes for Mercury Capture." *Journal of Membrane Science* 251(1–2): 169–78.

Squire, E. K. et al. 2000. "Light Emission from Highly Reflective Porous Silicon Multilayer Structures." *Journal of Porous Materials* 7(1): 209–13.

Takahashi, H., and M. Nagayama. 1978. "The Determination of the Porosity of Anodic Oxide Films on Aluminium by the Pore-Filling Method." *Corrosion Science* 18(10): 911–25.

Thakur, S. et al. 2012. "Depth Matters: Cells Grown on Nano-Porous Anodic Alumina Respond to Pore Depth." *Nanotechnology* 23(25).

Thompson, G.E., and G.C. Wood. 1983. "Anodic Films on Aluminium." In Elsevier, 205–329.

Treccani, Laura et al. 2013. "Functionalized Ceramics for Biomedical, Biotechnological and Environmental Applications." *Acta Biomaterialia* 9(7): 7115–50.

Trindade, Ricardo, Tomas Albrektsson, Pentti Tengvall, and Ann Wennerberg. 2016. "Foreign Body Reaction to Biomaterials: On Mechanisms for Buildup and Breakdown of Osseointegration." *Clinical Implant Dentistry and Related Research* 18(1): 192–203.

Velha, P. et al. 2007. "Ultra-High Q/V Fabry-Perot Microcavity on SOI Substrate." *Optics Express* 15(24): 16090.

Velleman, Leonora et al. 2009. "Structural and Chemical Modification of Porous Alumina Membranes." *Microporous and Mesoporous Materials* 126(1–2): 87–94.

Walpole, A. R. et al. 2003. "Nano-Porous Alumina Coatings for Improved Bone Implant Interfaces." In *Materialwissenschaft Und Werkstofftechnik*, John Wiley & Sons, Ltd, 1064–68.

Wang, Chaoyang et al. 2006. "Combination of Adsorption by Porous CaCO3 Microparticles and Encapsulation by Polyelectrolyte Multilayer Films for Sustained Drug Delivery." *International Journal of Pharmaceutics* 308(1–2): 160–67.

Wang, Hai Juan et al. 2006. "Template Synthesized Molecularly Imprinted Polymer Nanotube Membranes for Chemical Separations." *Journal of the American Chemical Society* 128(50): 15954–55.

Wang, Ye et al. 2014. "Structurally Engineered Anodic Alumina Nanotubes as Nano-Carriers for Delivery of Anticancer Therapeutics." *Biomaterials* 35(21): 5517–26.

Wang, Ye et al. 2015. "Systematic Invitro Nanotoxicity Study on Anodic Alumina Nanotubes with Engineered Aspect Ratio: Understanding Nanotoxicity by a Nanomaterial Model." *Biomaterials* 46: 117–30.

Whitney, T. M., J. S. Jiang, P. C. Searson, and C. L. Chien. 1993. "Fabrication and Magnetic Properties of Arrays of Metallic Nanowires." *Science* 261(5126): 1316–19.

Wieneke, Heinrich et al. 2003. "Synergistic Effects of a Novel Nanoporous Stent Coating and Tacrolimus on Intima Proliferation in Rabbits." *Catheterization and Cardiovascular Interventions* 60(3): 399–407.

Wolfrum, Bernhard, Yulia Mourzina, Frank Sommerhage, and Andreas Offenhäusser. 2006. "Suspended Nanoporous Membranes as Interfaces for Neuronal Biohybrid Systems." *Nano Letters* 6(3): 453–57.

Wolinsky, Jesse B., Yolonda L. Colson, and Mark W. Grinstaff. 2012. "Local Drug Delivery Strategies for Cancer Treatment: Gels, Nanoparticles, Polymeric Films, Rods, and Wafers." *Journal of Controlled Release* 159(1): 14–26.

Wood, G. C., P. Skeldon, G. E. Thompson, and K. Shimizu. 1996. "A Model for the Incorporation of Electrolyte Species into Anodic Alumina." *Journal of The Electrochemical Society* 143(1): 74–83.

Xifre-Perez, Elisabet et al. 2015. "In Vitro Biocompatibility of Surface-Modified Porous Alumina Particles for HepG2 Tumor Cells: Toward Early Diagnosis and Targeted Treatment." *ACS Applied Materials and Interfaces* 7(33): 18600–608.

Yamaura, M. et al. 2004. "Preparation and Characterization of (3-Aminopropyl)Triethoxysilane-Coated Magnetite Nanoparticles." *Journal of Magnetism and Magnetic Materials* 279(2–3): 210–17.

Yeh, Pochi. 2005. "Optical Waves in Layered Media (Wiley Series in Pure and Applied Optics)." : 416.

Yun, Yeon Hee, Byung Kook Lee, and Kinam Park. 2015. "Controlled Drug Delivery: Historical Perspective for the next Generation." *Journal of controlled release : official journal of the Controlled Release Society* 219: 2–7.

Zajaczkowska, Lidia, Dariusz Siemiaszko, and Małgorzata Norek. 2020. "Towards Self-Organized Anodization of Aluminum in Malic Acid

Solutions-New Aspects of Anodization in the Organic Acid." *Materials* 13(17): 3899.

Zaraska, Leszek, Grzegorz D. Sulka, Janusz Szeremeta, and Marian Jaskuła. 2010. "Porous Anodic Alumina Formed by Anodization of Aluminum Alloy (AA1050) and High Purity Aluminum." *Electrochimica Acta* 55(14): 4377–86.

Zhang, Chun, Feng Qiao, Jun Wan, and Jian Zi. 2000. "Enlargement of Nontransmission Frequency Range in Photonic Crystals by Using Multiple Heterostructures." *Journal of Applied Physics* 87(6): 3174–76.

Zhao, Qiang et al. 2011. "Synthesis of Dense, Single-Crystalline CrO 2 Nanowire Arrays Using AAO Template-Assisted Chemical Vapor Deposition." *Nanotechnology* 22(12).

Zhao, Xiao Ping et al. 2018. "Thermo and PH Dual – Actuating Smart Porous Anodic Aluminum for Controllable Drug Release." *Advanced Materials Interfaces* 5(13).

Zi, Jian, Jun Wan, and Chun Zhang. 1998. "Large Frequency Range of Negligible Transmission in One-Dimensional Photonic Quantum Well Structures." *Applied Physics Letters* 73(15): 2084–86.

Departament d'Enginyeria Electrònica, Elèctrica i Automàtica

UNIVERSITAT
ROVIRA i VIRGILI